The structural and magnetization studies of Transition Metal-doped ZnO thin films

Yong Zhihua

Supervisors:
Prof. Andrew Wee
& Dr. Liu Tao

In partial fulfillment of the requirement for the Master of Science (Physics)

DEPARTMENT OF PHYSICS

NATIONAL UNIVERSITY OF SINGAPORE

2008

CONTENT

Acknowledgement

I am truly grateful to the people who have made the accomplishment of this project possible. I would like to express my deepest appreciation to the following people without whom my project would not have been completed.

First, I would like to thank my supervisor, Prof. Andrew Wee, for his guidance and support in the course of this work and also giving me the opportunity to continue my studies. I have greatly improved my organization and interpersonal skills throughout these years. I would also like to thank Dr Liu Tao for his guidance in the experiments.

I am also grateful to my family members and all friends who have given me emotional support throughout these years. Last but not least, I would also like to thank the Laboratory technicians, Mr Chen and Mr Ho.

Yong Zhihua

June 2008

Abstract

A dilute magnetic semiconductor (DMS) is a material in which a fraction of the host cations are substitutionally replaced by magnetic ions or appropriate rare earths. This leads to localized magnetic moments in the semiconductor matrix. DMS is regarded as the key materials for spin electronics where not only charge but also spin of electrons are used for electronic functionality. Ferromagnetic semiconductors with Curie temperatures (T_C) above room temperature are ideal for more efficient spintronics devices, and high T_C ferromagnetic properties in DMS have been reported. However, the origin of room temperature ferromagnetism in DMS is still controversial. Four common possible origins of ferromagnetism in DMS have been proposed and this thesis aims to examine their feasibility. Zinc oxide (ZnO) is well known for its direct band-gap and large excitation energy, and exhibits unique piezoelectric and electric-optic properties. In particular, ZnO has been identified as a good host material for realizing wide band-gap DMS with high T_C ferromagnetism by doping with magnetic ions.

In this project, $Zn_{1-x}TM_xO$ (TM – Co, Cu, Ti and Mn) films were fabricated on Si (100) substrates by radio-frequency magnetron sputtering. Profilometry measurements, scanning electron microscopy (SEM), X-ray fluorescence (XRF), X-ray diffraction (XRD), X-ray absorption fine structure studies (XAFS) and vibrating sample magnetometer (VSM) measurements were used to characterize the samples and investigate the origins of magnetism.

Chapter 1

Dilute Magnetic Semiconductors

1.1 Spintronics

Spintronic devices are devices exploiting spins as information carriers. They exhibit performances superior to conventional electronic devices. Semiconductors lasers fed by spin-polarized currents will have better mode stability and lower critical currents. Similarly, spin transistors (Fig. 3.1) consisting of a conductor sandwiched between ferromagnetic contacts is expected to be faster and more efficient than a standard field-effect transistor.[1]

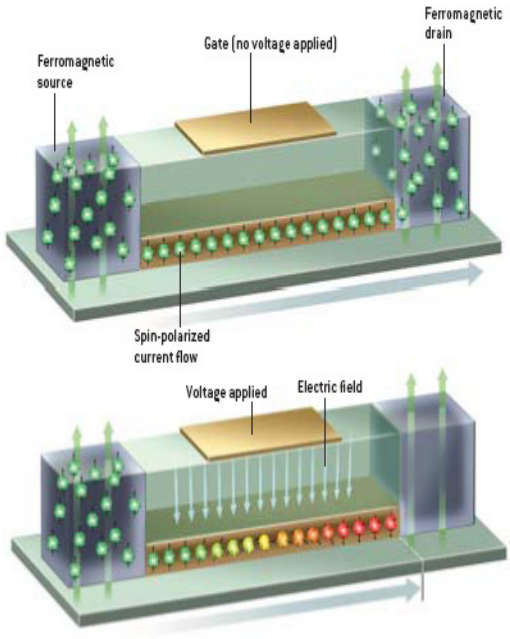

Fig. 3.1. Spin field-effect transistor (Spin FET).[2]

Semiconductor-based electronic devices, used for information processing and communications, have had great success using only the

charge of electrons. On the other hand, the spin of electrons in ferromagnetic materials plays the major role in information storage technology, for example in hard disks, magnetic tapes, and magneto-optical disks.[3] There is now great interest to further enhance the performance of electronic devices by using both charge and spin of electrons simultaneously, so that the device would have the capability of mass storage and information processing at the same time. The combination of charge and spin of electrons is known as spintronics (spin-polarized electronics) or magneto-electronics.[2]

1.2 Introduction to Dilute Magnetic Semiconductors

Dilute magnetic semiconductor (DMS) is a material in which a fraction of the host cations is substitutionally replaced by magnetic ions or appropriate rare earths.[4] This leads to localized magnetic moments in the semiconductor matrix. Usually, magnetic moments originate from the partially filled 3d or 4f shells of transition metals (TM) or rare earths elements. The partially filled d states or f states contain unpaired electrons, in terms of their spin, which are responsible for their magnetic behaviour.[4] In DMS materials, the delocalized conduction band electrons and valence band holes interact with the localized magnetic moments associated with the magnetic atoms.[4] Generally, when 3d transition-metal ions substitute the host cations, the resultant electronic structure is influenced by strong hybridization of the 3d orbitals of the magnetic ion and mainly the p orbitals of the neighbouring host anions.[4] This hybridization gives rise to strong magnetic interaction between the localized 3d spins and the carriers in the host valence band.[4]

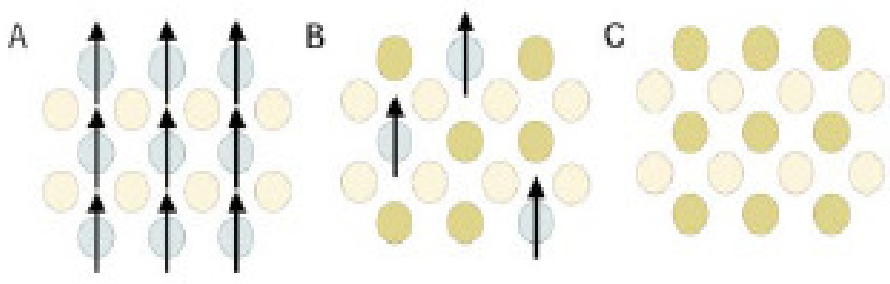

Fig. 1.2. Classification of semiconductor based on its magnetic behavior: a) magnetic semiconductor, b) dilute magnetic semiconductor, and c) nonmagnetic semiconductor.[5]

The concept of DMS was first introduced by Dietl et al.[1] who predicted the mean-field Zener model of ferromagnetism in ZnO and GaN above room temperature upon doping with transition elements such as Mn (on the order of 5% or more) in p-type materials in 2000. Sato et al.[6] predicted that the ferromagnetic state Co^{2+} in Co-doped ZnO could be stabilized by s-d hybridization, pointing to the possibility that high-temperature ferromagnetic materials could be realized in n-type ZnO. By doping magnetically active atoms into semiconductors, dilute magnetic semiconductors (Fig. 1.2b) are formed having both semiconducting and ferromagnetic properties, and whereby spins can be controlled using B-fields and E-fields. The idea of a dilute magnetic semiconductor is appealing because such a system has both semiconducting and ferromagnetic properties. Semiconductors such as those from group II-VI (e.g., ZnO, TiO_2, and SnO_2) and group III-V (e.g., GaAs, InSb) can be doped with transition metals (Cr, Mn, Fe, Co, and Ni). Physically, the magnetic ions will substitute a fraction of the cations in the host semiconductor. A major difficulty is the preparation and synthesis of perfectly doped DMSs due to the insolubility or instability of impurities in the host materials from the thermodynamic point of view.

There are five essential requirements for implementing a semiconductor in spintronics technology [2]:

1) Efficient electrical injection of spin-polarized carriers into semiconductors

2) Adequate spin diffusion lengths and lifetimes for transport in the device
3) Effective control and manipulation of the spin system
4) Efficient detection of the spin system to determine the output
5) Curie temperature (T_c) above room temperature

DMS are promising materials since they have charge and spin degrees of freedom in a single matrix leading to an interplay of magnetic, optical, and electronic functionalities. Many studies on DMS have been done, such as transition metal (Cr, Mn, Fe, Co, and Ni)-doped II-VI and III-V compound semiconductors. The transition metal-doped II-VI compound semiconductors include a variety of compounds consisting of various combinations of group II cations (Zn, Cd, and Hg) and group VI anions (O, S, Se, and Te) while the transition metal-doped III-V compound semiconductors include a variety of compounds consisting of various combinations of group III cations (B, Al, Ga, and In) and group V anions (N, P, As, and Sb).[2]

There is also much interest in oxide-based DMS because oxide semiconductors (e.g: ZnO, TiO_2, and SnO_2) have the following advantages over non-oxide semiconductors[2]:

1. wide bandgap suited for applications with short light wavelengths
2. transparency and dyeability with pigments
3. high n-type carrier concentration
4. easily grown at low temperatures

Much research on dilute magnetic semiconductors is currently on-going. The aims are to study the mechanism of ferromagnetism and also to improve the efficiency of spin injection into the semiconductors.[2] Due to the necessity that DMS materials must exhibit ferromagnetism with a critical temperature above room temperature in order to have practical applications in spintronic devices, T_c is naturally deemed to be the bottleneck issue.[4]

1.2.1 ZnO

Zinc oxide (ZnO) is well known for its direct band-gap and large excitation energy, and exhibits unique piezoelectric and electric-optic properties. The band-gap is the approximately the absorption edge which corresponds to a particular wavelength at which the material absorbs light. In the series of 3d metal oxides from Sc to Zn, the band gap tends to reduce progressively. ZnO has a band gap of ~3.4eV, placing it in the vicinity of insulating materials. For ZnO**,** this happens around a wavelength of 380nm which is in the UV region of the light spectrum. The band-gap is tuneable from 2.8 to 3.3eV and from 3.3 to 4eV, depending on the alloying material.

Instead of the NaCl-type crystal structure found in most mono-oxides of 3d metals, ZnO takes the wurtzite structure in which Zn and O are tetrahedrally coordinated, slightly distorted in the [111] direction. It is generally accepted that 4s and 4p orbitals of Zn contribute to the chemical bonding of valence electrons, the bond is ionic but with covalent character.[7] The partial replacement of Zn by other TM elements can introduce additional electronic bands from 3d orbitals, significantly changing the degree of covalency and overall electronic configurations. Therefore, it is essential to investigate the local atomic and electronic configuration and arrangement of these dopants in ZnO.

In addition, ZnO has large exciton energy (~60meV) which is useful for efficient UV laser applications. In particular, ZnO has been identified as a good host material for realizing wide band-gap DMS with high T_C ferromagnetism by doping with magnetic ions.[8] The magnetic properties due to the doping of Ti, Mn, Co and Cu in ZnO prepared by a variety of methods have been reported.[9-14]

1.3 Origin of magnetism in DMS

The first study on oxide-semiconductors (Mn-doped ZnO) was done by Fukumura et al.[15] but it showed no ferromagnetic behavior. Another work by Ueda et al.[16] using Pulsed Laser Deposition (PLD) technique to make

transition metal-doped ZnO films on α-Al2O3 (1120) substrates also reported no ferromagnetic behavior in (Mn, Cr, and Ni)-doped ZnO. However, their Co-doped ZnO ($Zn_{1-x}Co_xO$) films showed ferromagnetic behavior at room temperature. Many conflicting experimental results have been reported for TM doped ZnO.[4]

Theoretical results focusing on the magnetic properties and high T_C behavior of DMSs have been reported[4,17] but there is no consensus about the origin of the magnetic properties. The Zener model[1,8] based on mean field theory takes into account the anisotropy of the carrier-mediated exchange interaction associated with spin-orbit coupling in the host material. To achieve a high T_C, a specific amount of magnetic ions and a sufficiently high concentration of holes are required which is not easily achievable from the experimental point of view. Using density functional theory calculations for TM doped ZnO, Sato et al.[6,18] concluded that ferromagnetic states can be stabilized for V, Cr, Fe, Co and Ni-doped ZnO at concentrations ranging from 5 to 25%. A modified model proposed by Coey et al.[19] ascribed the origin of ferromagnetism to the formation of bound magnetic polarons (BMP) which overlap to create a spin-split impurity band.

Four common possible origins of ferromagnetism in DMS have been proposed. The first is the bound magnetic polaron (BMP) model.[19] The second is the spin-split impurity-band model.[20] The third is carrier-induced ferromagnetism.[4] The fourth is the ferromagnetism of TM or TM oxide clusters found in DMS samples but this will not be discussed in detail.

1.3.1 Bound magnetic polaron model

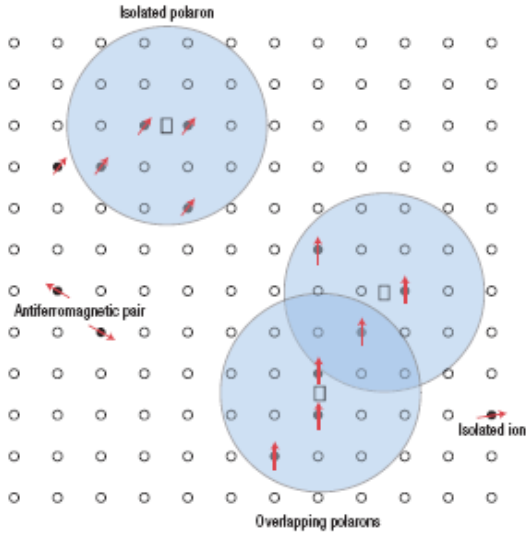

Fig. 1.3. Representation of magnetic polarons. A donor electron couples its spin antiparallel to impurities with a half-full or more than half-full 3d shell. The figure is drawn for magnetic cation concentration x=0.1 and when the orbital radius of the magnetic cation is sufficiently large. Cation sites are represented by small circles. Oxygen is not shown; the unoccupied oxygen sites are represented by squares.[4,19]

A possible explanation for intrinsic magnetism can be found invoking a supercoupling mechanism based on the BMP model. An electron associated with a particular defect is confined in a hydrogenic orbital of radius $r_H = \varepsilon_r(m/m^*)a_0 = \gamma a_0$ and $\gamma = \varepsilon_r (m/m^*)$, where ε_r is the dielectric constant, m is the electron mass, m^* is the effective mass of the donor electrons and a_0 is the Bohr radius (0.53 Å).[21] Taking into account a sufficiently large orbital radius, say for γ =7, overlap between a hydrogenic electron and the cations within its orbit leads to

FM supercoupling between them[21], as shown in Fig. 1.3. The interaction between the hydrogenic electron and the cations is represented by a Heisenberg exchange Hamiltonian[22]:

$$\hat{H}_{ij} = \sum_{ij} J_{ij}\hat{S}_i\hat{s}_j \qquad \text{---(1)}$$

where S is the spin of the TM ion and s is the donor electron spin. The donors tend to form a BMP, coupling TM ion within their orbits.[21] The Hamiltonian of a two-polaron subsystem is given by Eq. (1), where the donor electron spin index j takes only two values j_1 and j_2 corresponding to the two polarons under consideration.[21]

The bound magnetic polarons[20,23,24,25,26] are formed by the alignment of the spins of many TM ions with that of much lower number of weakly bound carriers such as excitons within a polaron radius.[4] The basic idea is illustrated in Fig. 1.3. The localized holes of the polarons act on the TM impurities surrounding them, producing an effective magnetic field and aligning all spins.[4] As the temperature decreases, the interaction distance (boundary) grows.[4] Neighbouring magnetic polarons overlap and interact via magnetic impurities forming correlated clusters of polarons.[4] FM is observed when the size of such clusters is equal to the size of the sample.[4] The model is inherently attractive for low carrier density systems such as many of the electronic oxides.[4] The polaron model is applicable to both p- and n-type host materials. Although the direct exchange interaction of localized holes is antiferromagnetic, the interaction between bound magnetic polarons may be FM for sufficiently large concentrations of magnetic impurities.[4] This enables FM ordering of the TM ions in an otherwise insulating or semi-insulating material.

1.3.2 Spin-split impurity-band model

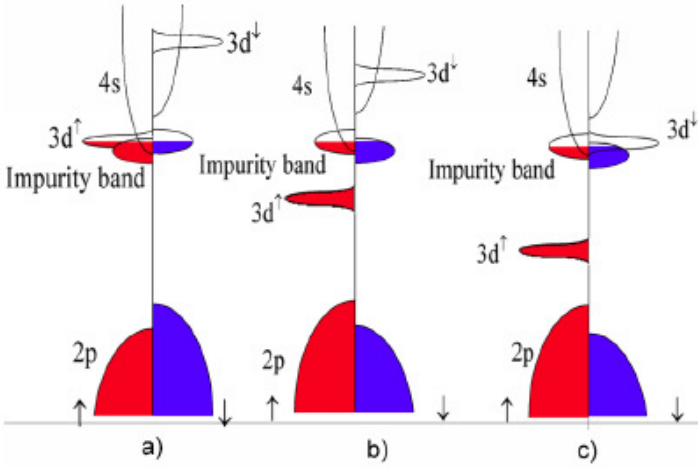

Fig. 1.4. Schematic density of states for (a) TM= Ti, (b) TM = Mn, and (c) TM = Co. The Fermi level lies in a spin-split donor impurity band.

M. Venkatesan et al[19] reported that the variation of magnetic moments across the TM series in TM-doped ZnO can be explained in terms of the spin-split impurity-band model[20] which can account for FM in high-*k* dielectrics doped with a few percent of transition-metal ions. For the light 3*d* elements, the $3d^{\uparrow}$ states lie high in the 2*p*(O) -- 4*s*(Zn) gap, overlapping the donor impurity band which is spin split[19] as shown in Fig. 1.4. In the middle of the series, there is no overlap with the 3*d* levels and exchange is weak, but towards the end of the series the $3d^{\downarrow}$ states overlap the impurity band, which then has the opposite spin splitting for the same occupancy.[19] High Curie temperatures are found whenever unoccupied 3*d* states overlap the impurity band, but not otherwise.[19] The likely origin of the donor impurity band in ZnO films is lattice defects such as oxygen vacancies which can trap between one or two electrons (F^0 centers).[27,28,29]

1.3.3 Carrier-induced ferromagnetism

For carrier-induced ferromagnetism (FM), the samples must first be conducting. There are several carrier-induced ferromagnetism based models

like Ruderman-Kittel-Kasuya-Yoshida (RKKY) type interactions and double exchange interactions. The basic idea behind RKKY interaction is based on indirect exchange coupling between the magnetic ions and the conduction band electrons due to Coulomb exchange. The conduction electron is magnetized in the vicinity of the magnetic ion, with the polarization decaying with distance from the magnetic ion in oscillatory fashion.[4] This oscillation causes an indirect superexchange interaction (RKKY) between two magnetic ions on the nearest or next nearest magnetic neighbours.[4] The coupling may result in a parallel (FM) or an anti-parallel (anti-FM) setting of moments dependent on the separation between interacting atoms.[4]

As the donor concentration δ increases, there comes a point where the impurity-band model breaks down and the donor states merge with the bottom of the conduction band.[20] The RKKY interaction is operative even when the Fermi level lies below the mobility edge, provided the separation of magnetic cation neighbours is less than the localization length.[20] The Fermi wavevector k_F is small at the bottom of the band and the RKKY interaction is always ferromagnetic at low electron densities.[20] At higher densities, the interaction will provide as many negative as positive exchange bonds, and the system becomes a spin glass.[20] The first change of sign of the RKKY function $F(\xi) = -[(\xi\cos(-\sin\xi)/\xi 4]$ is at $\xi = 2k\mathrm{F}r = 2.87$, where k_F is the Fermi wavevector $(3\pi 2n_{\square})1/3$.[20] In a free-electron band the corresponding condition for ferromagnetism $x > 2.6n\delta$, is easily satisfied.[20] The Curie temperature in the molecular field approximation considering only z nearest-neighbour sites is $T_C = 2zJ_{RKKY}\mathbf{S}(\mathbf{S} + 1)/3k_B$ where J_{RKKY} is given by the expression[30] $[(J_{sd}^2 m^* k_F^4 n^2)/(32\pi^3\hbar^2 n_O^2)]\mathrm{F}(\xi)$. In order to enhance the interaction, it would be necessary to transfer conduction-band electrons to the 3*d* impurities but this is precluded for the second half of the 3*d* series if the spin polarization of the conduction band is positive.[20]

In the double exchange mechanism originally proposed by Zener,[31] magnetic ions in different charge states couple with each other by virtual hopping of the extra electron from one ion to the other.[4] In the DMS material, if neighbouring TM magnetic moments are in the same direction,

the TM-d band is widened by the hybrization between the up-spin states.[4] Therefore, in the FM configuration, the band energy can be lowered by introducing carriers to the d band.[4] In these cases, the 3d electron in the partially occupied 3d-orbtials of the TM is allowed to hop to the 3d-orbitals of the neighbouring TM if neighbouring TM ions have parallel magnetic moments.[4] As a result, the d-electron lowers its kinetic energy by hopping in the FM state. This is so called the double exchange mechanism.[4]

1.4 Scope of thesis

It is at presently unclear whether all reports of ferromagnetism particularly at or above room temperatures are indeed intrinsic magnetic behaviour or arising from clustering and segregation effects. However, the observed ferromagnetism of $Ga_{1-x}Mn_xAs$ is well-established and is universally believed to be an intrinsic DMS phenomenon. It is not an overstatement that the expected advantages of GaN and ZnO-based spintronics are truly exciting although the efforts in material science and devices are still in their embryonic stage. Moreover, there are many challenges to consider including whether high ferromagnetic transition temperature and carrier mediated ferromagnetism can be realized.

The scope of the remaining thesis is as follow: The second chapter will describe the set-up of the XDD beamline in Singapore Synchrotron Light Source (SSLS) and the theories of X-ray Absorption Fine Structure (XAFS). The third chapter will discuss the principles of Radio-Frequency (RF) magnetron sputtering and the procedure of the fabrication of the TM-doped thin films. The fourth, fifth and sixth chapters cover the structural characterization, XAFS studies and the magnetization studies of the samples. Finally, the seventh chapter is the conclusion chapter.

References

1. T. Dietl, Nature materials, **2**, 646 (2003).
2. Johnson Kasim, Ong Chong Kim, Yan Lei, Room Temperature oxide-

based Dilute Magnetic Semiconductor on Silicon, National University of Singapore, Department of Physics, Honours year project 2004 April.
3. D. P. DiVincenzo, Science, 270, 255 (1995).
4. C. Liu, F. Yun and H. Morkoc, J. Mater. Sci. in electronics, **16**, 555 (2005).
5. H. Ohno, Science **281**, 951 (1998)
6. K. Sato and H. Katayama-Yoshida, Jpn. J. Appl. Phys., Part 2, **40**, L334 (2001).
7. S. –H. Wei and Alex Zunger, Phy. Rev. B **37**, 8958 (1988).
8. T. Dietl, H. Ohno, F. Matsukura, J. Cibert and D. Ferrand, Science **287**, 1019 (2000).
9. G. A. Prinz, Science, **282**, 1660 (1998).
10. F. Matsukura, H. Ohno, A. Shen and Y. Sugawara, Phys. Rev. B, **57**, R2037 (1998).
11. H. Ohno, A. Shen, F. Matsukura, A. Oiwa, A. Endo, S. Katsumoto, and Y. Iye, Appl. Phys. Lett., **69**, 363 (1996).
12. H. Munekata, H. Ohno, S. von Molnar, A. Segmuller, L. L. chang and L. Esaki, Phys. Rev. Lett., **63**, 1849 (1989).
13. H. Akai, Phys. Rev. Lett., **81**, 3002 (1998).
14. H. Ohno, H. Munekata, T. Penneys S. von Molnar and L. L. Chang, Phys. Rev. Lett., **68**, 2664 (2005).
15. T. Fukumura, Z. Jin, M. Kawasaki, Appl. Phy. Lett., **75**, 3366 (1999).
16. K. Ueda, H. Tabata, and T. Kawai, Appl. Phy. Lett., **79**, 988 (2001).
17. S. Sanvito, G. Theurich and N. A. Hill, J. Supercond. Incorporating Novel magnesium, **51**, 85 (2002).
18. K. Sato and H. Katayama-Yoshida, Semicond. Sc. Technol. **17**, 367 (2002).
19. M. Venkatesan, C. B. Fitzgerald, J.G. Lunney, and J.M. D. Coey, Phys. Rev. Lett., **93**, 177206 (2004).
20. J. M. D. Coey, M. Venkatesan and C. B. Fitzgerald, Nat. Mater., 4, 173 (2005).
21. C. Song, K.W. Geng, F. Zeng, X.B. Wang, Y.X. Shen, F. Pan, Y.N. Xie, T. Liu, H.T. Zhou and Z. Fan, Phys. Rev. B, **73**, 024405 (2006).
22. P. A. Cox, Transition Metal Oxides (Clarendon, Oxford, 1992).
23. M. Berciu and R.N. Bhatt, Phys. Rev. Lett., **87**, 107203 (2001).
24. T. Dietl, F. Matsukura and H. Ohno, Phys. Rev. B, **66**, 033203 (2002).
25. T. Dietl and J. Spalek, Phys. Rev. Lett, **48**, 355 (1982).
26. M. Sawicki, T. Dietl, J. Kossut, J. Igalson, T. Wojtowicz and W. Plesiewicz, Phys. Rev. Lett, **56**, 508 (1986).
27. A. P. Roth, J. B. Webb and D. F. Williams, Phys. Rev. B, **25**, 7836 (1982).
28. A. F. Kohan, G. Ceder, D. Morgan and C.G.Van deWalle, Phys. Rev. B, **61**, 15 019 (2000)
29. S. B. Zhang, S. H. Wei and A. Zunger, Phys. Rev. B, **63**, 075205 (2001).
30. Mattis, D. C. Theory of Magnetism Vol. 1 (Springer, Berlin, 1981).
31. Idem., ibid., **82**, 403 (1951).

Chapter 2

X-ray Absorption Fine Structure

2.1 Introduction

In this thesis, a range of analytical techniques are used to study 3d metal doped ZnO thin films, namely profilometry, SEM, XRD, XRF, SIMS, XAFS and VSM etc. Details of these techniques can be easily found in the references [1]–[8]. In this chapter, we will describe the XAFS technique, which is the main technique used in this thesis.

X-ray absorption fine structure (XAFS) measurements reveal the absorption characteristics of x-rays absorbed by an atom at energies near and above the core-level binding energies of that atom. Specifically, XAFS is the modulation of an atom's x-ray absorption probability due to the chemical and physical state of the atom. XAFS spectra give information on the immediate environment around each absorbing species, and are especially sensitive to the formal oxidation state, coordination chemistry, and the distances, coordination number and species of the atoms immediately surrounding the selected element. Hence, XAFS provides a practical, and relatively simple, way to determine the chemical state and local atomic structure for a selected atomic species. XAFS can be used in a variety of systems, for example in the solid (crystalline or amorphous), liquid or gaseous state.[9]

The x-ray absorption spectrum is typically divided into two regimes: x-ray absorption near-edge spectroscopy (XANES) and extended x-ray absorption fine-structure spectroscopy (EXAFS). XANES is strongly sensitive to the formal oxidation state and coordination chemistry (e.g., octahedral, tetrahedral coordination) of the absorbing atom, while EXAFS is used to determine the distances, coordination number, and species of the neighboring atoms surrounding the absorbing atom.[9] XAFS has the

advantage that it can provide element-specific structural information on crystalline or non-crystalline systems with a bond-length accuracy of 0.01 Å. Therefore, XAFS can be employed as a useful tool to study the DMS system, particularly to probe the dilute doping and impurities in the host.[10]

The development of the XANES and EXAFS techniques came only after the 1970s when intense X-ray sources became readily available through synchrotron laboratories. Synchrotron Light (SL)[1,2,11,12] is produced by electrons circulating in a storage ring at almost the speed of light. The electrons are deviated by the magnetic field of the bending magnets distributed all along the circumference and when the trajectory of the electrons bends, they emit SL composed of bright infra-red, ultraviolet and X-ray light through the *bremsstrahlung* (braking radiation) process. These intense sources of X-ray light make it possible for XANES and EXAFS methods to be employed to investigate structures of materials.

2.2 Principles of XAFS

When x-rays are incident on the sample, the x-rays are absorbed by the electrons in the atom. The atom absorbs an x-ray of energy E, ejecting a core electron of energy E_0 and emitting a photoelectron of energy ($E-E_0$). When the x-ray energy is large enough to promote the core electron to the continuum, there is a sharp increase in the absorption. The absorption spectrum for an isolated atom is depicted on the left of Fig. 2.1. However, in the presence of neighboring atoms in the vicinity, the emitted photoelectron interacts with the surrounding atoms.[13]

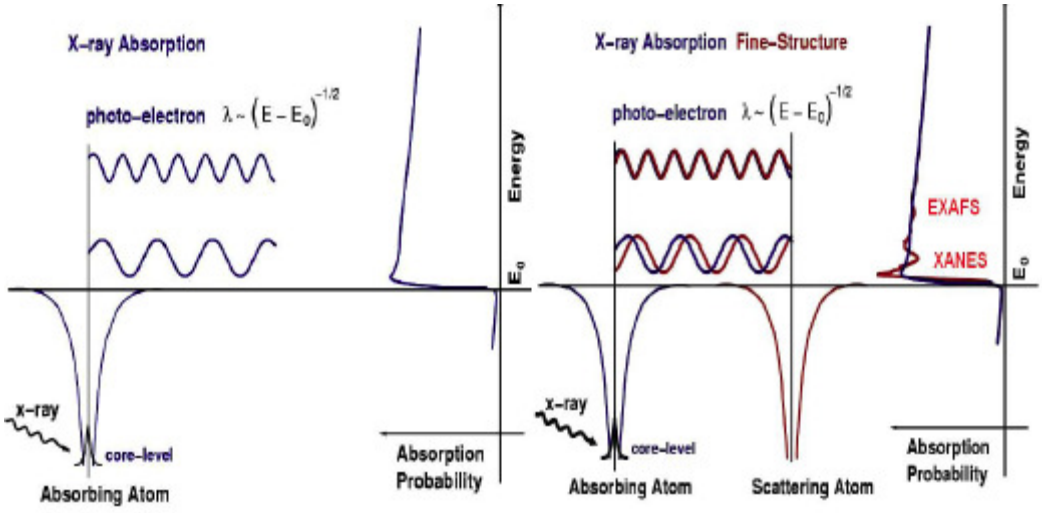

Fig. 2.1. X-ray Absorption due to isolated atom and with scattering atom.[9]

When the wave nature of the ejected photoelectrons are taken into account and the atoms are regarded as point scatterers, a simple picture can be seen in which the backscattered waves interfere with the forward wave to produce either peaks or troughs as illustrated by Fig. 2.2. This is an interference effect on the final state and results in an oscillatory feature seen in the EXAFS region to the right of Fig. 2.1.

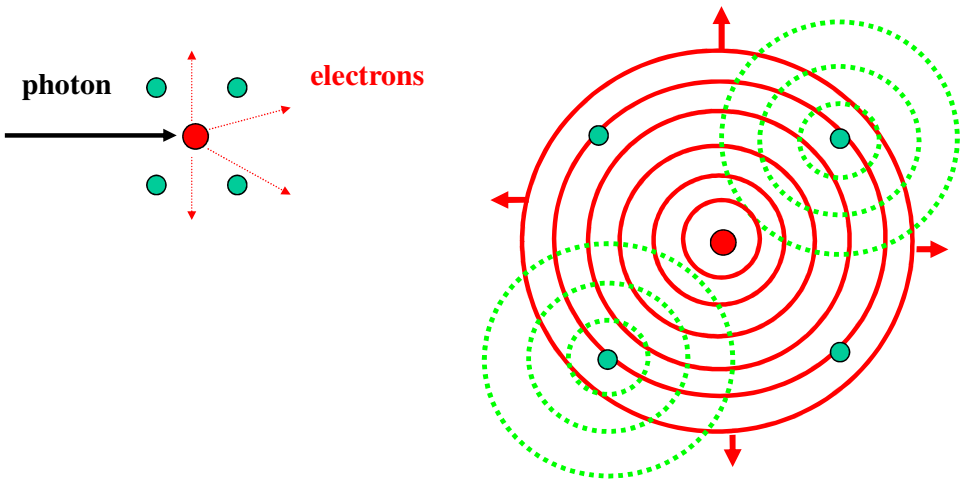

Fig. 2.2. Interference of photoelectrons in multi-atom system.[14]

The wavelength of the photoelectron is dependent on its energy and thus the phase of the back scattered wave at the central atom will change with the energy of the incoming photon. Since the backscattering amplitude and

phase are dependent on the type of atom causing the backscattering and its distance from the central atom, information regarding the coordination environment of the absorbing atom can be obtained by analyzing the absorption spectrum.[13]

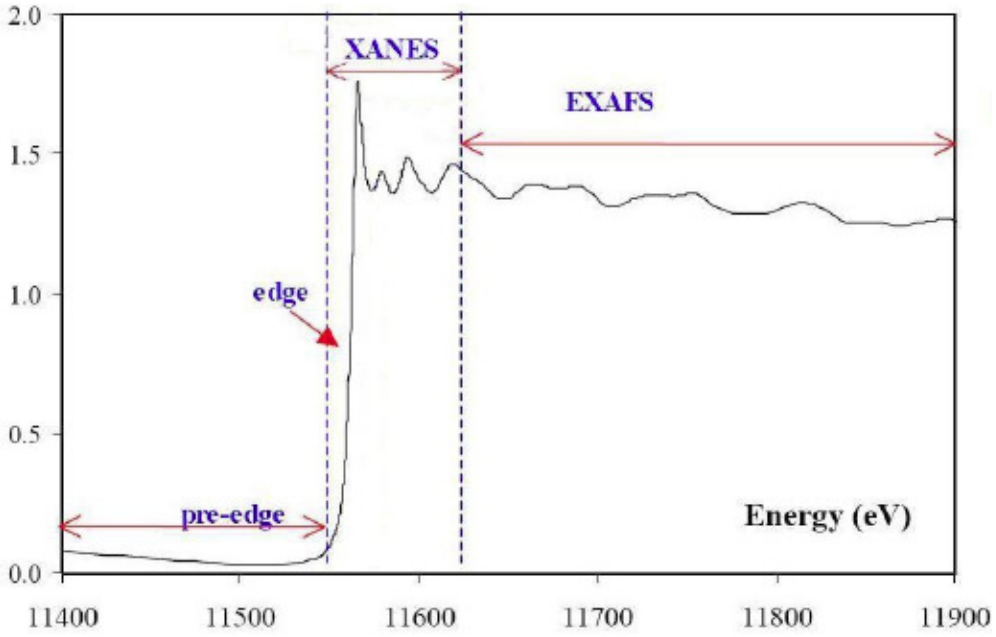

Fig. 2.3. Segmentation of Absorption Spectrum into pre-edge, XANES and EXAFS region.[13]

A typical XAFS spectrum is shown in Fig. 2.3 with the different regions labelled. The energy range of the absorption spectrum from the absorption edge till approximately 50 electron volts above the edge is termed as the XANES region, while the EXAFS region extends approximately 200 electron volts beyond the XANES region.

The XANES regime is where the oscillations contain information about the valance number, anti-bonding states etc within the atom. As illustrated in Fig.2.4, multiple scattering from various neighbours are dominant in XANES whereas single scattering from its direct neighbour is dominant in EXAFS. The EXAFS spectrum contains information about the number and species of neighbouring atoms as well as their distances away from the absorbing atom.

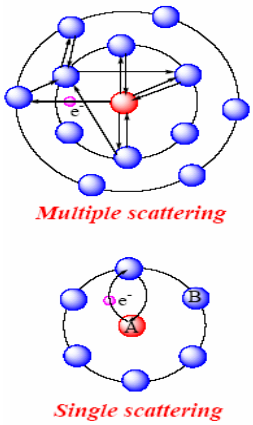

Fig. 2.4. Photoscattering Processes in XANES and EXAFS.[14]

2.2.1 XANES

The pre-edge absorption is usually due to electronic transitions of electrons from the lower core levels to the higher unfilled or half-filled molecular orbitals. These absorptions may be due to s→d orbital transitions or p→f orbital transitions. However, the probabilities for such transitions are usually not very high, thus resulting in a low absorption in the pre-edge region.[13] The x-ray absorption region near the edge is known as XANES.

XANES gives information on the valence state of the selected type of the atom in the sample. The local symmetry of its unoccupied orbitals can also be deduced in the shape and energy shift of the x-ray absorption edge itself.[13] Theoretically, the anti-bonding states, bonding information and even the Density of States (DOS) can be extracted from the XANES spectrum. However, the details of XANES are currently not very well understood, and there are no simple models describing the XANES features.

The different oxidation states of the sample would result in a chemical shift in the absorption edge. Thus, the position of the edge gives an indication of the oxidation state of the sample. Typically, as the oxidation state increases, the edge lies at a higher energy. This is because when the elements are oxidized, the valence electrons are more tightly bound to the nucleus, resulting in a higher energy required to remove the electron from its bound state.[15]

Since the XANES spectrum is also sensitive to the local geometry of the sample, there should be a distinct difference for different bond coordinations. For a sample of octahedral structure, due to its symmetry about its centre (centro-symmetry), no p-d mixing is allowed. Only quadrupole transitions are possible but by Fermi's golden rule, this transition probability is very low. This results in very little or an absent pre-edge feature in the XANES spectrum. When the structure is distorted from the octahedral structure, p-d mixing is allowed, resulting in dipole transitions in the pre-edge as well as quadrupole transitions. These results in a larger pre-edge peak and in a pure tetrahedral sample Thus, the pre-edge feature is indicative of geometry in the XANES structure.[15]

2.2.2 EXAFS

EXAFS is the region of the absorption spectrum roughly 50eV after the absorption edge till several hundred electron volts later. In EXAFS, we can determine the thermal or structural disorder of the atomic positions which are determined from the oscillatory part of the absorption coefficient above the major absorption edge. EXAFS is mainly caused by single scattering off the nearest neighbours, and this scattering effect is much better understood compared to XANES. The EXAFS equation[9]:

$$\chi(k) = \sum_j \frac{s_0^2 N_j F_j(k)}{kR_j^2} e^{-2k^2\sigma_j^2} e^{-2R_j/\lambda(k)} \sin[2kR_j + \delta_j(k)] \quad \text{--- (1)}$$

Where N_j = Coordination number, $\delta_j(k)$ = Phase shift, $F_j(k)$= Scattering amplitude, σ_j = Debye Waller factor, R_j =Bond length, s_0 = inelastic factor.

XAFS oscillations $\chi(k)$ are found to be proportional to $1/kR^2$ [spherical wave], N, $F_j(k)$, $\sin(2kR_j+\delta_j(k))$ [interference item], $\exp(-2k^2\sigma_j^2)$ [disorder factor] and $\exp(-2R_j/\lambda)$ [electron mean free path].

Within the neighbourhood of the element of interest, there is usually more than one type of scattering atom. Depending on the scattering atom, the scattering amplitude *f(k)* and the *δ(k)* varies. The EXAFS equation is useful for modelling the effects of scattering atoms around our absorbing element. Hence, we are able to determine *R*, *N* and the mean square disorder of neighbour distance σ^2. Thus, the measured fine structure will be a sum of the contributions from each scattering atom type. This is accommodated by taking a sum of the atoms in the neighbourhood, and *j* represents the individual coordination shell of identical atoms at approximately the same distance from the central atom. Since *f(k)* and *δ(k)* depends on the atomic number of the scattering atom, we can also determine the species of the scattering atom.[9]

2.3 XDD Beamline

The X-ray Development and Demonstration (XDD)[16,17] beam line and its experimental station are designed for general purpose diffractometry, fluorescence detection and absorption spectroscopy.

Fig. 2.5. Picture of XDD Beamline at SSLS[13]

The X-rays produced by the synchrotron are first directed to a focusing mirror, which is then sent to a monochromator, allowing x-rays of only a particular energy to pass through. Finally, x-rays of selected energy are allowed into the experimental hatch.[13] The optical layout of the XAFS facility in the XDD beamline is illustrated in Fig.2.6. Synchrotron radiation

beams from the superconducting bending magnet (4.5 Tesla) are confined by a front slit (slit1), focused horizontally and collimated vertically by a toroidal mirror, and monochromatized via a double-crystal monochromator.[10] The monochromatic beams pass through a UHV chamber, confined by an exit slit (slit2), and finally enter the experimental hutch where samples are mounted.[10] The sample position is 14 m long from the light source point. The Si (111) double crystal monochromator[18] covers an energy range from 2.5 to 10 keV which incorporates measurable elements in the periodic table: S to Zn, K-edge; Ru to Ta, L-edge; Pt to Bi, M-edge and the L-, M-edges of most rare earth elements.[10] The beam size is about 4 mm horizontally and 3 mm vertically at the sample position.[10] The 3rd order harmonic component was removed by a collimating mirror installed upstream of the monochromator which cuts off fluxes with energies higher than 10 keV.

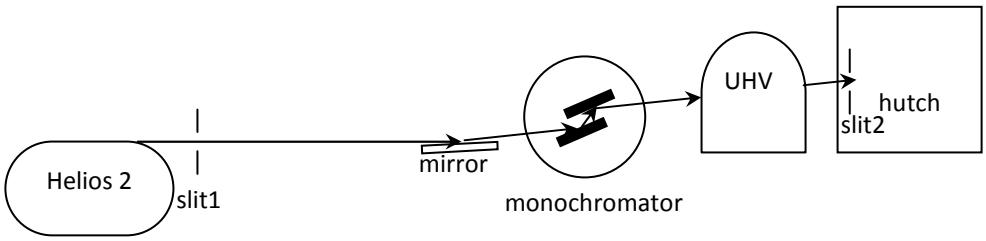

Fig. 2.6 Optical layout of the XAFS facility at the XDD beamline of SSLS.[14]

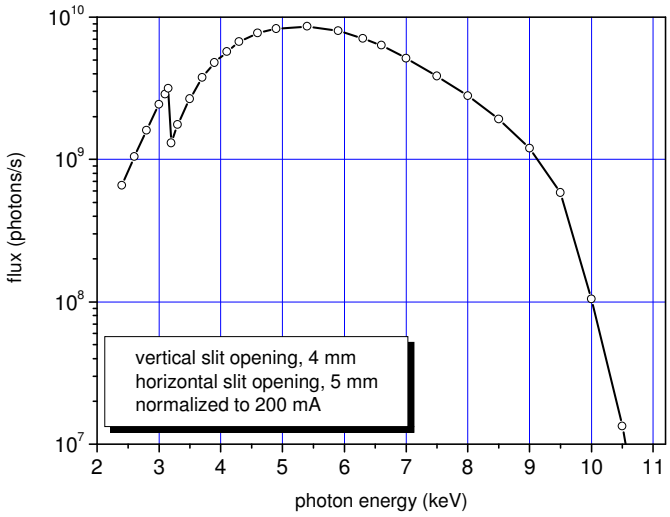

Fig. 2.7. Photon flux measured by an ion chamber at energies from 2.4 to 10.5 keV, vertical and front horizontal slit opening were set to 4 and 5 mm respectively. The flux was normalized to 200 mA of ring current.[10]

Inside the storage ring, electrons with energy of about 700 MeV are accelerated and orbited through 4.5 T dipoles in the Helios 2.[19] The flux estimated at the sample position of the XDD beamline is plotted in Fig. 2.7 at energies from 2.4 to 10.5 keV measured by the ionization chamber. The vertical and front horizontal slit opening at the front end were set to 4 and 5 mm, respectively, the flux was normalized to 200 mA ring current.[10] The photon flux is related to the critical energy (1.47 keV) of the synchrotron storage ring, and it falls significantly for energies higher than 8 keV. The drop at 3.2 keV is due to the argon absorption in air since there is a 20 mm long air path between the exit window and the ion chamber, and the measurements were performed in air.[10] The high photon flux from synchrotron radiation light source which is several orders of magnitude higher than that of the laboratory X-ray generators is necessary for XAFS experiments.

At higher energies than 10 keV, the photon count drops and is not suitable for XAFS experiments. Thus, experiments conducted at the SSLS XDD beamline are limited to elements with absorption edges (K- L- M-edges) in the range from about 4keV till 8.5keV.[13] Therefore, the list of elements suitable for XAFS measurements at the XDD beamline is displayed in Fig. 2.8. Some elements are measured at the K edges, while others are measured at the L or M edges.

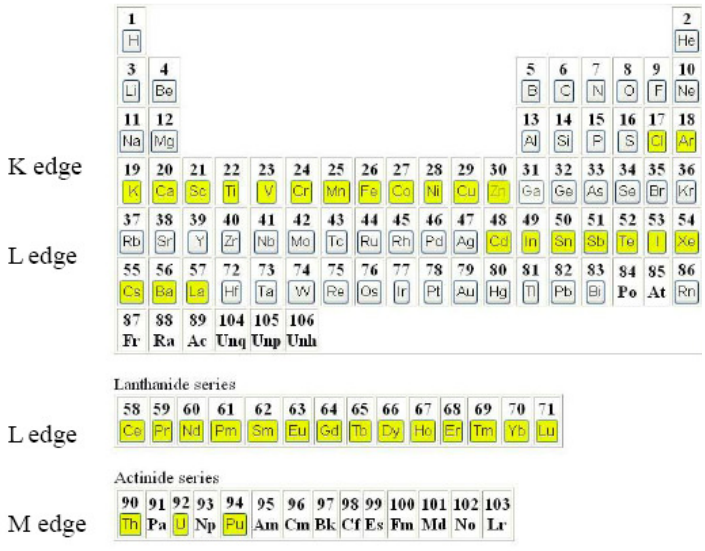

Fig. 2.8. Suitable elements for XAFS at XDD Beamline.[14]

2.4 Sample Requirements

The samples used for XAFS measurements at the XDD beamline are usually solid (crystalline or amorphous) samples, though XAFS can be applied even to liquid and gaseous samples. However, certain modifications must be made to the current experimental end station in order to do XAFS experiments for liquid and gaseous samples.[13]

For transmission mode measurements, the solid samples are ground to a powder of very fine particle size. The particle size is ideally less than 1 absorption length or roughly 400 mesh. The unit "mesh" is for description of particle size where 400 mesh indicates that there are 400 lines per inch in the wire grid.[13] By a simple conversion, 400 mesh indicates that the particle size is around 60 microns in diameter.[13] They are then either spread on scotch tape and folded a number of times or mixed with fine powders of BN or LiF and pressed into pellets.

If the method of detection is by Total Electron Yield (TEY), the sample has to be conductive, so it is sometimes spread on carbon tape, or ground into fine powder then mixed with graphite and pressed into pellets.[13] The gauge as to how thick the sample should be or how many folds of scotch tape to make, is dependent on the best signal to noise ratio for the element of interest whereby the absorption jump ratio is ideally around 1, as described in Fig. 2.9.

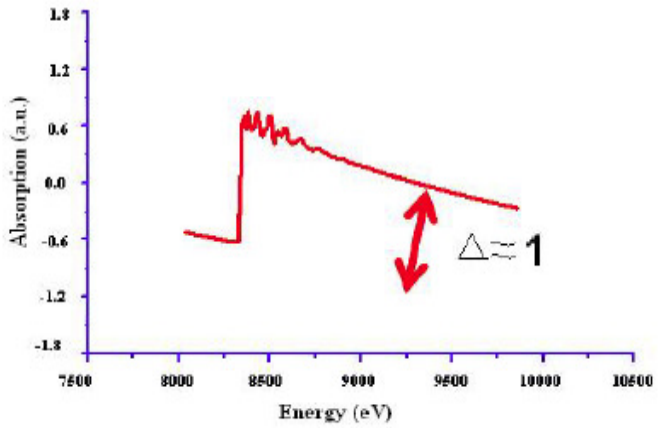

Fig. 2.9. Ideal Absorption Jump for XAFS Experiments.[13]

2.5 Methods of Detection

When x-rays interact with matter, several processes may occur as illustrated in Fig 2.10. The x-rays may end up scattered, transmitted, or absorbed and producing fluorescence x-rays and photoelectrons. X-rays that are not absorbed by the sample pass through the sample directly and are detected as transmitted x-rays.

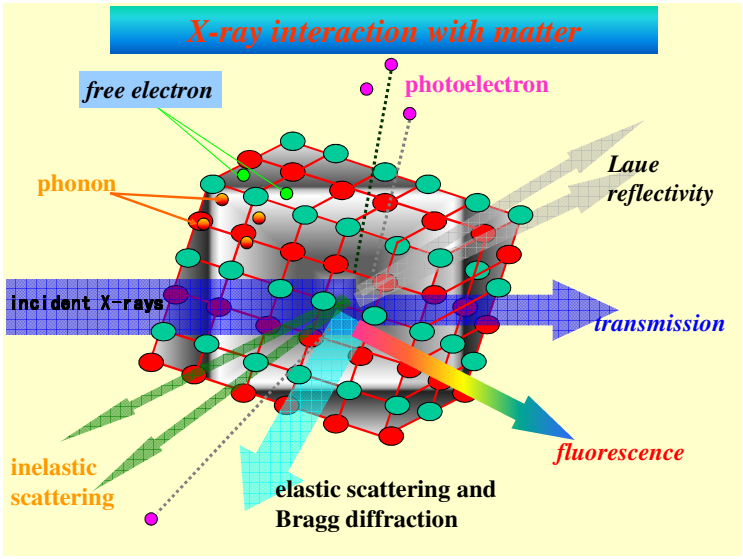

Fig. 2.10. Interaction of X-ray with matter.[14]

We can deduce the absorption of x-rays by the element of interest by either measuring the intensity of the transmitted x-rays, photoelectrons produced or the fluorescence photons produced. These methods of detection are namely measurements by Transmission, Total Electron Yield (TEY) and X-ray Fluorescence.[13] Our choice of method of detection is dependent on the concentration of our target element in the sample. Transmission is always the preferred technique but when the sample concentration is low (<5%), the absorption jump is low and the spectrum formed may have a large noise to signal ratio.[13] Hence, for dilute samples, we can adopt either TEY or X-ray Fluorescence methods for measurements. Fig. 2.11 shows a guide to what methods to use for different element concentrations. The electron yield decreases with increasing atomic number Z and the fluorescence yield increases with Z. This means that TEY is most effective

with lighter elements and is ineffective with heavier elements as the electron yield signal becomes too weak and vice versa for X-ray Fluorescence.

In the sections below, transmission measurement mode and X-ray Fluorescence measurement will be discussed in detail. TEY is excluded from the discussions since it is not utilized in the project.

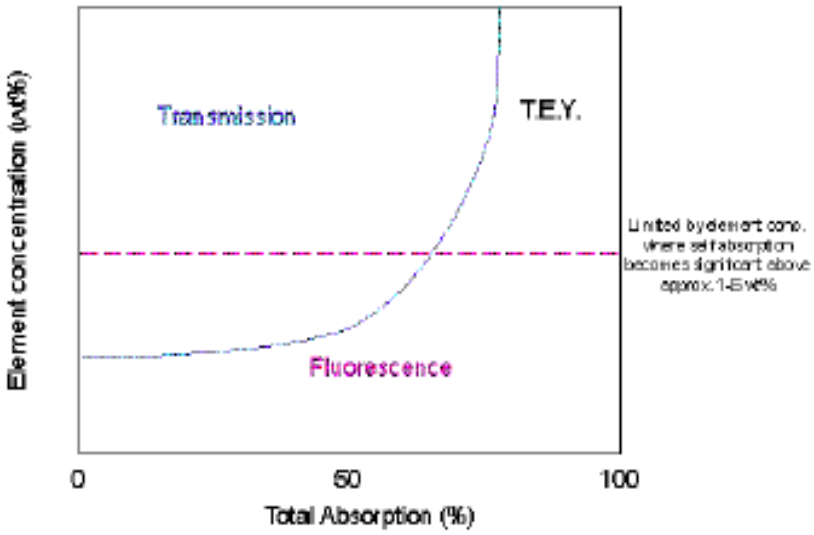

Fig. 2.11. XAFS methods of detection for different concentration.[20]

2.5.1 Transmission

Transmission measurement mode is preferred as very little statistical noise is introduced through the measurement technique. The sample needs to be totally homogeneous because the bulk properties of the sample are being measured and thickness effects become important. Particle size can also contribute to thickness effects unless it is considerably smaller than the absorption length.

The method of detection is to place the ionisation chambers in line with the sample and the incident x-ray. A typical experimental setup for XAFS transmission measurements at the XDD beamline is shown in Fig. 2.12. The x-rays enter the first ionisation chamber and the intensity of the incident x-ray (I_0) is measured. The x-rays is then partially absorbed by the sample and the transmitted x-rays enter the ionisation chamber 2 which measures

the intensity I. I, I_0 and the thickness of the sample t are related by Beer's law: $\mathbf{I=I_o e^{-\mu t}}$ where μ is the absorption coefficient of the sample. The limitation of this method is that the sample has to be of an appropriate thickness. If the sample is too thin, the photons just pass through the sample without interacting but if it is too thick, the absorption is too great that no photons enter Ionisation chamber 2.[13]

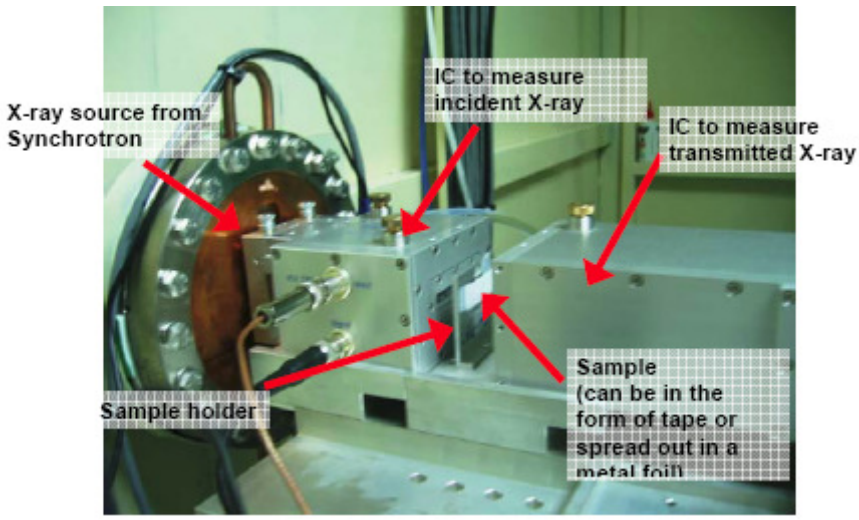

Fig. 2.12. Experimental Setup at XDD beamline for XAFS measurement by transmission.[13]

2.5.2 X-Ray Fluorescence

Below a certain level of concentration (<5%), the change in absorption before and after the edge will become indiscernible with the transmission technique.[13] In situations like this, XAFS measurements are performed in the fluorescence mode. The probability of fluorescence is proportional to the absorption probability but the fluorescence intensity that we measure has to travel back through the sample to get to the detector.[9] Since all matter attenuates x-rays, the fluorescence intensity, and therefore the XAFS oscillations, can be damped due to this self-absorption effect.[9] Thus, the fluorescence mode is not suitable for XAFS measurements when significant self absorption occurs. A schematic diagram of the Lytle detector used for

X-ray Fluorescence is shown in Fig. 2.13. The XDD beamline utilizes a home-made Lytle-type detector for X-ray Fluorescence measurements.

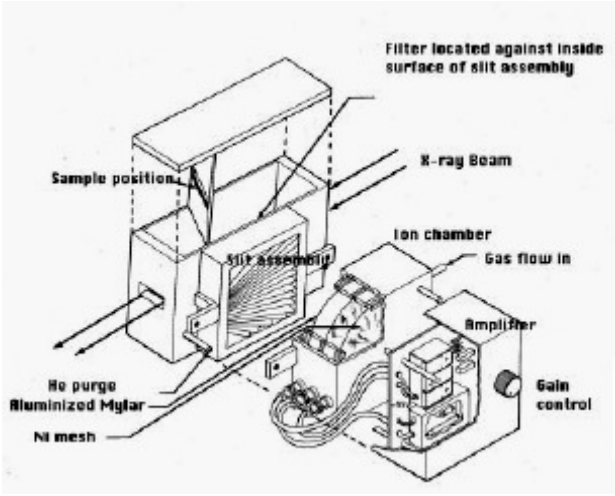

Fig. 2.13. Schematic Lytle Detector.[14]

Assuming that the sample is at 45° to both the incident beam and the fluorescence detector, the measured fluorescence intensity[14] goes as:

$$I_f = \frac{I_0 \varepsilon(\Omega/4\pi)\mu_x(E)}{\mu_t(E)+\mu_t(E_f)}(1-e^{-[\mu_t(E)+\mu_t(E_f)]d}) \quad \text{--- (2)}$$

Where ε = fluorescence efficiency, Ω = the solid angle of the detector, E_f = the energy of the fluorescent x-ray, $\mu_x(E)$ = the absorption from the element of interest, $\mu_t(E)$ = the *total* absorption in the sample: $\mu_t(E) = \mu_x(E) + \mu_{other}(E)$

For thin or dilute samples, the fluorescence intensity[14] will follow the expression:

$$I_f = I_0 \varepsilon(\Omega/4\pi)\mu_x(E)d \quad \text{where} \quad [\mu_t(E)+\mu_t(E_f)]d << 1 \qquad \text{---(3)}$$

For concentrated samples, $\mu_x(E)$ and $\mu_{other}(E)$ are comparable, and the XAFS will be severely damped by self-absorption. For thick and concentrated samples, the equation for the fluorescence intensity[14] will be:

$$I_f = \frac{I_0 \varepsilon(\Omega/4\pi)\mu_x(E)}{\mu_t(E)+\mu_t(E_f)} \quad \text{where} \quad [\mu_t(E)+\mu_t(E_f)]d >> 1 \qquad \text{---(4)}$$

2.6 Data Analysis

The WinXAS code[21] was used for data analysis. For samples measured with more than one scan, all scans were averaged to improve statistics. The spectra for XANES are sectioned accordingly to remove glitches. Each spectrum was normalized by applying linear fits to the pre and post-edge regions. A macro was recorded and employed for automatic data processing for all scan data to allow for precise comparability of results. The data analysis for EXAFS follows a standard procedure. Firstly, the spectra are subjected to Golay-Savitzky smoothing with polynomial of 0/1 degree. Normalization was performed by employing linear and polynormial fits to the pre-edge and post-edge regions of the absorption spectra respectively. The subsequent processing includes the E_0 selection, transforming from energy space to momentum (k) space, a 7-segment spline fit to post-edge region to extract XAFS functions, k^3 weighting to amplify the oscillation of the spectrum and Fourier transform (FT) from k space to real R space.[13] A macro was recorded and employed for the automatic data processing of all scan data.

In the FT, the appropriate XAFS functions in k space were extracted for Co, Cu, Ti and Mn K-edges respectively, k^3 weighted and a Bessel window function was employed. The data fit was performed in R space using phase shift and backscattering amplitude extracted from the TM-replaced ZnO model.[22] The model was constructed based on the wurtzite structure of ZnO where one Zn atom (central absorber) was replaced by the doped TM atoms. The inelastic factor, s_0, was determined by fitting to standard references and fixed.

References

1. X-ray characterization of Materials, edited by Eric Lifshin, Published by Wiley-Vch.
2. Surface characterization: a user's sourcebook, edited by D. Brune, Published by Wiley-Vch.
3. Physics of magnetism and magnetic materials, by K.H.J. Buschow and F.R. de Boer. Imprint New York : Kluwer Academic/Plenum Publishers, c2003.
4. Introduction to focused ion beams : instrumentation, theory, techniques and practice, edited by Lucille A. Giannuzzi, Fred A. Stevie. Imprint New York : Springer, c2005.
5. Surface and thin film analysis : principles, instrumentation, applicatons, edited by H. Bubert and H. Jenett. Imprint Weinheim: Wiley-VCH, 2002.
6. Scanning electron microscopy and x-ray microanalysis, by Joseph I. Goldstein. Imprint New York : Kluwer Academic/Plenum Publishers, c2003. Edition 3rd ed.
7. Scanning electron microscopy, X-ray microanalysis, and analytical electron microscopy: a laboratory workbook / Charles E. Lyman. Imprint New York : Plenum Press , c1990.
8. Handbook of silicon semiconductor metrology, edited by Alain C. Diebold. Imprint New York : Marcel Dekker, 2001.
9. Matthew Newville, Consortium for Advanced Radiation Sources, University of Chicago, (2004). Fundamentals of XAFS. Retrieved on September 30, 2004, from http://cars9.uchicago.edu/xafs/xas_fun/xas_fundamentals.pdf
10. Tao Liu, Zhihua Yong and Andrew T. S. Wee, Hairuo Xu and Weeshong Chin, Ping Yang, ICMAT 2007.
11. Some basic principles of synchrotron radiation. Anonio Juarez, AmLm group, 2001
12. Yong Zhihua, Andrew Wee, Gao Xinyu, National University of Singapore, Department of Physics, *Synchrotron radiation studies of Cobalt doped Dilute Magnetic Semi-conductors*, Honours Year Project 2005 Nov.
13. Toh Ping Yong, Andrew Wee, Liu Tao, National University of Singapore, Department of Physics, *XAFS Studies on Eu, Mn and Co doped ZnO Nanoparticles*, Honours Year Project 2006 April.
14. Some basic and practical aspects of X-ray Absorption Fine Structure Spectroscopy based on synchrotron radiation, a presentation by Dr Liu Tao, National University of Singapore, Department of Physics, 2005 Sept.
15. Course Characterization Techniques in Heterogeneous Catalysis January 5th, 2004 JeroenA. vanBokhoven, Retrieved on Jan 2006, from http://prins00.ethz.ch/Teaching/xanespdf.pdf
16. P. Yang, D. Lu, R. Kumar and H.O. Moser, Nucl. Instr. and Meth. in Phys. Res. B **238,** 310 (2005).
17. SSLS official website, XDD beamline details:

http://ssls.nus.edu.sg/facility/beamlines/xdd/xdd.htm
18. Farideh Jalilehvand, Ph.D. Assistant Professor University of Calgary. (2002). *X-ray Absorption Spectroscopy (XANES, EXAFS) Synchrotron*. Retrieved on September 30, 2004, from http://www.chem.ucalgary.ca/research/groups/faridehj/index.html
19. X. Yu, O. Wihelmi, H.O. Moser, J. Electron Spectrosc. Relat. Phenom., **144**, 1031(2005).
20. Carrying out an EXAFS Experiment: http://srs.dl.ac.uk/xrs/Stations/basics/basic_EXAFS.htm
21. Ressler, T. J. Physique IV, **7**, C2 (1997).
22. Tao Liu, Hairuo Xu, Wee Shong Chin, Zhihua Yong, and Andrew T. S. Wee, J. Phys. Chem C, **112**, 3489 (2008)

Chapter 3

Fabrication of 3d Metal Doped ZnO thin films

3.1 Reactive Radio-frequency magnetron sputtering

The planar magnetron sputtering source was invented at the beginning of the seventies.[1,2,3] Magnetron sputtering became a well established commercial technique for the deposition of metal, optical films and semiconductors films many years later. It has many important advantages over other thin-film deposition methods such as evaporation, chemical vapour deposition (CVD) or spray pyrolysis, namely[3,4]: 1) Low substrate temperatures (down to room temperature); 2) Good adhesion and high purity of films on substrates; 3) High deposition rates; 4) High uniformity of thickness of the deposited films; 5) Good controllability and long-term stability of the process; 6) Good ability to maintain the stoichiometry of original target; 7) Low cost; 8) Scalability to large areas; 9) Better reproducibility of films.

Two excitation modes are used in magnetron sputtering, namely direct current (dc) and radio-frequency (rf) modes. If a chemical redox reaction occurs, it is called reactive magnetron sputtering. The reactive rf sputtering mode was used in our work since it is more suitable for insulating targets.

3.2 Principles of RF magnetron sputtering

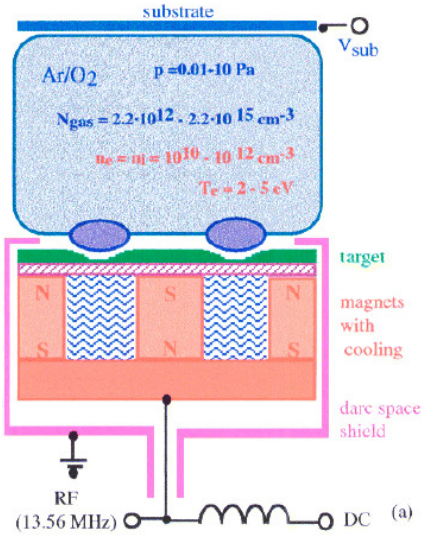

Fig. 3.1. Schematic diagram of a magnetic sputtering configuration for simultaneous rf and dc excitation.[3]

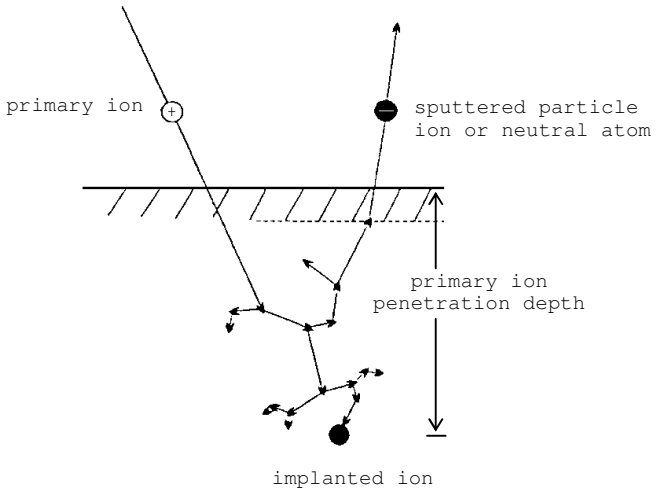

Fig. 3.2. Schematic of the ion-solid interactions and the sputtering process.[4]

A schematic diagram of magnetron sputtering configuration is shown in Fig. 3.1 and the process is illustrated in Fig. 3.2. When a high

energy ion bombards a target, it knocks atoms near the target surface from their equilibrium positions, causing these atoms to move around in the material and undergo further collisions, and finally causing the ejection of atoms through the target surface. This ejection process is known as sputtering. Reflected ions, neutral atoms and secondary electrons may also be produced along with the target atoms. The ejected target atoms are then made to condense on a substrate to form a thin film.[4]

In rf sputtering, which is suitable for both conducting and insulating targets, a high frequency generator (13.56MHz) is connected between the metal electrodes where the target is placed.[5] Neutral gas is introduced into the vacuum chamber. When a large rf potential (~1-1.5 kV) is applied across the metal electrodes, glow discharge can be initiated and electrons oscillating in the alternating field have sufficient energy to cause further ionizing collisions, and the plasma which is a complex gaseous state of matter comprising of free radicals, electrons, photons, ions, and various neutral species can be self-sustained. The large rf potential required to initiate the discharge is no longer necessary once it has been attained.

Due to their higher mobility as compared to ions, many more electrons will reach the target surface during the positive half-cycle than ions during the negative half-cycle, and the target, being mounted capacitively to the rf source, will become self-biased negatively. [4] The negative dc potential on the target surface then repels many electrons from the vicinity of this surface, creating a torus-like plasma in front of the target. In the rf discharge, the electrons are able to follow the rf frequency of 13.56MHz while the ions are not, due to their large inertia. This kind of excitation is much more effective compared to ionization by non-oscillating secondary electrons in the dc discharge, leading to lower target voltages in the rf discharge. However, the magnetic confinement of the electrons is not as good due to the negative dc

potential on the target surface.[3] The collection of charged particles in the plasma will bombard the target and sputtering can be achieved. The plasma will not form at frequencies less than 10 kHz and 13.56 MHz is the frequency generally used for rf sputtering. [4]

Magnetic field effects are used in sputtering systems. In the conventional sputtering systems, electrons escaping from the inter-electrode space as a result of random collisions will be lost to the walls and no longer oscillate in the rf field. Thus, there will be insufficient electrons in the plasma to cause ionization, leading to a loss to the glow. To minimize this loss, a magnet is placed behind the metal electrodes. The purpose of using a magnetic field in a sputtering system is to constrain the electrons, and cause them to produce more ionization. [4] The use of magnetic field in sputtering is termed as magnetron sputtering and this is particularly useful where high deposition rates and low substrate temperatures are required.[5]

The basic feature of a magnetron discharge is the confinement of the plasma in front of the target and this can be achieved by the combination of electric and magnetic fields. The magnetic field is parallel to the target surface and orthogonal to the electric field. [5] The magnetic field strength is adjusted in such a way (about 20 to 200mT) that the electrons are significantly influenced by the magnetic field while the ions are not. The electrons perform cycloidal orbits in the crossed electric and magnetic fields, leading to very high ionization efficiency. Thus, magnetron discharges can be sustained at much lower pressures ($<10^{-2}$ Pa) and/or higher current densities than the glow discharges without magnetic assistance. [3] The rf system requires an impedance matching network to ensure maximum effective power delivered to the electrodes. Adequate grounding of the substrate assembly is necessary to avoid undesirable rf voltages developing on the surface. [4]

The potential distribution in the discharge between the target and the substrate is essential for the sputtering and the deposition of the film. This potential distribution determines the energies of the ions and neutral species which contribute to the deposition process. The external discharge parameters such as working pressure, discharge power and design of the magnetic fields (i.e. balanced or unbalanced magnetrons) influence the potential distribution and hence the particle energies. The potential distribution for rf excitation is shown schematically in Fig. 3.3. [3]

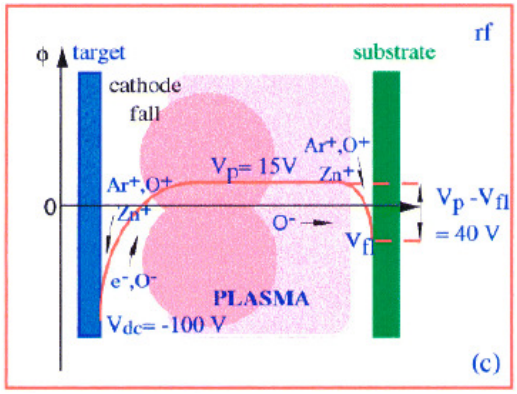

Fig. 3.3. Potential distribution in a magnetron sputtering discharge, excited by rf. [3]

The working gas pressure typically ranges from a 10^{-2}-10^{-3} Torr, depending on factors such as target material, rf voltage etc. If the working gas pressure in the rf system is too low, the electrons in the plasma do not cause sufficient ionizations. On the other hand, if the gas pressure is too high, the electrons are slowed by elastic collisions, resulting in insufficient energy to cause ionizations. In addition, the ions generated may not have enough energy to produce secondary electrons when they strike the target surface. For both situations, the plasma will not appear stable.[4]

Usually, films sputtered at room temperatures are amorphous but an increase in substrate temperature or post-deposition heat treatment

improves the crystalinity and grain size. The quality of the films depends on various deposition parameters such as plasma conditions, sputtering rate, substrate temperature, sputtering gas mixture, sputtering pressure, etc. [5]

3.3 Discovery-18 Deposition system

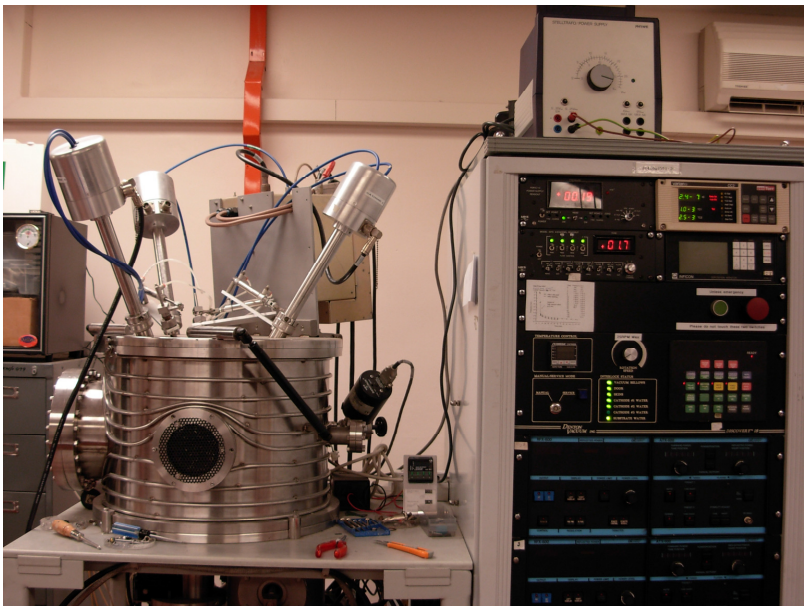

Fig. 3.4. Discovery-18 Deposition system and control panel

The sputtering system utilized in the fabrication of the doped ZnO thin films is the Discovery-18 Deposition system shown in Fig. 3.4. It is a semi-automatic system that has essentially all the features described in the above section. It has three planar magnetron sputter sources, with rf/dc capability, allowing multi-target sputtering of conducting and insulating targets to be done simultaneously. In addition, it is equipped with a rf-biasable, rotatable substrate stage. Substrate heating is also possible to 400 °C. The pumping assembly comprises of one rotary pump which serves as a backing pump for the turbomolecular pump. The chamber can be pumped down to high vacuum pressures of 10^{-7} torr. The total flow rate of the sputtering gases is controlled by their

respective mass flow controllers (100 sccm full scale). The chamber is connected to a water cooling system.[4]

3.4 Cleaning and preparation of Si and glass substrates

Silicon (100) wafers and thin glass slides are used as substrates for deposition. Silicon wafers are selected as it is the most widely used in semiconductor industry and also due to its low cost. Thin glass slides are used to study the contrast in the textures and properties of the films grown.

Si(100) substrates and glass slides were cleaned chemically before mounting in the vacuum chamber. A clean substrate that is free from impurities and oil layer will facilitate epitaxial growth and minimize stacking faults as well as pin holes in the resulting film.

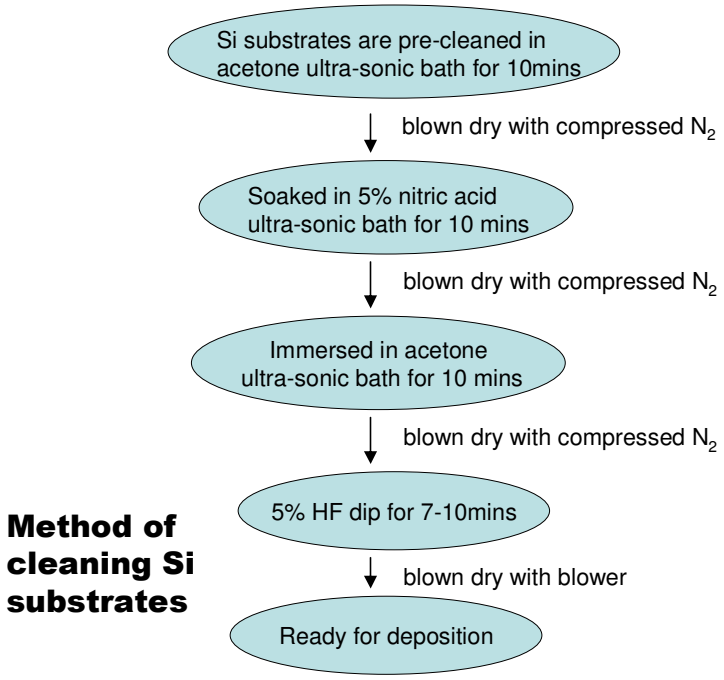

Fig. 3.5. Schematic diagram of cleaning Si substrates (Method 1)

Two methods of cleaning Si substrates were used. In the first method, the Si substrates are cleaned using the following sequence as illustrated in Fig. 3.5. They are first pre-cleaned ultrasonically in acetone for 10 minutes and blow dried using compressed nitrogen gas to remove most of the dust particles, oil molecules, fibers and organic compounds on the sample surfaces. Next, the Si substrates were immersed in 5% nitric acid ultra-sonic bath for 10 minutes to remove the inorganic contaminants. They were blown dry using compressed nitrogen gas. After this, the Si substrates were washed ultra-sonically in acetone for 10 more minutes to remove excess nitric acid left on the surfaces. They were blown dry using compressed nitrogen gas before being subjected to a 5% HF dip for about 7 to 10 minutes to dissolve any remaining native silicon dioxide layer. They are then blown dry with a blower.

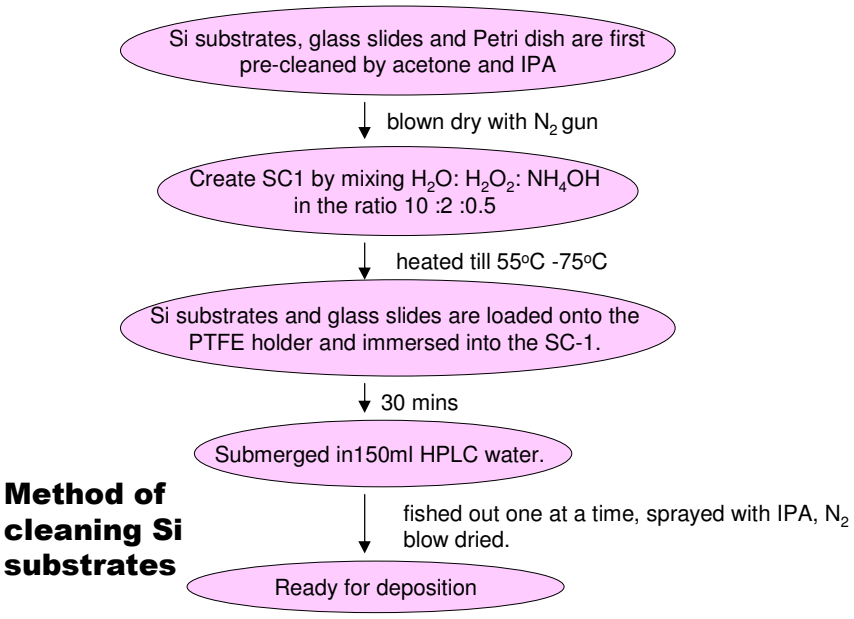

Fig. 3.6. Schematic diagram of cleaning Si substrates (Method 2)

In the second method[6] illustrated in Fig. 3.6, the Si substrates, glass slides and a Petri dish were first pre-cleaned by acetone and IPA (isopropyl alcohol), followed by N_2 blow drying. After this, the substrates are stored in a clean petri dish. The SC-1 solution was prepared by mixing H_2O: H_2O_2: NH_4OH in the ratio 10 :2 :0.5 in a 250ml beaker dedicated to SC-1. The beaker containing SC-1 solution and PTFE holder are heated on a hot plate till the temperature of the solution reaches 55°C to 75°C. When the desired temperature is reached, Si substrates and glass slides are loaded onto the PTFE holder and immersed into the SC-1 solution.

After soaking for 30 minutes, the PTFE holder together with the Si substrates and glass slides are removed and immersed into a second clean beaker containing 150ml HPLC (High-performance liquid chromatography) water. The substrates and glass slides are fished out one at a time, sprayed with IPA and finally N_2 blow dried. The Si

substrates and glass slides are put back into the petri dish and are ready for deposition.

3.5 Thin film deposition

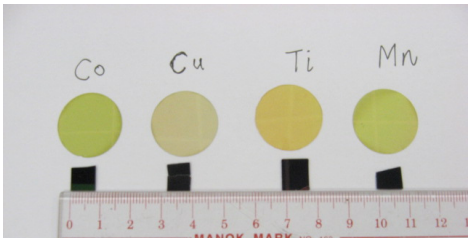

Fig. 3.7. TM-doped ZnO thin films deposited on round glass slides and Si(100). (Left to Right: TM stands for Co, Cu Ti and Mn)

All the thin films of TM (Ti, Mn, Co and Cu)-doped ZnO in our work were fabricated by reactive radio-frequency magnetron sputtering from a commercial ZnO target of 99.995% purity with a small plate of pure metal plate (Ti, Mn, Co or Cu) attached. A ZnO target is selected instead of Zn metallic target since the control of film stochiometry is easier with oxide targets, alleviating the need for high temperature and post-deposition annealing.[5] The concentration of TM doped into the samples was changed by changing the size of the plate. Fig. 3.7 shows a photograph of the Ti, Mn, Co and Cu-doped thin films deposited on round glass slides and Si(100) substrates. The deposited films on the glass/ substrates show different colors due to different thickness and perhaps due to different elemental compositions.

A low-temperature ZnO buffer layer is first induced between the Si(100) substrate/glass slides and ZnO film to reduce the lattice mismatch between ZnO and Si(100)/glass slides. Next, a high-temperature ZnO layer is deposited on this buffer layer to obtain a high-quality thin film. Reports[7,8,9] have shown that there is marked improvement in both the optical properties and crystalline quality

achieved in high-temperature ZnO layers on the low-temperature (LT) ZnO layer/ Si through a two-step growth using an RF magnetron sputtering system. Photoluminescence (PL) spectra taken of the ZnO film with LT-grown ZnO layer at room temperature and 10K both showed the remarkably improved features including narrower FWHM of exciton emission, suppression of defect-induced visible emission, and appearance of free exciton peak, when compared with the PL spectra of the ZnO directly grown on Si.[7]

In the experiments, the chamber is first pumped down to 10^{-6} to10^{-7} Torr and the voltage for sputtering is set at around 28V. The target was first pre-sputtered for 6 to 8 minutes to clean its surface at 200^{o}C. Buffer layers were next created on the Si(100) substrates and glass slides at 200^{o}C for 2 minutes at a deposition power of 150W. The temperature of the heater was then raised to 400^{o}C. The target was pre-sputtered again for 3 minutes at 400^{o}C before a further 1 hour of sputtering at 400^{o}C at a deposition power of 150W; thin films of a certain thickness were formed. The films were deposited in high vacuum at different ambient atmospheres (100% argon, a mixture of 85% argon and 15% nitrogen and a mixture of 80% argon and 20% oxygen) at a pressure of 1.0 - 2.0mTorr. The gas flow was set at 18.7 - 21.0sccm (atm cm^3/min). The target to substrate distance is fixed throughout all the experiments.

References

1. Schiller S, Heisig U and Goedicke K, Vakuum-Technik **27**, 51 (1978)
2. Schiller S, Heisig U and Goedicke K, Vakuum-Technik **27**, 75 (1978)
3. Klaus Ellmer, J. Phy. D:Appl. Phys **33**, R17 (2000)
4. Year 3 Physics laboratory manual, NUS, on synthesis of thin films by Reactive RF Magnetron Sputtering
5. H. L. Hartnagel, A. L. Dawar, A. K. Jain, Semiconducting Transparent Thin Films, published by Iop Institute of Physics, January 1995.
6. SC1 cleaning procedure manual prepared by ONDL laboratory, physics department, NUS.

7. Sang-Hun Jeong, Il-Soo Kim, Jae-keun Kim, Byung-Teak Lee, J. Cryst. Growth **264**, 327 (2004)
8. J.F. Yan, Y.M. Lua, Y.C. Liu, H.W. Liang, B.H. Li, D.Z. Shen, J.Y. Zhang, X.W. Fan, J. Cryst. Growth **266**, 505 (2004)
9. T.E. Park, B.H.Kong, H.K.Cho, D.J.Park, J.Y.Lee, Physica B, **376**, 735 (2006).

Chapter 4

Structural Properties of Doped ZnO thin films

In this chapter, the characterization of doped ZnO films by several techniques will be presented, namely profilometry measurements (section 4.1), X-ray fluorescence (section 4.2), scanning electron microscopy (SEM) (section 4.3), X-ray diffraction (XRD) (section 4.4) and secondary ion mass spectrometry (SIMS) (section 4.5). These characterization techniques give complementary analyses of the different structural properties of TM-doped ZnO films.

4.1 Profilometry measurements

The thickness of the films was measured using a Alpha-step 500 Profilometer. Before measuring the thickness, a step must be first created. This step was created before deposition of the films by drawing a thin line using a transparency marker on the Si (100) substrate. After deposition, the marker line was removed using a cotton bud soaked in acetone. The film deposited on this line can thus be removed and a step is created. The thickness of the films is measured at least twice at 2 different line sections and the average is taken. The errors are calculated by the standard deviation method. The results are tabulated in the Table 4.1.

Table. 4.1. Thickness of TM-doped films and the atmosphere under which they are fabricated. (The other experimental parameters are listed in Section 3.5.)

Samples	**Thickness of Films/ Å**	**Atmosphere**
ZnO	1806.7±15	85%Ar + 15%N_2
$Zn_{0.985}Co_{0.015}O$	5657.5±61	85%Ar + 15%N_2
$Zn_{0.979}Co_{0.021}O$	5535.5±50	85%Ar + 15%N_2
$Zn_{0.977}Co_{0.023}O$	6434.7±4	85%Ar + 15%N_2
$Zn_{0.961}Co_{0.039}O$	3583.0±11	80%Ar + 20%O_2
$Zn_{0.809}Co_{0.191}O$	7757.0±15	85%Ar + 15%N_2
$Zn_{0.790}Co_{0.210}O$	6513.5±3	Ar
$Zn_{0.987}Cu_{0.013}O$	9926.0±48	Ar
$Zn_{0.986}Cu_{0.014}O$	8084.0±40	85%Ar + 15%N_2
$Zn_{0.976}Cu_{0.024}O$	7463.7±28	85%Ar + 15%N_2
$Zn_{0.942}Cu_{0.058}O$	8887.5±40	Ar
$Zn_{0.812}Cu_{0.188}O$	9856.3±111	85%Ar + 15%N_2
$Zn_{0.754}Cu_{0.246}O$	10370.0±20	Ar
$Zn_{0.996}Ti_{0.004}O$	6406.5±64	85%Ar + 15%N_2
$Zn_{0.994}Ti_{0.006}O$	3790.0±33	80%Ar + 20%O_2
$Zn_{0.972}Ti_{0.028}O$	5053.0±48	85%Ar + 15%N_2
$Zn_{0.933}Ti_{0.067}O$	5661.0±58	Ar
$Zn_{0.999}Mn_{0.001}O$	6914.0±50	85%Ar + 15%N_2
$Zn_{0.978}Mn_{0.022}O$	4372.0±20	80%Ar + 20%O_2
$Zn_{0.963}Mn_{0.037}O$	5834.0±28	Ar

4.2 X-Ray Fluorescence (XRF)

X-ray fluorescence studies were performed at the Phase Contrast Imaging (PCI) beamline[1] at SSLS. The penetration depth of the hard X-rays used in XRF is in the μm range; hence XRF probes the bulk of the films. Fig. 4.1, 4.2, 4.3 and 4.4 show the normalized XRF spectra of the TM-doped ZnO films where TM is Co, Cu, Ti and Mn, respectively. Ar detected by XRF originates from the career gas absorbed by the samples while Cr and Fe contaminants are from the stainless steel sample holder. A calibrated sample $Zn_{0.92}Co_{0.02}Cu_{0.02}Mn_{0.02}Ti_{0.02}O$ was first prepared by mixing ZnO, Co_3O_4, MnO_2, TiO_2 and CuO powders together and XRF measurement was performed to determine the accurate composition. By comparing the areas under the Zn K_α and TM K_α peaks and comparing with the calibrated sample of known concentration using equation (1) below, the TM composition x was derived. Table 4.1 tabulates the concentrations of all the samples determined using XRF measurements.

$$\frac{x}{x'} = \frac{A}{A'} \qquad \text{---- (1)}$$

where A = area of TM K_α peak: area of Zn K_α peak in the TM-doped ZnO film

A' = area of TM K_α peak: area of Zn K_α peak in the calibrated sample tabulated in Table 4.2

x′ = composition of TM in calibrated sample = 0.02

Table. 4.2. Ratio of areas of TM K_α peak to area of Zn K_α peak in the calibrated sample $Zn_{0.92}Co_{0.02}Cu_{0.02}Mn_{0.02}Ti_{0.02}O$. x′ for all TM in sample are 0.02±0.002.

TM	Co	Cu	Ti	Mn
A'	0.119	0.090	0.024	0.076

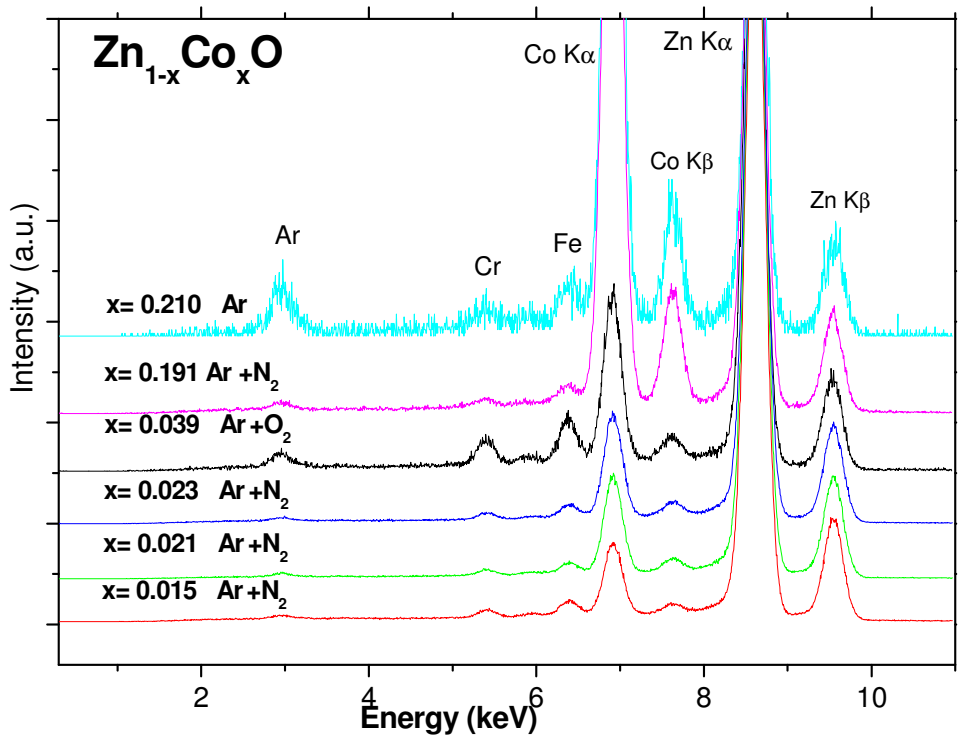

Fig. 4.1. Normalized X-Ray Fluorescence spectra of the Zn $_{1-x}$Co$_x$O films.

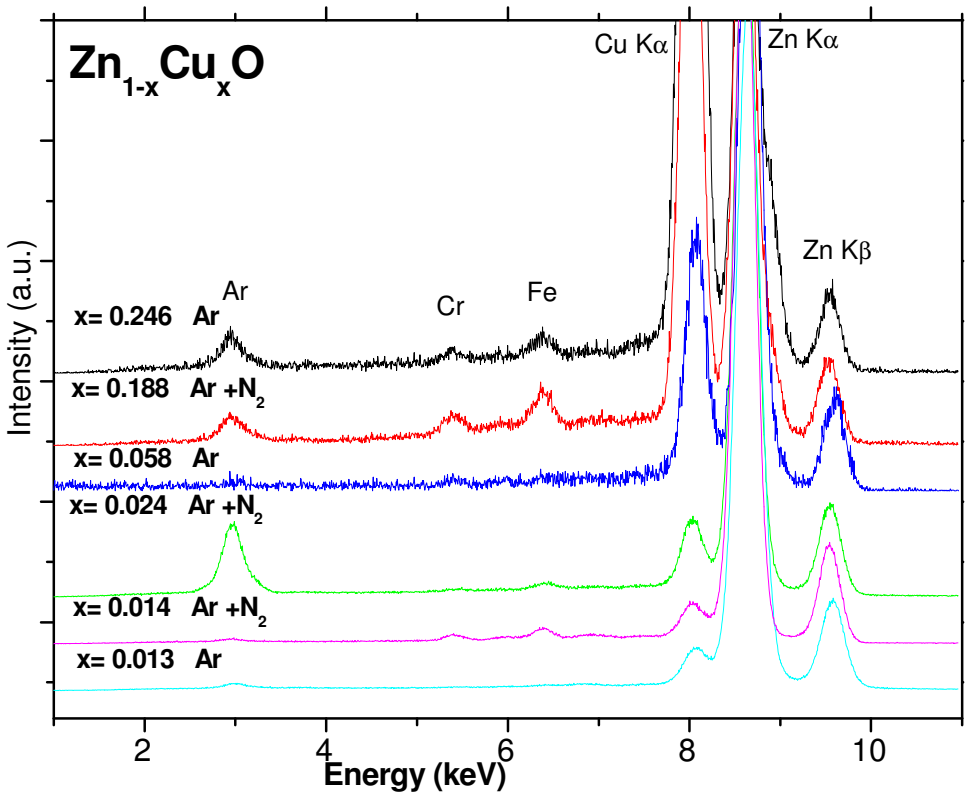

Fig. 4.2. Normalized X-Ray Fluorescence spectra of the Zn $_{1-x}$Cu$_x$O films.

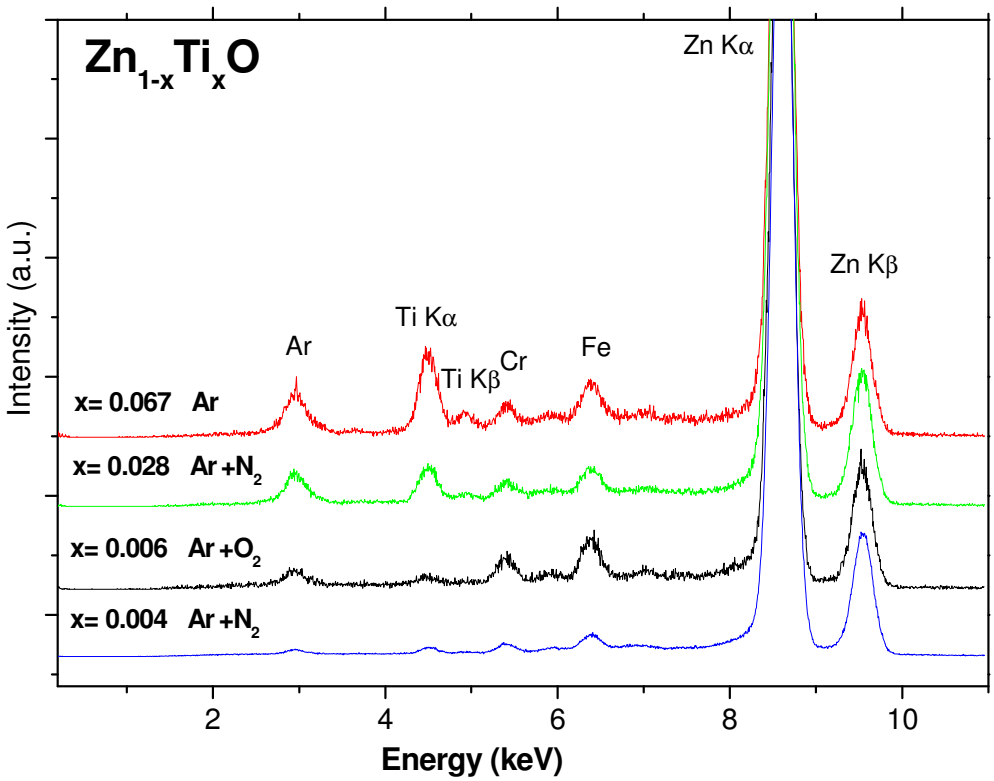

Fig. 4.3. Normalized X-Ray Fluorescence spectra of the $Zn_{1-x}Ti_xO$ films.

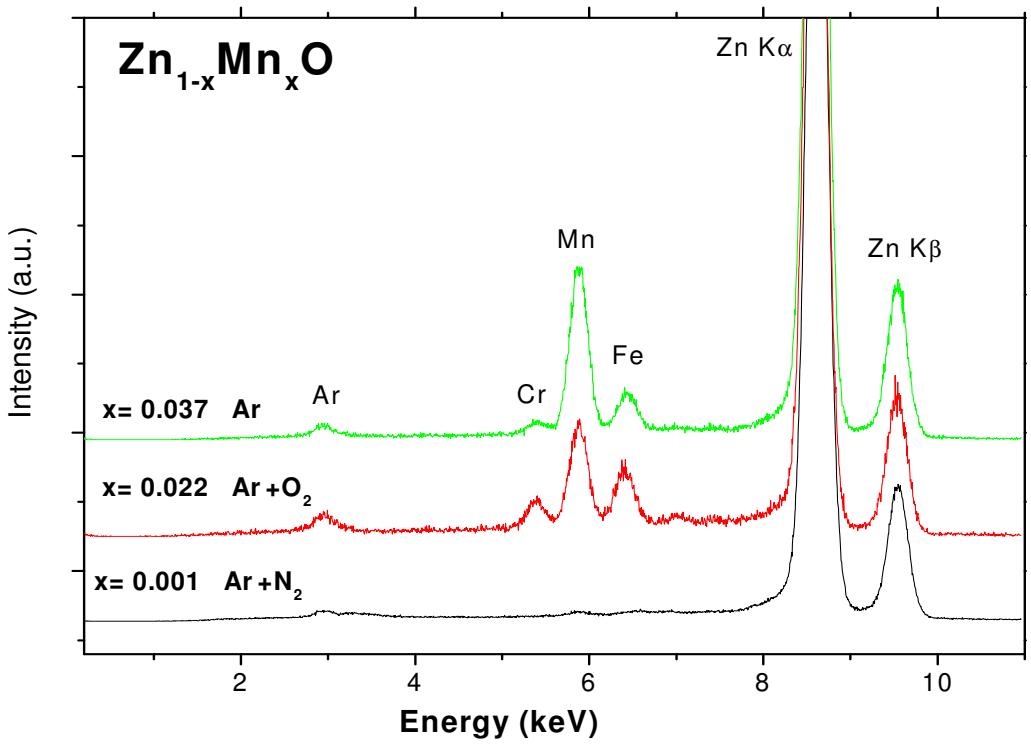

Fig. 4.4. Normalized X-Ray Fluorescence spectra of the $Zn_{1-x}Mn_xO$ films.

4.3 Scanning Electron Microscopy (SEM)

SEM measurements were done using a JEOL JSM 6700F system. The surface morphology of Co, Cu, Ti and Mn-doped ZnO films deposited at 400^{o}C was imaged at normal e-beam incidence as shown in Figs. 4.5, 4.6, 4.7 and 4.8. In general, the surfaces of the films look smooth at low magnification and particles can be observed at high magnification. The Co, Cu and Ti-doped ZnO films have relatively small and slightly elongated spherical grain structure. The Mn-doped ZnO films, on the other hand, have a mixture of small, spherical and blade-like grain structures. The images at high magnification also display ring hexagonal structures of the ZnO compound which are most evident in Fig. 4.5(c) at 50,000 magnification and Fig. 4.6(c) at 100,000 magnification. This confirms the hexagonal wurtzite structure of ZnO.[2]

Fig. 4.9 shows the cross-sectional view of a typical Cu-doped ZnO film. A preferred vertical growth of the ZnO nanorods on Si (100) substrate is observed. The thickness of the film is measured to be 768.0nm, which is of approximately 2.9% different from the value measured by profilometry. This implies that both the SEM and profilometry give very close thickness measurements.

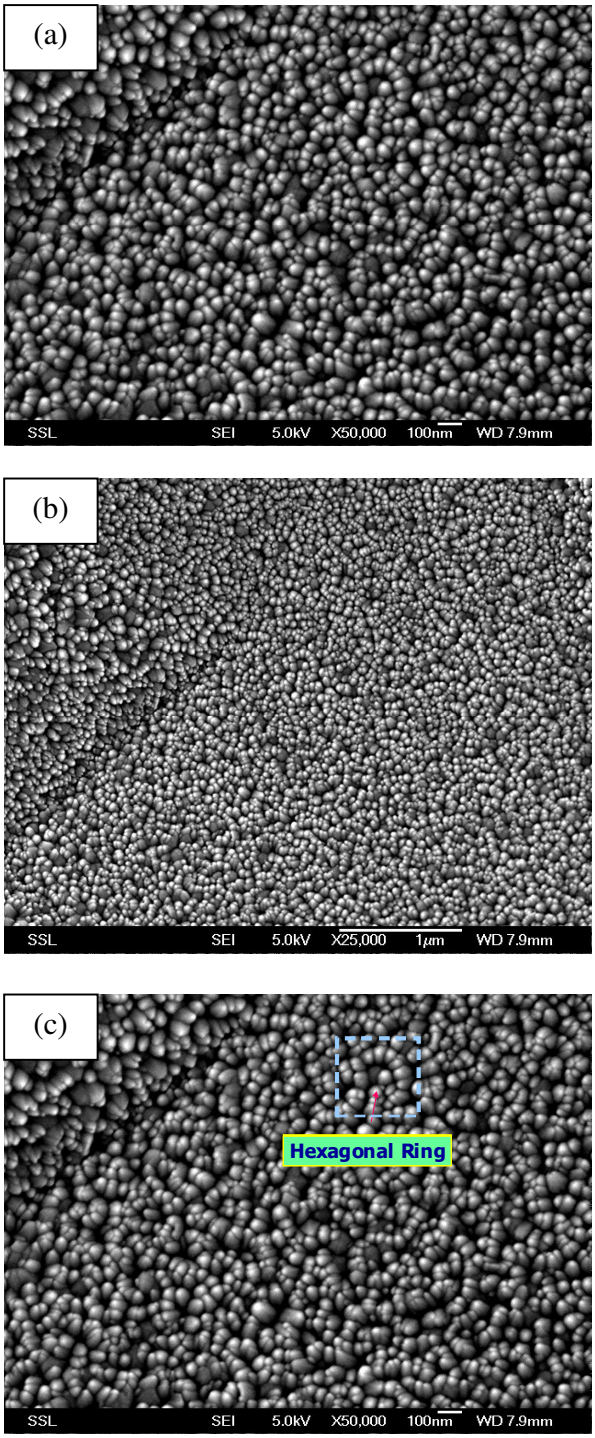

Fig. 4.5. SEM images of (a) Co-doped ZnO film deposited on Si (100) at high magnification, (b) Co-doped ZnO film at low magnification and (c) hexagonal ring structure drawn on (a).

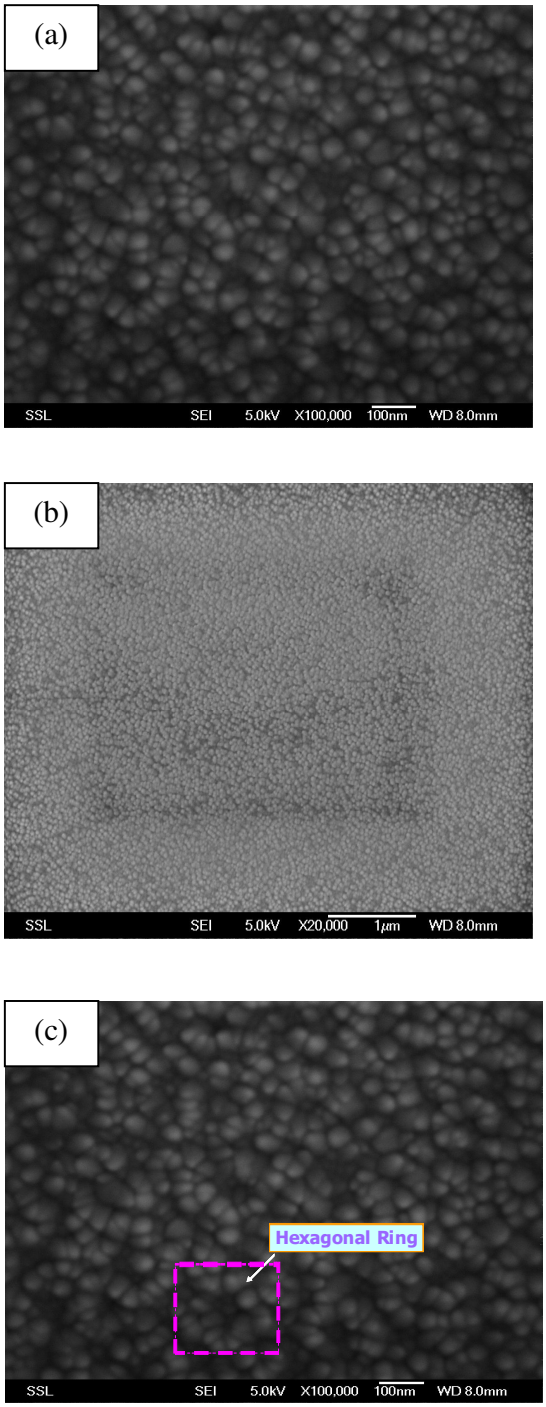

Fig. 4.6. SEM images of (a) Cu-doped ZnO film deposited on Si (100) at high magnification, (b) Cu-doped ZnO film at low magnification and (c) hexagonal ring structure drawn on (a).

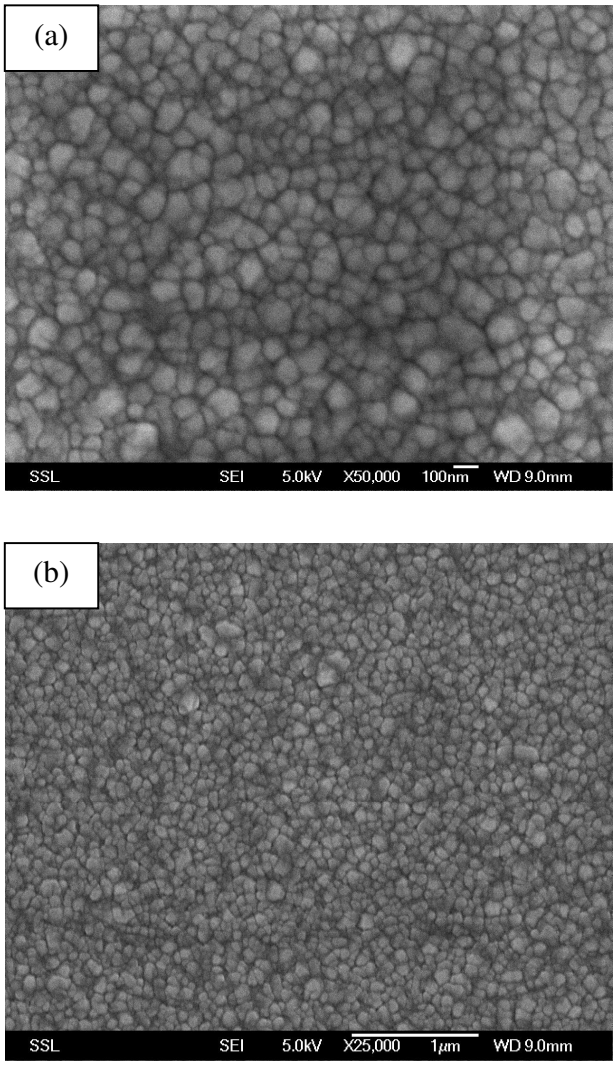

Fig. 4.7. SEM images of (a) Ti-doped ZnO film deposited on Si (100) at high magnification, (b) Ti-doped ZnO film at low magnification.

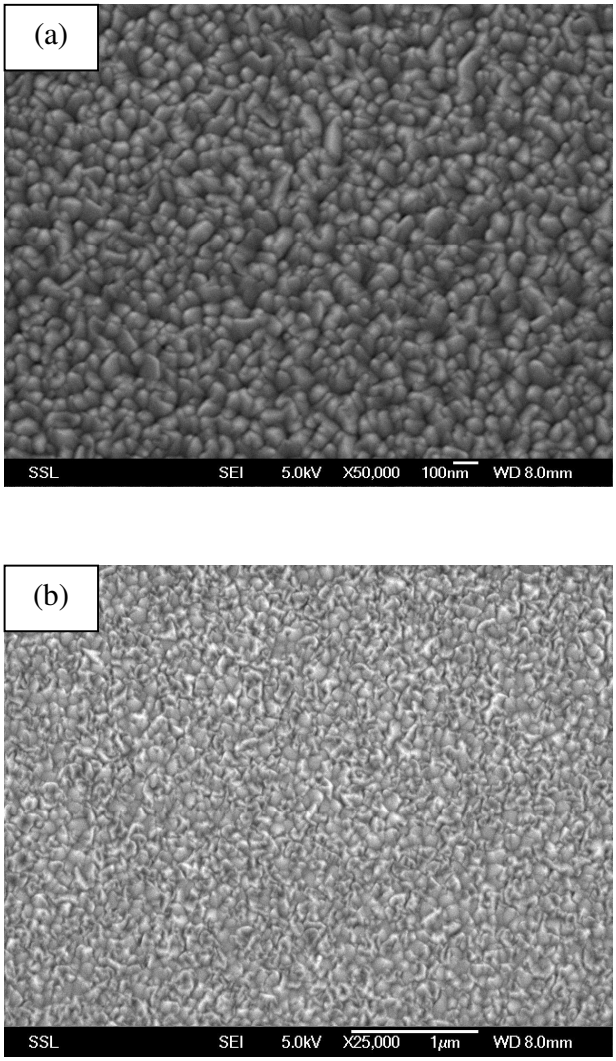

Fig. 4.8. SEM images of (a) Mn-doped ZnO film deposited on Si (100) at high magnification, (b) Mn-doped ZnO film at low magnification.

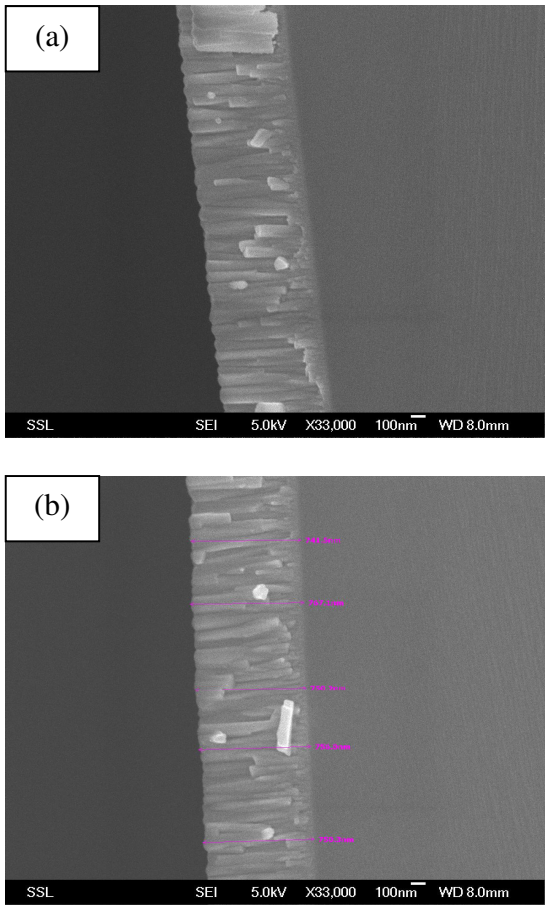

Fig. 4.9. Cross-sectional view of (a) Cu-doped ZnO thin film deposited on Si (100), (b) thickness of the same film indicated on the image.

4.4 X-ray Diffraction (XRD)

The as-grown samples with various compositions of Zn, Co, Cu, Ti and Mn were subjected to XRD studies for gross structural characterization. ZnO thin films deposited on Si (100) substrates and glass slides show polycrystalline structure, indicating that the respective ZnO grains are rotated along the c-axis direction due to large differences between ZnO and Si/glass in terms of physical properties such as thermal expansion coefficient and lattice mismatch.

4.4.1 Co-doped ZnO films

ZnO (002) and ZnO (201) peaks are observed in the XRD spectra of the undoped ZnO and Co-doped ZnO films deposited on Si (100) substrates as shown in Fig. 4.10. ZnO (101) peak is only observed for $Zn_{0.809}Co_{0.191}O$ film, which is the thickest among the Co-doped films. This is an indication of poorer-texture film.[3] This indicates a non-preferential-orientation wurtzite structure. No particular trend is observed for the films grown under the same gas ambient. No metal or metal oxide related peak was detected within the sensitivity of XRD. However, the peak position of ZnO: Co is shifted by $0.2^{o} – 0.4^{o}$ towards the higher angles as compared to undoped ZnO. The peak shift suggests a decrease in lattice parameter c of the Co-doped ZnO by Bragg's law. The decrease in c is consistent with the substitution of Zn^{2+} ion (radius = 0.600 Å)[4,5] by the smaller Co^{2+} ion (radius = 0.058 Å)[5,6].

The XRD spectrum of the same Co-doped ZnO film deposited on Si (100) with different geometrical orientations might give different peak intensities and even an extra ZnO peak (103) as shown in Fig. 4.11; this implies that these films exhibit anisotropic behavior. Fig. 4.12 displays the XRD spectrum of Co-doped ZnO films deposited on glass slides with Co concentrations of less than 2.5%. XAFS results presented in section 5.2.1 have proven the incorporation of Co ions into the ZnO lattice at these Co concentrations. ZnO (002) peak and a very weak ZnO (004) peak are observed and ZnO (002) peak being the dominant peak suggests that the single phase Co-doped ZnO film deposited on glass is strongly c-axis orientated. This also implies that the Co-doped ZnO films grown on glass slides might have slightly different crystal phases as compared to those grown on Si (100) substrates.

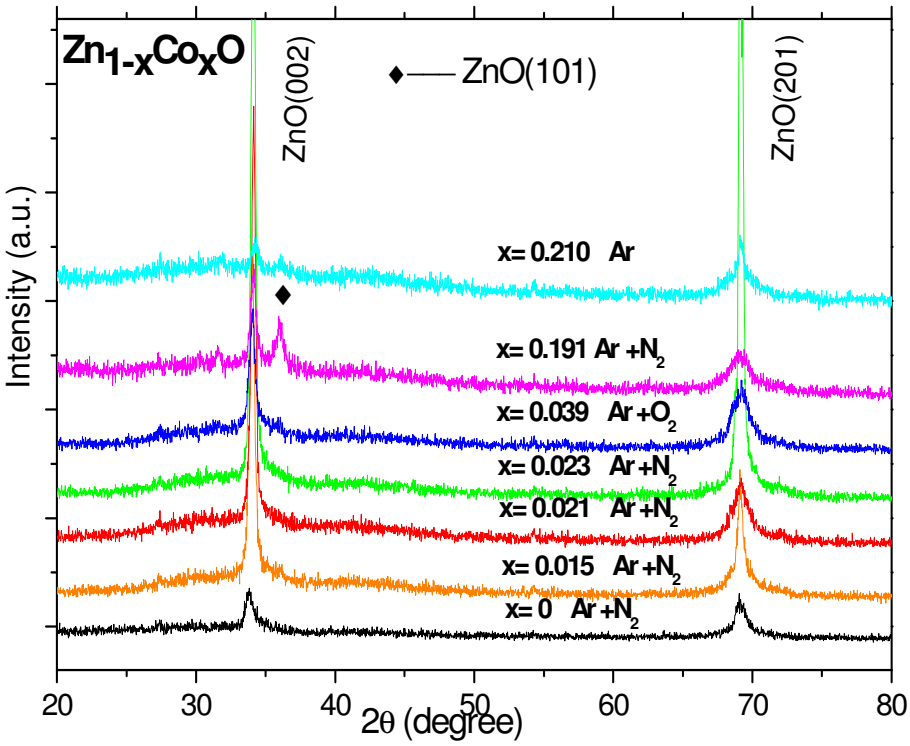

Fig. 4.10. XRD patterns of the ZnO and Co-doped ZnO films deposited on Si (100). The Co concentrations **x** were determined by XRF.

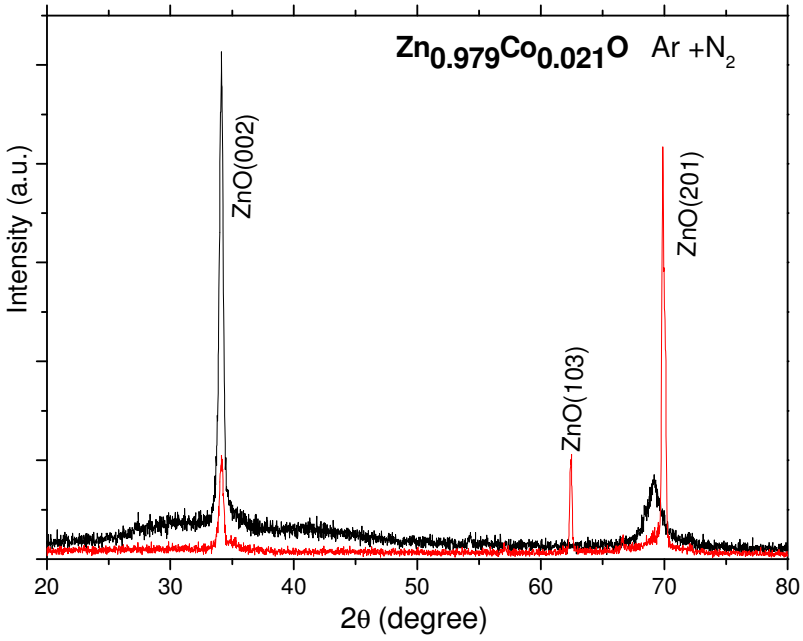

Fig. 4.11. Repeated XRD measurements of the same Co-doped ZnO film deposited on Si (100).

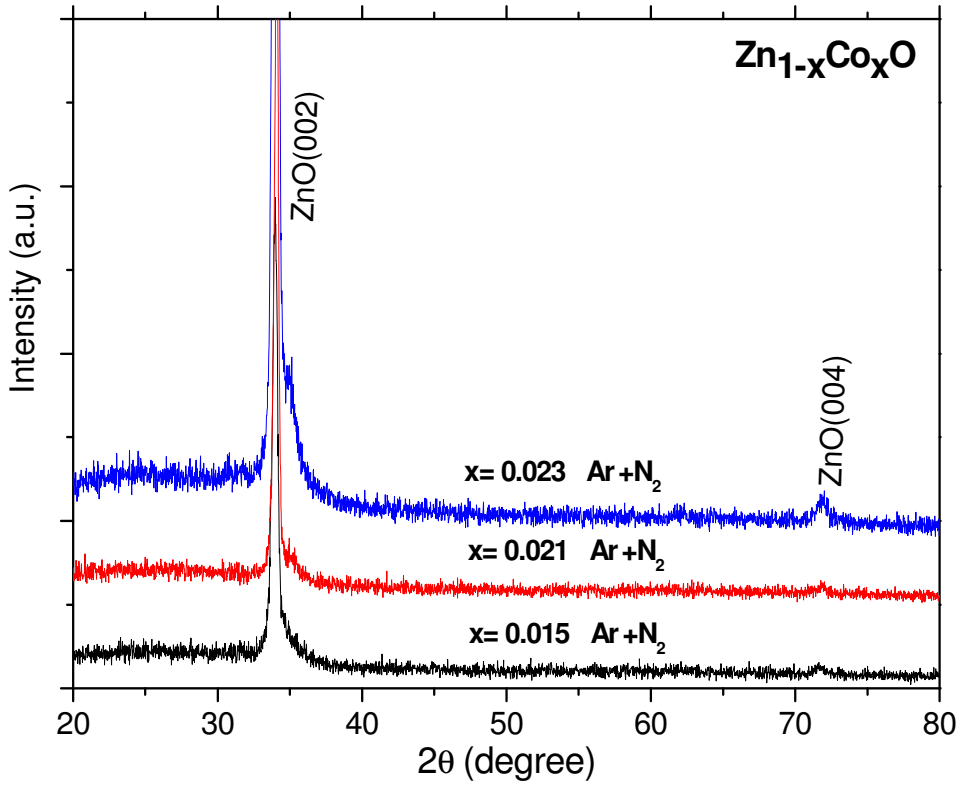

Fig. 4.12. XRD patterns of Co-doped ZnO films deposited on glass.

4.4.2 Cu-doped ZnO films

The XRD spectra for the undoped ZnO and Cu-doped ZnO films deposited on Si (100) substrates are displayed in Fig. 4.13. Both ZnO(002) and ZnO(201) peaks are observed for the undoped ZnO and Cu-doped ZnO films with Cu concentrations below 6% deposited on Si (100) substrates. This indicates a non-preferential-orientation wurtzite structure. No particular trend is observed for the films grown under the same gas ambient. For high Cu concentrations, the ZnO (002) peak is absent ($Zn_{0.812}Cu_{0.188}O$ and $Zn_{0.754}Cu_{0.246}O$), but ZnO (201) appears appears for both films. This implies that these films are not c-axis orientated. The ZnO (103) peak shows up when the Cu concentration exceeds 2%. No metal or metal oxide related peak can be detected

within the sensitivity of XRD below Cu concentrations of 19%. The Cu_2O (220) phase is readily observed in $Zn_{0.754}Cu_{0.246}O$.

The peak position of ZnO: Cu is shifted by 0.3^o – 0.5^o towards higher angles as compared to undoped ZnO. The peak shift implies a decrease in lattice parameter c of the Cu-doped ZnO by Bragg's law. Since the radius of the Zn^{2+} ion is approximately the same as that of the Cu^+ ion (radius = 0.600 Å)[7], the decrease in lattice parameter c cannot be solely explained by ionic radii difference. The reason might be due to the strain caused by non-uniform substitution of Cu ions into the Zn site[5,8] and complex defect formation[7].

XRD spectrum of the same particular Cu-doped ZnO film deposited on Si (100) substrate with different geometrical orientation might give different peak intensities as depicted in Fig. 4.14; this implies that these films exhibit anisotropy behavior. Fig. 4.15 displays the XRD spectrum for Cu-doped ZnO films deposited on glass slides with Cu concentrations of less than 2.5%. The ZnO (002) and ZnO (004) peaks are identified, and dominant ZnO (002) peak implies that the single phase Cu-doped ZnO film deposited on glass is strongly c-axis orientated. We have come to the same conclusion as the Co-doped ZnO films that the Cu-doped ZnO films grown on glass slides might have slightly different crystal phases as compared to those grown on Si (100) substrates.

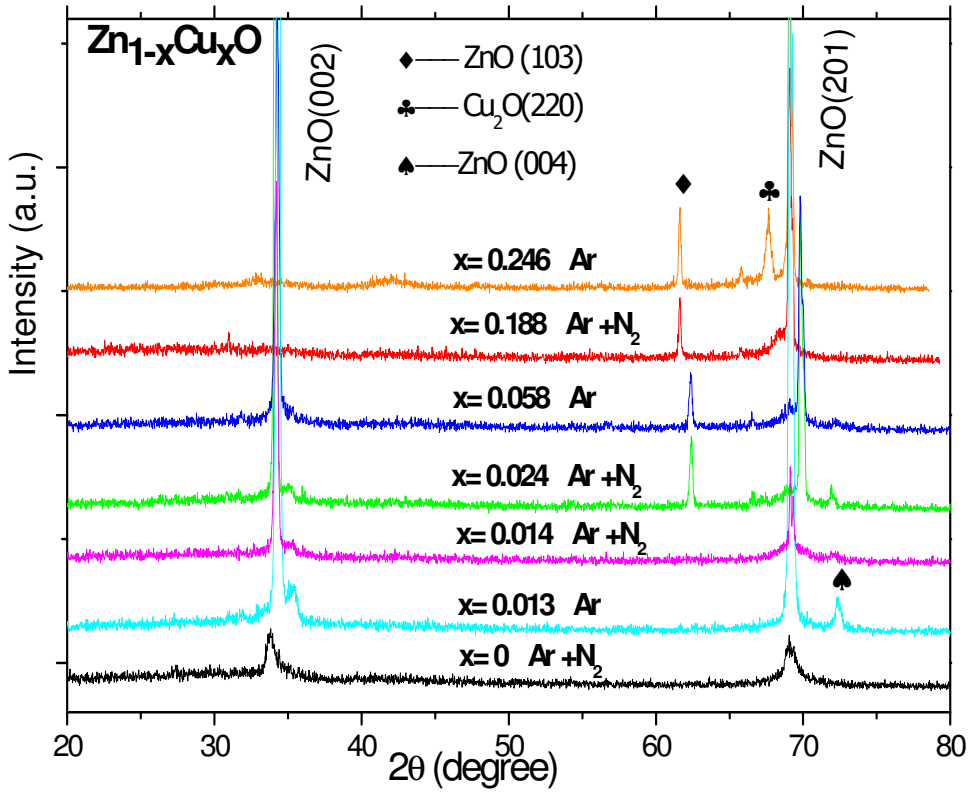

Fig. 4.13. XRD patterns of the ZnO and Cu-doped ZnO films deposited on Si (100). The Cu concentrations **x** were determined by XRF.

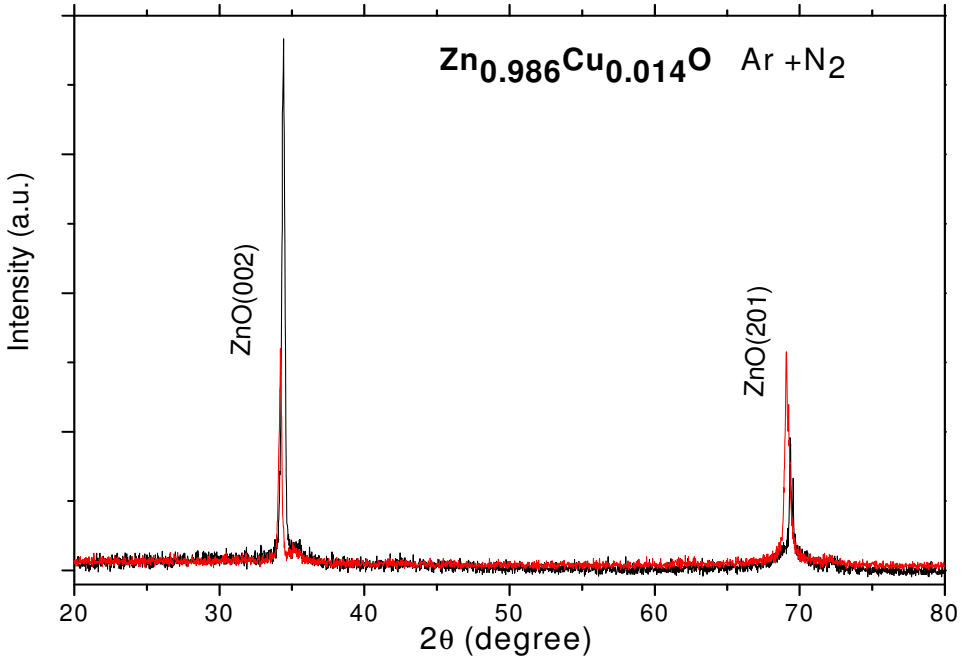

Fig. 4.14. Repeated XRD measurements of the same Cu-doped ZnO film deposited on Si (100).

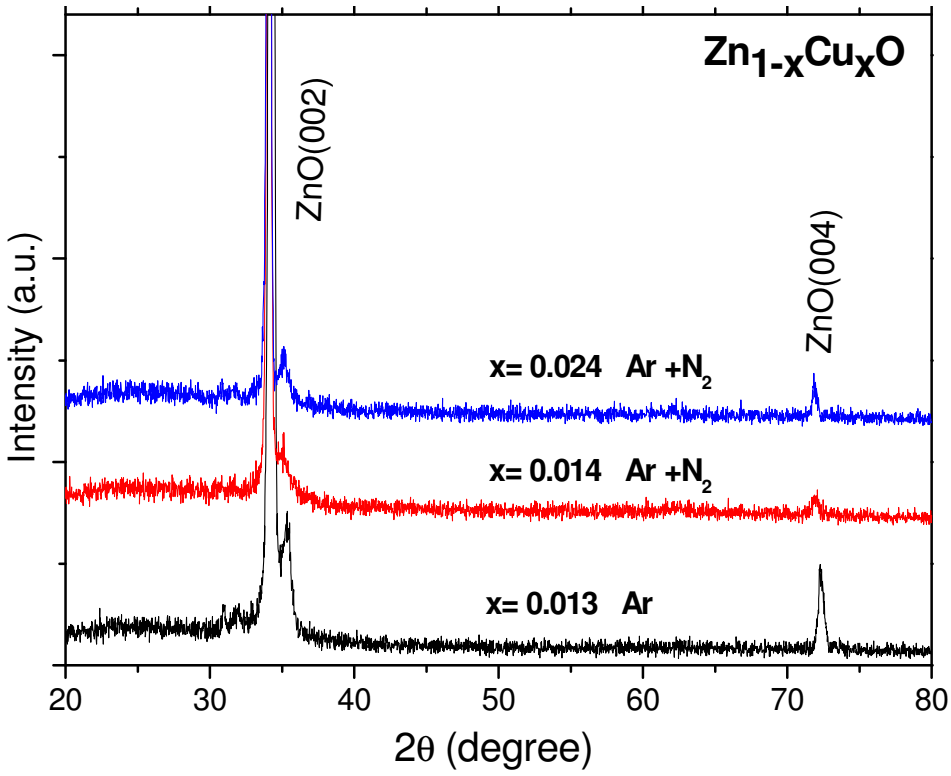

Fig. 4.15. XRD patterns of Cu-doped ZnO films deposited on glass.

4.4.3 Ti-doped ZnO films

The ZnO (002) and (201) peaks from the undoped ZnO and Ti-doped ZnO films deposited on Si (100) substrates could be identified in Fig. 4.16. This indicates a non-preferential-orientation wurtzite structure. No particular trend is observed for the films grown under the same gas ambient. No metal or metal oxide related peak can be detected within the sensitivity of XRD. However, the peak position of ZnO: Ti is shifted by 0.1^{o} – 0.2^{o} towards higher angles as compared to undoped ZnO. The peak shift implies a decrease in lattice parameter c of the Ti-doped ZnO by Bragg's law. The decrease in c is not consistent with the substitution of Zn^{2+} ion (radius = 0.600 Å) by the bigger Ti^{3+} ion (radius = 0.670 Å). However, the decrease in c is in agreement with the theoretical calculations in reference [9] which mainly attributes this

phenomenon to the reduced bond length of the Ti-O bond after Ti ion substituted Zn ion in the ZnO wurtzite structure. As mentioned above, the reason might be due to the strain caused by non-uniform substitution of Ti ions into the Zn site[5,8] and complex defect formation[7].

The XRD spectrum of the same particular Ti-doped ZnO film deposited on Si (100) with different geometrical orientations might give different relative peak intensities and even an extra ZnO peak (103) as shown in Fig. 4.17; this implies that these films exhibit anisotropic behavior. The ZnO (002) peak is present in Fig. 4.18 (the XRD spectrum of Ti-doped ZnO films deposited on glass slides). This implies that the single phase Ti-doped ZnO film deposited on glass is strongly c-axis orientated. We have come to the same conclusion as the above. The Ti-doped ZnO films grown on glass slides might have slightly different crystal phases as compared to those grown on Si (100) substrates.

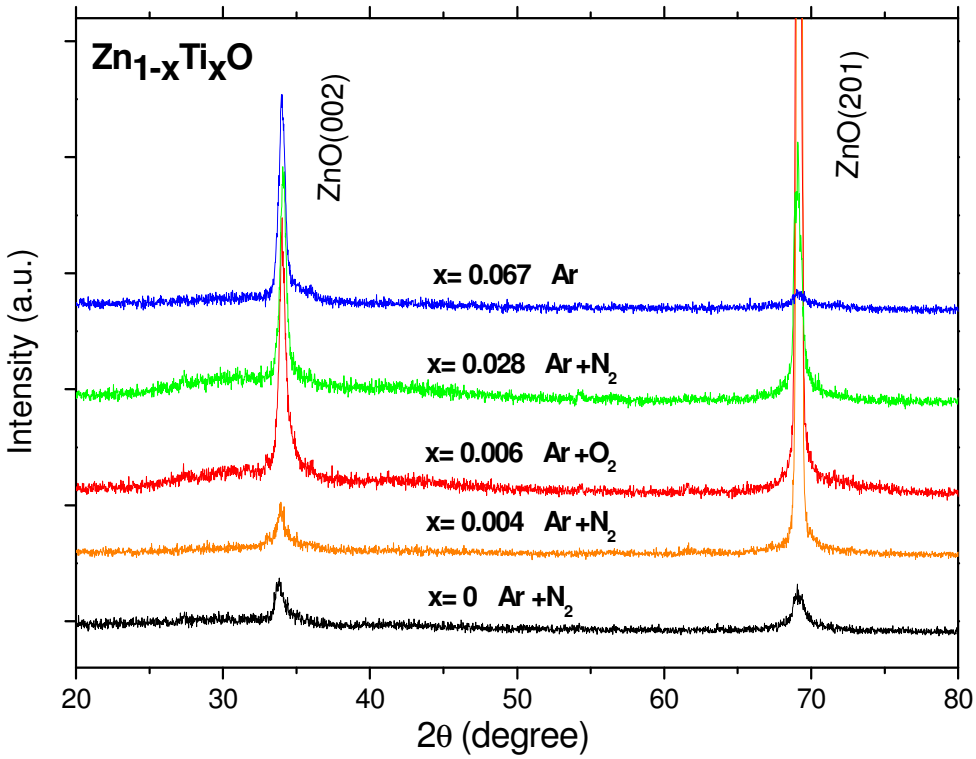

Fig. 4.16. XRD patterns of the ZnO and Ti-doped ZnO films deposited on Si (100). The Ti concentrations **x** were determined by XRF.

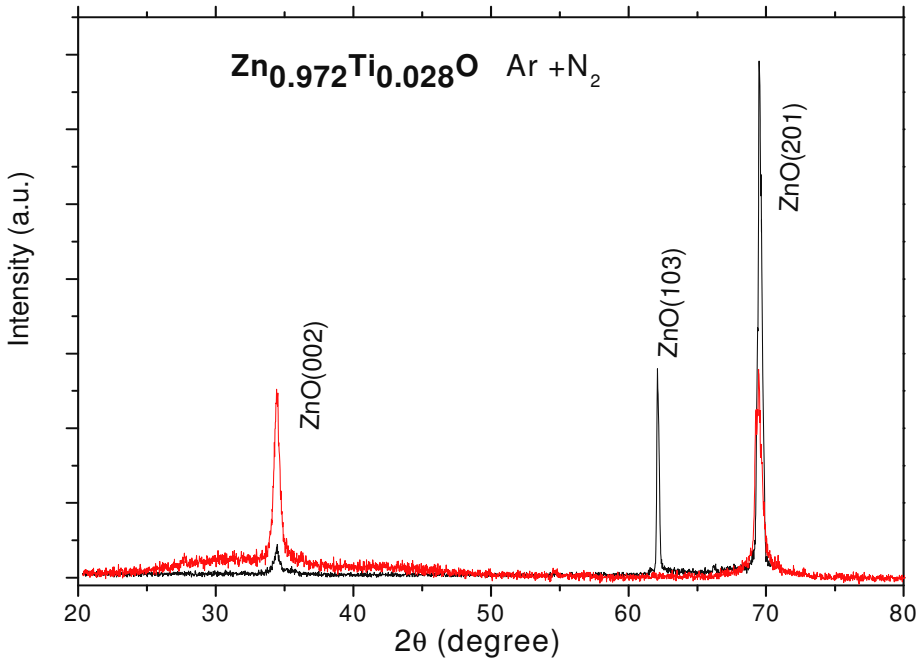

Fig. 4.17. Repeated XRD measurements of the same Ti-doped ZnO film deposited on Si (100).

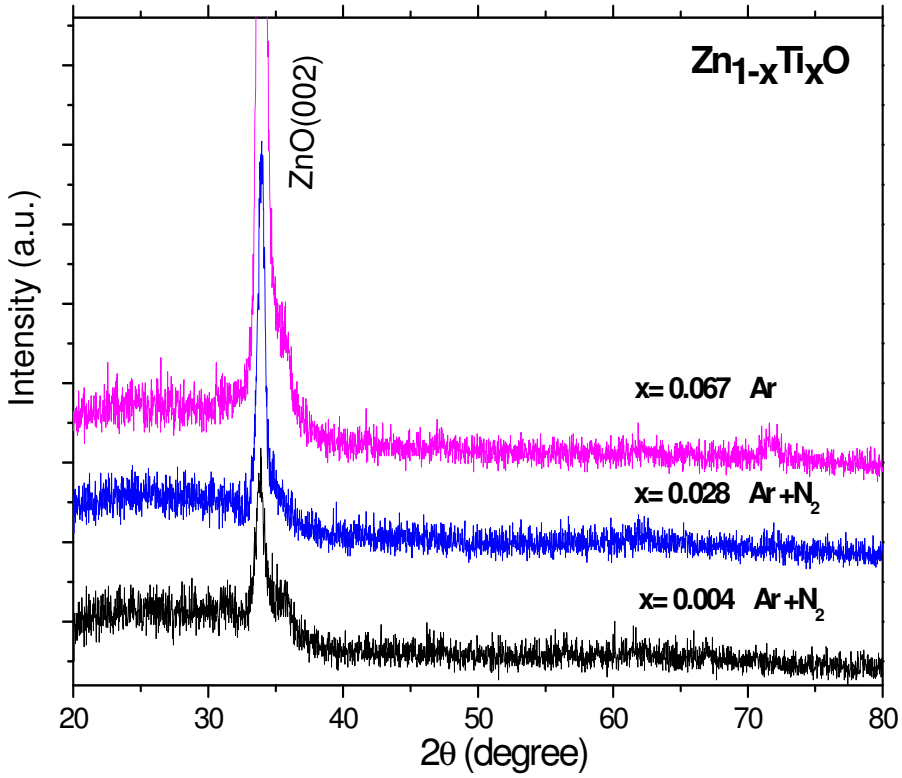

Fig. 4.18. XRD patterns of Ti-doped ZnO films deposited on glass.

4.4.4 Mn-doped ZnO films

Fig. 4.19 illustrates the XRD spectrum for the undoped ZnO and Mn-doped ZnO films deposited on Si (100) substrates. The ZnO (002) and ZnO (201) peaks are recognized in Fig. 4.19 for all samples. This indicates a non-preferential-orientation wurtzite structure. No particular trend is observed for the films grown under the same gas ambient. However, $Zn_2Mn_3O_8$ (215) peak is observed for the $Zn_{0.978}Mn_{0.022}O$ sample. Little information on the properties of the complex compound $Zn_2Mn_3O_8$ has been found. The XAFS results presented in section 5.2.4 has confirmed the precipitation of Mn. The reason for precipitation might be due to the ambient atmosphere in which the film is fabricated and might not be related to the Mn concentration; this shall be discussed in the later chapter.

The peak position of ZnO: Mn is shifted by 0.2^o – 0.4^o towards higher angles as compared to undoped ZnO. The peak shift suggests a decrease in lattice parameter c of the Mn-doped ZnO. The decrease in c is not consistent with the substitution of the Zn^{2+} ion (radius = 0.600 Å) by the bigger Mn^{2+} ion (radius = 0.660 Å)[6,10]. The reason might be due to the non-uniform substitution of Mn ions into the Zn site[5,8] and complex defect formation[7] as suggested previously.

Fig. 4.20 shows the XRD spectrum of the same particular Mn-doped ZnO film deposited on Si (100) substrate. It reveals that the same sample orientated at different positions might give different peak intensities; this implies that these films exhibit anisotropy behavior. The Mn-doped ZnO films deposited on glass slides exhibit ZnO (002) peak and an extremely weak ZnO (004) peak as shown in Fig. 4.21. The dominant ZnO (002) peak indicates that the film has a strongly c-axis orientated wurtzite structure. Hence, ZnO films grown on glass slides might have slightly different crystal phases as compared to those grown on Si (100) substrates.

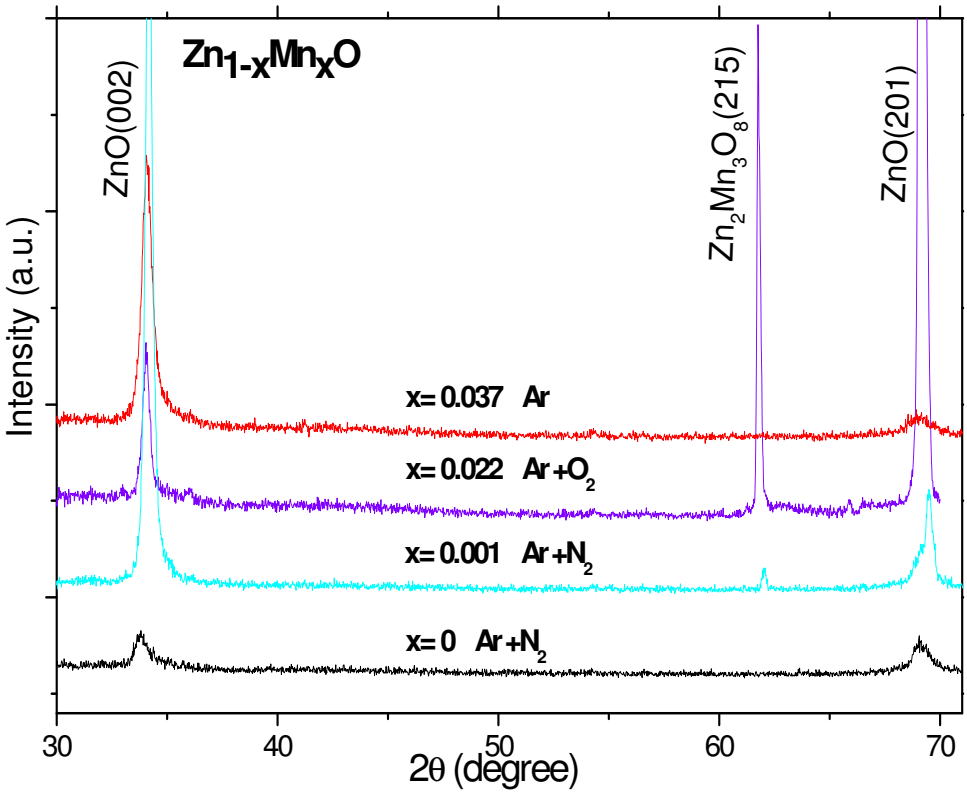

Fig. 4.19. XRD patterns of the ZnO and Mn-doped ZnO films deposited on Si (100). The Mn concentrations **x** were determined by XRF.

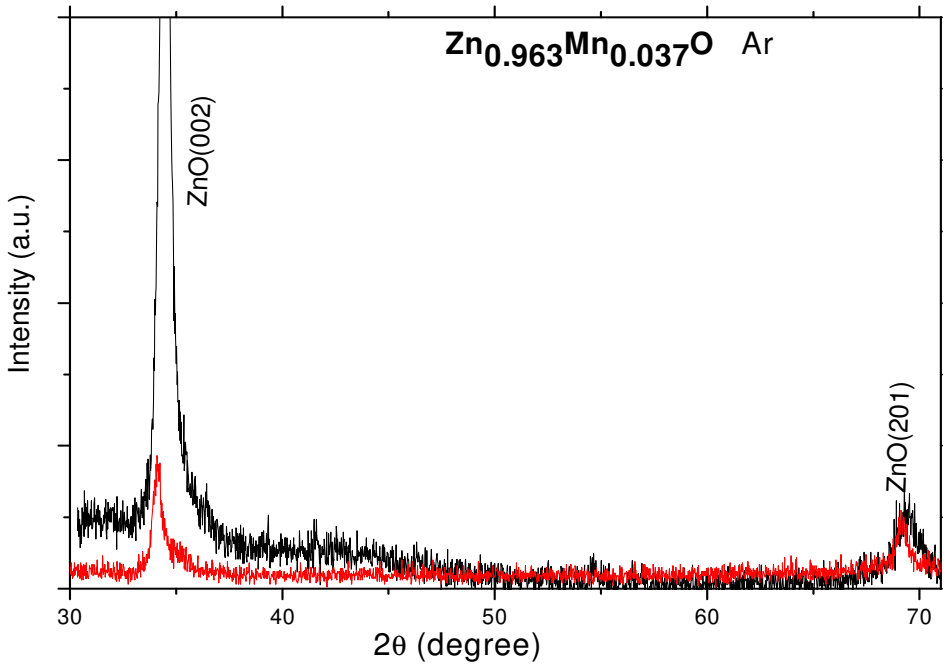

Fig. 4.20. Repeated XRD measurements of the same Mn-doped ZnO film deposited on Si (100).

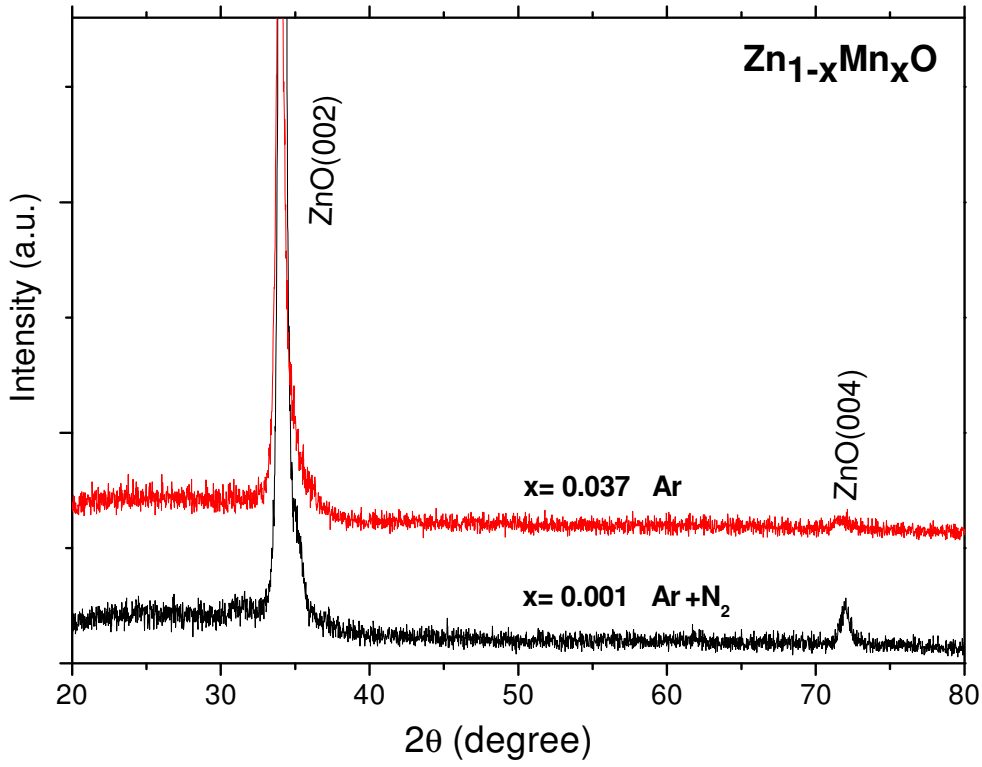

Fig. 4.21. XRD patterns of the Mn-doped ZnO films deposited on glass.

4.4.5 Summary of XRD Results

All TM (Co, Cu, Ti and Mn)-doped ZnO films deposited on Si (100) exhibit anisotropic behavior. No particular trend is observed for the films grown under the same gas ambient for all TM-doped samples. ZnO (002) and ZnO (201) peaks are observed in all the XRD spectra of the undoped ZnO and Co, Ti and Mn-doped ZnO films deposited on Si (100) substrates. ZnO (101) peak is only observed for the thickest Co-doped film. This indicates non-preferential-orientation wurtzite structures. On the other hand, both ZnO(002) and ZnO(201) peaks are only observed for the Cu-doped ZnO films deposited on Si (100) substrates with Cu concentrations below 6%. For high Cu concentrations, the ZnO (002) peak is absent. This implies that these

films are not c-axis orientated. The ZnO (103) peak shows up when the Cu concentration exceeds 2%.

All the peak positions of ZnO: TM are shifted slightly towards the higher angles as compared to undoped ZnO. The peak shifts suggest a decrease in c of the all TM-doped ZnO films by Bragg's law. The decrease in c is consistent with the substitution of Zn^{2+} ion by the smaller Co^{2+} ion. However, it is not consistent with the cases of Cu, Ti and Mn. Hence, ionic radii difference between Zn^{2+} and TM ions cannot fully account for the decrease in lattice parameter c. The possible reason might be due to the strain caused by non-uniform substitution of Cu, Ti and Mn ions into the Zn site and complex defect formation.

All TM-doped ZnO films deposited on glass slides exhibit ZnO (002) peak. The dominant ZnO (002) peak indicates that these films have a strongly c-axis orientated wurtzite structure. Thus, ZnO films grown on glass slides might have slightly different crystal phases as compared to those grown on Si (100) substrates.

4.5 Secondary ion mass spectroscopy (SIMS)

SIMS was performed to investigate whether the distribution of TM ions is uniform throughout the bulk of TM-doped ZnO films annealed at high temperature since there is a likelihood of segregation of transition metal oxides near the surfaces.

First, samples with no precipitation as confirmed by EXAFS results in chapter 5 were chosen for annealing. The samples were first annealed at 800^{o}C in air in a furnace. The rate of temperature increment was 15 ^{o}C per minute, and subsequently the temperature was kept constant at 800^{o}C for an hour. The temperature was then decreased at 15 ^{o}C per minute. The annealed samples were then removed from the furnace after cooling to room temperature.

SIMS measurements were performed on a Cameca IMS-6F SIMS; primary beams of O^{2+} at 7.5 kev impact energy were used for the depth profiling. The angle of bombardment of O^{2+} with respect to the sample surface is about 50^{o}. The SIMS spectra for $Zn_{0.977}Co_{0.023}O$ annealed at $800^{o}C$ showed uniform dopant distribution with respect to the distribution of Zn^{2+} ions as shown in Figs. 4.22. The as prepared Co-doped ZnO sample was not analyzed by SIMS since the annealed sample already showed uniform dopant distribution.

Fig. 4.23 displays the SIMS spectrum of the as-prepared $Zn_{0.986}Cu_{0.014}O$ sample showing a slightly higher concentration of Cu ions in the bulk of ZnO relative to the surface. However, after annealing this sample at $800^{o}C$, surface precipitation of Cu or Cu oxides was observed in Fig. 4.24. This might lead to ferromagnetism in Cu-doped ZnO samples calcinated at high temperatures.

Fig. 4.25 displays the SIMS spectrum of the as-prepared $Zn_{0.978}Mn_{0.022}O$ sample illustrating a two-layer growth of the film. The bottom bulk layer was richer in Mn than the top layer. The bottom bulk layer was richer in terms of Mn ions than the top layer. This might be due to a sudden change of sputtering conditions like a decrease in gas flow or a decrease of deposition power etc and this is not observed in other Mn-doped samples. After annealing this sample at $800^{o}C$, the concentration of Mn at shallower depth increased as shown in Fig. 4.26. This implies that the Mn ions gained energy and diffused towards the surface in the form of Mn oxides as thermal vibrations increased. This result has been confirmed in XAFS Section 5.2.4. The precipitated Mn oxides might lead to ferromagnetism in Mn-doped ZnO samples annealed at high temperatures.

Out of the three annealed TM (Co, Cu and Mn)-doped ZnO samples, only the Co-doped ZnO sample showed uniform dopant distribution relative to the Zn^{2+} distribution. The as-prepared $Zn_{0.986}Cu_{0.014}O$ sample possessed a slightly higher concentration of Cu ions in the bulk of ZnO

with respect to the surface whereby after annealing, surface precipitation of Cu or Cu oxides was observed. The $Zn_{0.978}Mn_{0.022}O$ film consisted of two-layers, the bottom layer being Mn richer than the top layer. After annealing this sample, the concentration of Mn at shallower depth increased.

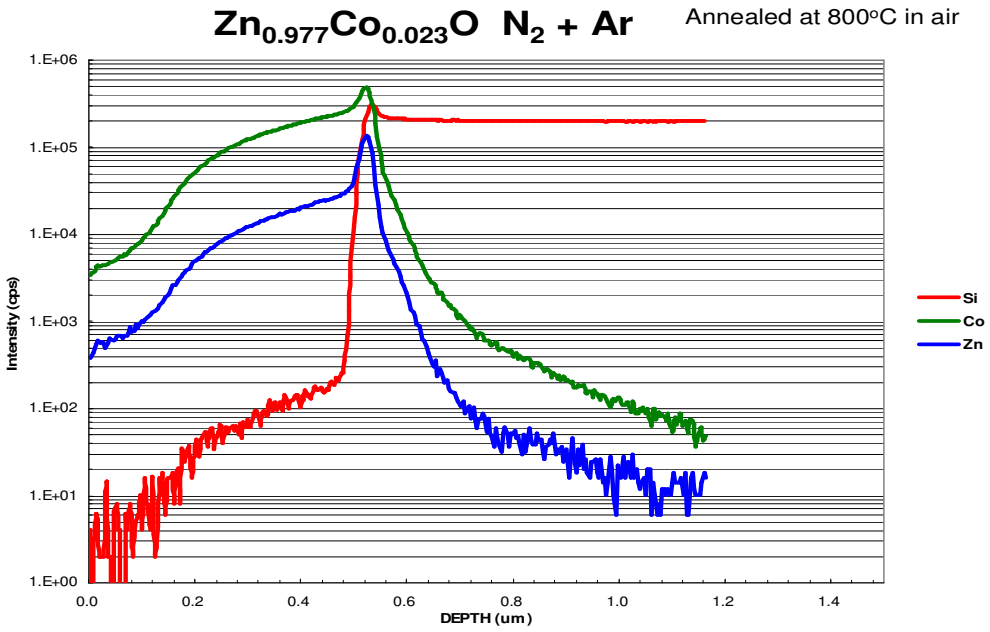

Fig. 4.22. SIMS spectrum of $Zn_{0.977}Co_{0.023}O$ sample annealed at 800°C in air.

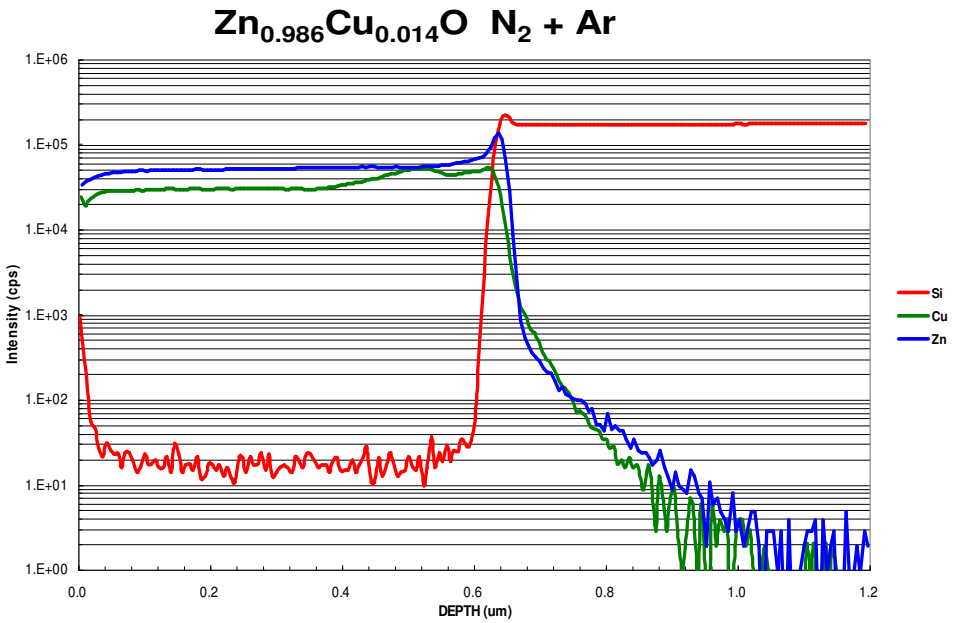

Fig. 4.23. SIMS spectrum of $Zn_{0.986}Cu_{0.014}O$ sample.

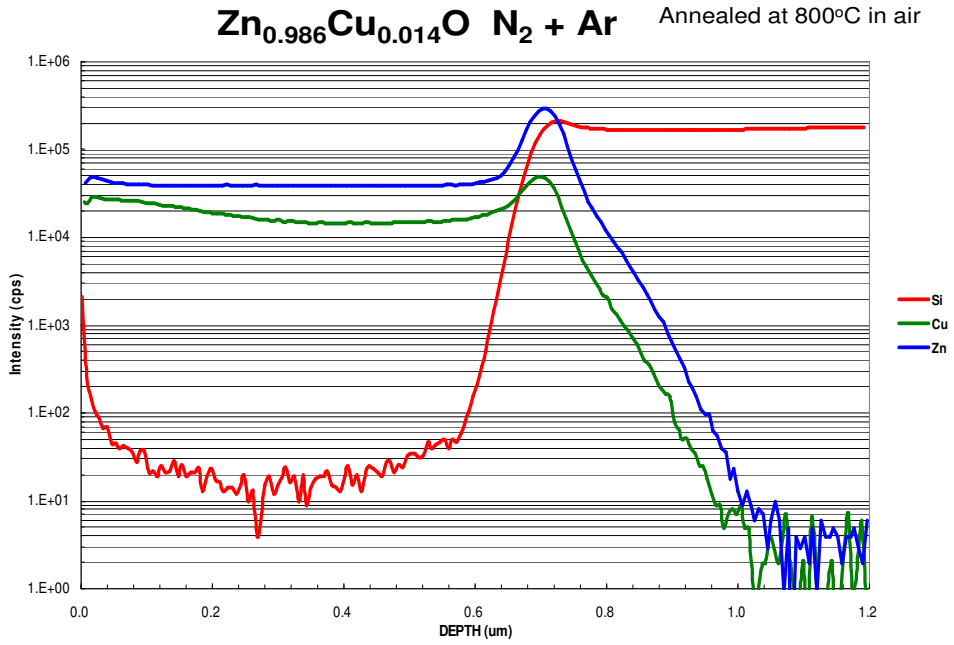

Fig. 4.24. SIMS spectrum of $Zn_{0.986}Cu_{0.014}O$ sample annealed at 800°C in air.

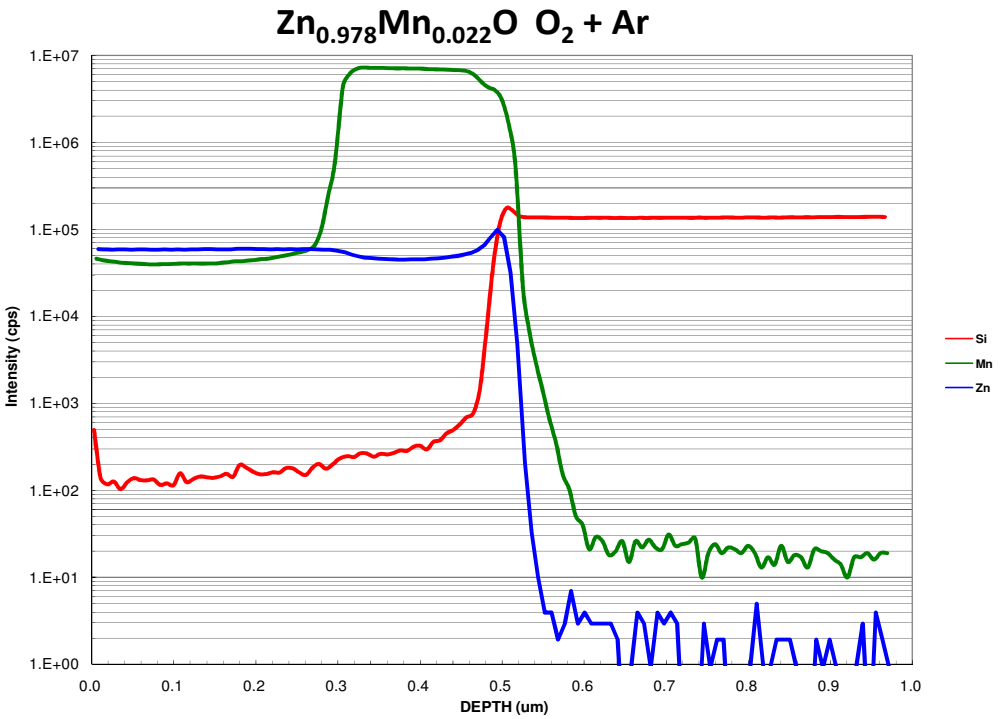

Fig. 4.25. SIMS spectrum of $Zn_{0.978}Mn_{0.022}O$ sample.

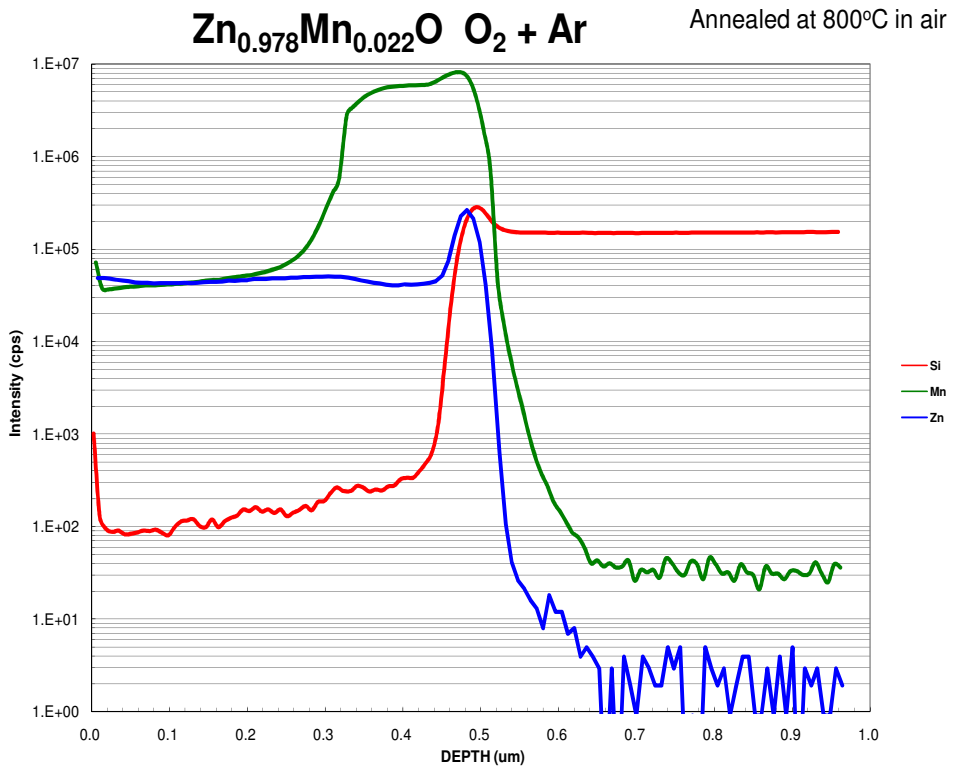

Fig. 4.26. SIMS spectrum of $Zn_{0.978}Mn_{0.022}O$ sample annealed at 800°C in air.

4.6 Conclusions

The thickness of all films was found to be a few thousands angstroms. The films are polycrystalline in nature. The Co, Cu and Ti-doped ZnO films have relatively small and slightly elongated spherical grain structure. The Mn-doped ZnO films, on the other hand, have a mixture of small, spherical and blade-like grain structures. The images at high magnification also display ring hexagonal structures of the ZnO compound.

All TM-doped ZnO films deposited on glass slides exhibit ZnO (002) peak in XRD spectrum. The dominant ZnO (002) peak indicates that these films have a strongly c-axis orientated wurtzite structure. Thus, ZnO films grown on glass slides might have slightly different crystal phases as compared to those grown on Si (100) substrates.

All TM (Co, Cu, Ti and Mn)-doped ZnO films deposited on Si (100) exhibit anisotropy behavior. These films have non-preferential-orientation wurtzite structures. There is also a decrease in c of the all TM-doped ZnO films. The decrease in c is consistent with the substitution of Zn^{2+} ion by the smaller Co^{2+} ion. However, it is not consistent with the cases of Cu, Ti and Mn. Hence, ionic radii difference between Zn^{2+} and TM ions cannot fully account for the decrease in lattice parameter c. The possible reasons might be due to the strain caused by non-uniform substitution of Cu, Ti and Mn ions into the Zn site and complex defect formation.

Secondary ion mass spectrometry (SIMS) has shown that out of the three annealed TM (Co, Cu and Mn)-doped ZnO samples, only $Zn_{0.977}Co_{0.023}O$ showed uniform dopant distribution relative to the Zn^{2+} distribution. The as prepared $Zn_{0.986}Cu_{0.014}O$ sample possessed a slightly higher concentration of Cu ions in the bulk of ZnO with respect to the surface whereby after annealing, surface precipitation of Cu or Cu oxides was observed. $Zn_{0.978}Mn_{0.022}O$ film consisted of two-layers,

the bottom layer being Mn richer than the top layer. After annealing this sample, the concentration of Mn at shallower depth increased.

References

1. A. Yeo, P. Yang, A.G. Fane, T. White and H.O. Moser, Journal of Membrane Science **250**,189 (2005).
2. Jaffe, J. E, Pandey, Ravindra, Kunz, A. B, Physical Review B, **43**, 14030 (1991).
3. Klaus Ellmer, J. Phy. D, **33**, R17 (2000).
4. P. Bhattacharya, R. R. Das, R. S. Katiyar, Thin Solid Films, **447,** 564 (2004).
5. T.S. Herng, S.P. Lau, S.F. Yu, H.Y. Yang, X.H. Ji, J. Appl. Phys, **99**, 086101 (2006).
6. S. Kolesnik, B. Dabrowski, J. Mais, J.Appl. Phys, **95**, 2582 (2004).
7. Z.Banu Bashi, A.Yavuz Oral, Optical materials, **29**, 672 (2007).
8. Jiji Antony, Sweta Pendyala, David E. McCready, Mark H. Engelhard, IEEE Transactions On Magnetics, **42**, 2697 (2006).
9. Zhi-hua Xiong, Feng-yi Jiang, J. Phy. And Chem. of Solids, **68**, 1500 (2007).
10. C. Liu, F. Yun and H. Morkoc, J. Mater. Sci. **16**, 555 (2005).

Chapter 5

XAFS investigations of 3d metal doped ZnO thin films

In this chapter, the XANES and EXAFS experimental procedures will be covered (section 5.1), followed by the results and discussions for TM (Co, Cu, Ti and Mn) -doped ZnO films (Section 5.2).

5.1 Experimental procedure

The Co, Cu and Mn–doped ZnO films were measured at X-ray Development and Demonstration beamline[1] (XDD) beamline at the Singapore Synchrotron Light Source (SSLS) which has an available energy range of 2.4keV -10 keV, whereas the Ti-doped ZnO films, due to the low concentration and low binding energy for Ti, were performed at SPring-8 in Hyogo, Japan.[2]

XAFS spectra of film samples deposited on glass were collected in the fluorescence mode at the XDD beamline employing a home-made Lytle-type detector filled with argon ambient. The samples were mounted in grazing incidence geometry at an incident angle of 4° with the sample plane parallel to the electric field vector of the incident beam. Thin glass slides are chosen for deposition as substrates since Si single crystal substrates exhibit diffraction peaks in the EXAFS spectrum. These diffraction peaks overlap with the measured absorption spectrum, making it difficult to perform EXAFS analysis. As glass is amorphous, there will be no diffraction peak in the EXAFS spectrum.

The incident intensity of x-ray photons were recorded by an air filled ionization chamber. The reference samples of metal foils and metal

oxides were measured in transmission mode where a second ionization chamber was employed. These were discussed in section 2.5.1. Standards of metal oxides were ground into fine powders and dispersed on Scotch tapes. The tapes were folded into a number of layers and tested for optimal thickness for transmission. The energy was calibrated to the K-edge absorption of metal-foils. XAFS spectra were collected in the photon energy range from roughly 100eV prior to the absorption edge to several hundred eV above.

Experiments at SPring-8 were performed at room temperature at the BL01B1 beamline[3] which has an available energy range of 3.8 keV – 113 keV. BL01B1 is a bending magnet beam line equipped with 2 mirrors and a fixed-exit double-crystal monochromator using Si(311) crystals. X-ray fluorescence from the samples was detected by a 19-element Ge solid-state detector.[4]

5.2 Results and Discussion

5.2.1 Co-doped ZnO films

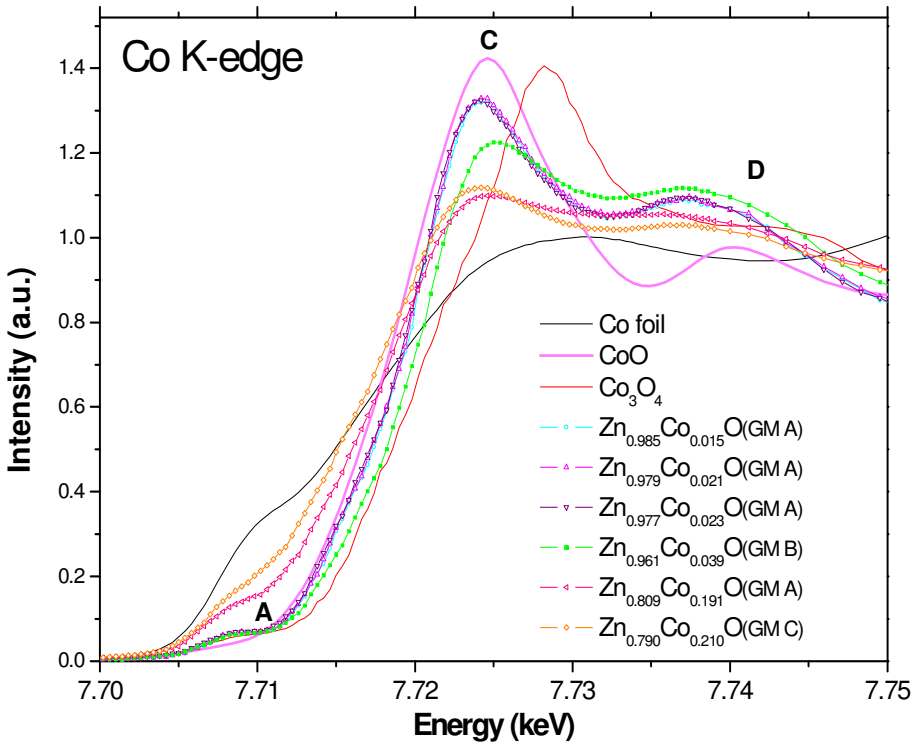

Fig. 5.1. Normalized Co K-edge XANES spectra of Co-doped ZnO films deposited on glass, Co foil, CoO and Co_3O_4. GM A, GM B and GM C stand for 85%Ar + 15%N_2, 80%Ar + 20%O_2 and Ar gas mixture, respectively.

The XANES features are mostly associated with the configuration of the nearest neighbors. Three main features are identified in the XANES spectrum in Fig. 5.1 are: the small pre-edge peak A, the dominant main peak C and the shoulder D at the post-edge region. The interpretations of K-edge XANES features for 3d transition-metal oxides are well established. [5-7] In the tetrahedral configuration of oxygen nearest neighbors, the 3d, 4s and 4p orbitals of TM are hybridized and mixed with the O 2p orbitals to form hybridized

molecular orbitals. The features A and C in XANES can be attributed to the unfilled anti-bonding states of these molecular orbitals.[5,8,9] Generally, peak A is interpreted as a quadrupolar electronic transition from 1s to the unoccupied 3d final states hybridized with 4p character of the absorber; its intensity is enhanced by the local atomic configuration that lacks centrosymmetry.[5,10] Even though it is not allowed by the electronic dipolar selection rule, $\Delta l = \pm 1$, the pre-edge peak is discernible due to the mixing of 4p and 3d states. Therefore, this feature gains significant spectral weight for the case of non-centrosymmetric tetrahedral geometry of an absorbing atom through the mixing of d–p orbitals.[10]

Peak C arises from the dominant dipolar transition from 1s to the 4p-related final states; the intensity drops significantly in samples with Co oxides and Co metal precipitation. This peak is higher for octahedral sites (CoO) than tetrahedral sites. The shoulder D has a solid state character which is attributed to the single scattering contribution of absorbers with the third coordination shell of O neighbors[8,9] and it is known to be associated with orbital mixing of the more delocalized Co 4p with higher shell O atoms.

Fig. 5.1 compares the normalized Co K-edge XANES spectra of Co-doped ZnO films deposited on glass with those of the reference materials. A comparison with CoO in terms of chemical shift indicates a valence state 2+ for Co in the $Zn_{0.985}Co_{0.015}O$, $Zn_{0.979}Co_{0.021}O$ and $Zn_{0.977}Co_{0.023}O$ which were all fabricated under 85%Ar + 15%N_2 atmosphere. This is in agreement with previous reports. [10-13] The spectra of these samples show a distinct pre-edge peak A. On the contrary, the present spectrum of CoO with the rocksalt structure shows only a weak pre-edge peak A due to the octahedral symmetry of cobalt ion in CoO. Feature A with almost the same intensity as these samples appears for the reference Co_3O_4 with the spinel structure, in which one third of cobalt ions exist in tetrahedral sites and the rest are located in

octahedral sites. This observation provides evidence for the incorporation of cobalt ion into the tetrahedral site of the wurzite ZnO lattice, in agreement with several reports.[10,12,14,15]

$Zn_{0.961}Co_{0.039}O$ was fabricated under 80%Ar + 20%O_2 atmosphere. There is a positive shift in energy of the $Zn_{0.961}Co_{0.039}O$ spectrum relative to those of the samples stated above. The drop in intensity and shift of peak C to higher energy implies the valence state of Co changes to a higher oxidation state and is about +2.67 as the final spectrum lies near to Co_3O_4 at the pre-edge region. Therefore, a portion of Co in $Zn_{0.961}Co_{0.039}O$ might have formed Co_3O_4 clusters. The Co oxides might have already formed during the sputtering process as Co might have reacted with the O_2 gas in the chamber during deposition before they enter the Zn lattice.

A comparison with Co metal in terms of chemical shift at the pre-edge region reveals a Co valence state between 0 and 1 in $Zn_{0.809}Co_{0.191}O$ and $Zn_{0.790}Co_{0.210}O$, and this suggests a phase transition due to the precipitation of metastable Co from ZnO. Peaks C and D also broaden and their intensities decrease significantly, implying that a large proportion of Co metal has precipitated from $Zn_{0.809}Co_{0.191}O$ and $Zn_{0.790}Co_{0.210}O$ samples. The solubility limit of Co into ZnO for equilibrium film growth process is about 14.5~18.0%.[16]

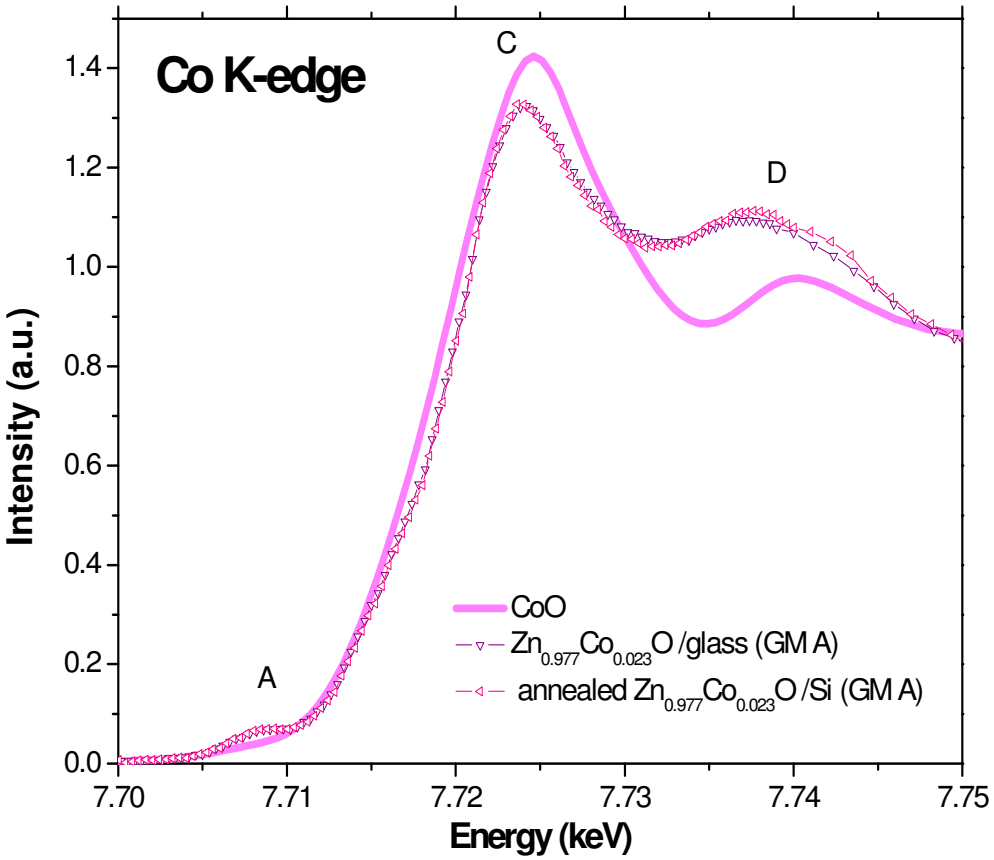

Fig. 5.2. Normalized Co K-edge XANES of annealed $Zn_{0.977}Co_{0.023}O$ film deposited on Si and the as-prepared $Zn_{0.977}Co_{0.023}O$ film grown on glass. GM A stands for 85%Ar + 15%N_2 gas mixture.

$Zn_{0.977}Co_{0.023}O$ films deposited on Si(100) and glass slide are grown under the same conditions. The film deposited on Si(100) is annealed at 800^{o}C; details are given in section 4.5. The normalized Co K-edge XANES spectra of this sample and the as-prepared $Zn_{0.977}Co_{0.023}O$ film grown on glass are depicted in Fig. 5.2. Both spectra are very similar to each other and a valence state 2+ and tetrahedral coordination of Co is identified in both samples via a comparison with the CoO spectrum. No precipitation can be detected in the annealed sample using XANES. These results are further discussed with the EXAFS results.

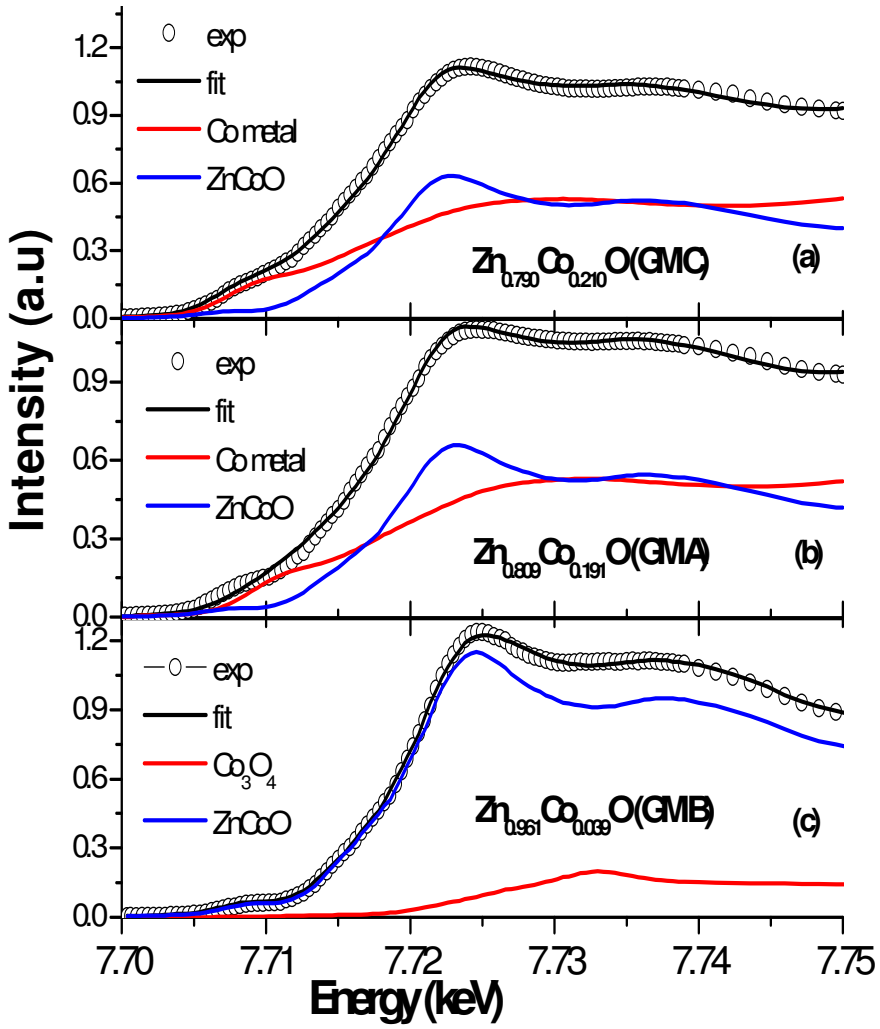

Fig. 5.3. Linear Combination XANES fit of normalized Co K-edge XANES spectra of (a) $Zn_{0.790}Co_{0.210}O$, (b)$Zn_{0.809}Co_{0.191}O$ and (c) $Zn_{0.961}Co_{0.039}O$, all deposited on glass. GM A, GM B and GM C stand for 85%Ar + 15%N_2, 80%Ar + 20%O_2 and Ar gas mixture, respectively.

Fig. 5.3 shows the Linear Combination (LC) -XANES fit by a combination of cobalt metal and ZnCoO for $Zn_{0.790}Co_{0.210}O$ and $Zn_{0.809}Co_{0.191}O$; Co_3O_4 and ZnCoO for $Zn_{0.961}Co_{0.039}O$. The results of the fit are tabulated in table 5.1. At the first approximation, $Zn_{0.961}Co_{0.039}O$ consists of 14.0% Co_3O_4 and 86.0% of interstitial Co^{2+} substituted in Zn sites, consistent with the XANES analysis. For $Zn_{0.790}Co_{0.210}O$ and $Zn_{0.809}Co_{0.191}O$, 48.1% Co metal and 51.9% of

interstitial Co^{2+} substituted in Zn sites and 47.1% Co metal and 52.9% of interstitial Co^{2+} substituted in Zn sites, respectively, were resolved. Clearly, a significant proportion of Co metal has precipitated in both samples.

Table. 5.1. Results of the Fit to Co K-edge XANES of $Zn_{0.961}Co_{0.039}O$, $Zn_{0.809}Co_{0.191}O$ and $Zn_{0.790}Co_{0.210}O$ films giving % of interstitial Co and Co precipitation.

Samples	% of interstitial Co substituted in Zn sites	% of Co_3O_4 precipitation
$Zn_{0.961}Co_{0.039}O$	86.0	14.0
Samples	% of Co substituted in Zn sites	% of Co metal precipitation
$Zn_{0.809}Co_{0.191}O$	47.1	52.9
$Zn_{0.790}Co_{0.210}O$	48.1	51.9

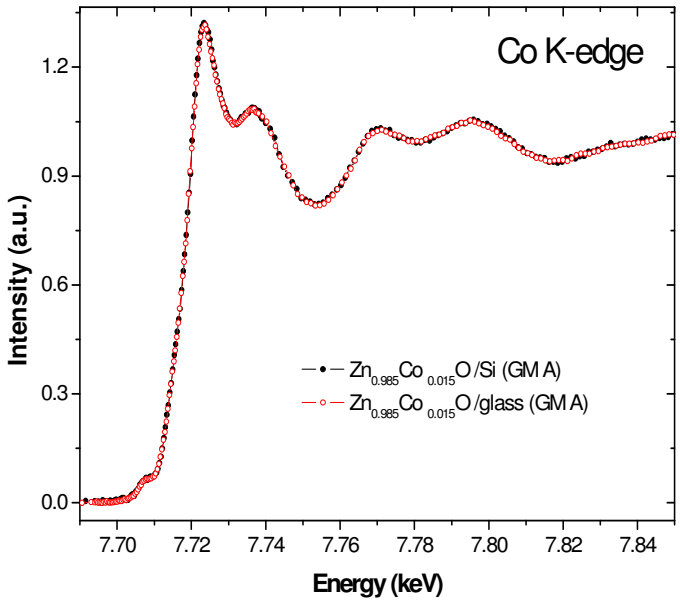

Fig. 5.4. Normalized Co K-edge EXAFS of $Zn_{0.985}Co_{0.015}O$ films grown on glass and Si (100). GM A stands for 85%Ar + 15%N_2 gas mixture.

Fig. 5.4 illustrates the normalized Co K-edge EXAFS spectra of $Zn_{0.985}Co_{0.015}O$ films grown on glass and Si (100) under the same

conditions. The two spectra overlap very well which implies that the chemical state and the local atomic structures of Co in the films deposited on glass and Si(100) are identical. Thus, XAFS experiments were only performed on films grown on glass substrates.

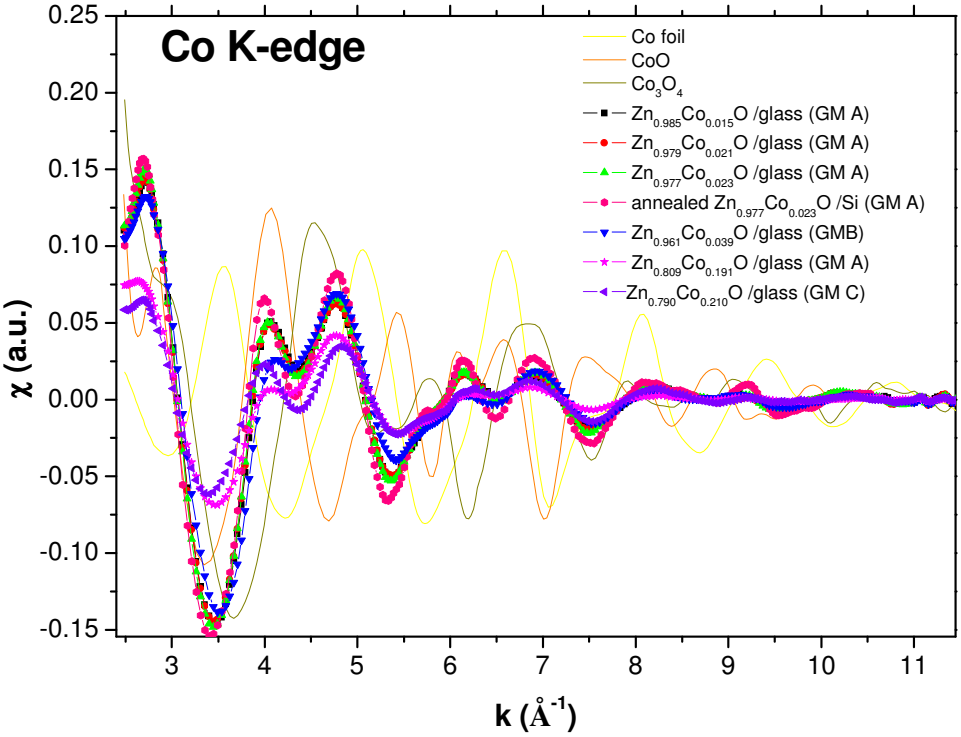

Fig. 5.5. Co K-edge EXAFS function of Co-doped ZnO films deposited on glass and reference samples. GM A, GM B and GM C stand for 85%Ar + 15%N_2, 80%Ar + 20%O_2 and Ar gas mixture, respectively.

Fig. 5.5 shows the Co K-edge EXAFS functions of Co-doped ZnO films and reference samples by extracting the oscillation part from the free atomic absorption background. A significant decrease in intensity of the XAFS amplitude can be observed for samples $Zn_{0.790}Co_{0.210}O$ and $Zn_{0.809}Co_{0.191}O$ as compared to others, indicating a significant structural change.

The Fourier transform (FT) magnitudes of the Co K-edge EXAFS function of the Co-doped ZnO films and reference samples are shown in Fig. 5.6. The magnitude of the FT peak is related to the coordination number (CN) and the Debye-Waller (DW) factor (σ^2), and the trends of Fig. 5.6 for $Zn_{0.985}Co_{0.015}O$, $Zn_{0.979}Co_{0.021}O$, $Zn_{0.977}Co_{0.023}O$ and $Zn_{0.961}Co_{0.039}O$ can be quantitatively described by the 2-shell data fit in Fig. 5.7 and the fitting results tabulated in Table 5.2. Table 5.2 also lists the radial structure of the first two coordination shells for the reference samples used in the study which were extracted from crystallographic data of these oxides. The data fit for $Zn_{0.809}Co_{0.191}O$ and $Zn_{0.790}Co_{0.210}O$ are not included since it is evident that Co metal is present in both samples. In the FT, the XAFS function in the range 2.4-11.4$Å^{-1}$ in k space was extracted for Co K-edge. The CN, inter-atomic distance (R), DW factor (σ^2) and the energy shift (E_0) were free variables during the fitting. σ^2 refers to the mean-square relative displacement and accounts for the thermal and static disorder effects associated with the movement of atoms about their equilibrium position, and is extracted from the fit to EXAFS. These parameters are associated with a certain local coordination shell and averaged over all absorbers in the sample. The inelastic factor, s_0^2, was extracted from a fit to the reference sample and was fixed at 0.85 in the fit.

As shown in Fig. 5.6, the first peak at about 1.6Å is due to nearest four Co-O or Zn-O pairs in the first shell. The second peak situated at about 2.95Å corresponds to the second shell of mainly twelve Co-Zn or Zn-Zn pairs (for ZnO), and the third peak at approximately 4.3Å arises mainly from the third coordination shell comprising 9 O atoms. The third coordination peaks are almost smeared out due to long range disorder in the samples.

The position of the first Co-O peak does not change significantly for $Zn_{0.985}Co_{0.015}O$, $Zn_{0.979}Co_{0.021}O$ and $Zn_{0.977}Co_{0.023}O$ relative to the Zn-O peak because when Co^{2+} ions are incorporated into the ZnO lattice; R_{Co-}

$_O$ changes only by at about 0.01Å. It can be seen that R_{Co-O} and R_{Co-Zn}, displayed in Table 5.2 are very close to R_{Zn-O} and R_{Zn-Zn} of their bulk counterpart (1.97Å and 3.21Å). In addition, the CN of the first Co-O shell for these samples did not exceed 4, hence the majority of the Co^{2+} ions have been incorporated into the substitutional sites of the Zn lattice and they are of tetrahedral coordination in the first shell.

Broadening of the Co-O and Co-Zn peaks in the Co K-edge FT displayed in Fig.5.6 is observed for $Zn_{0.961}Co_{0.039}O$. R_{Co-O} decreases relative to R_{Zn-O} and is 1.94Å, close to the theoretical value of Co_3O_4 (1.93Å) [5]. It is clear that not all Co ions are dissolved in the ZnO wurtzite lattice; part of them is deposited to form Co_3O_4 precipitate. This result is supported by the fact that the Co constituents of $Zn_{0.961}Co_{0.039}O$ are 14.0% Co_3O_4 and 86.0% of interstitial Co^{2+} substituted in Zn sites as given by the LC-XANES fitting results in Table 5.1.

A significant difference in $Zn_{0.809}Co_{0.191}O$ and $Zn_{0.790}Co_{0.210}O$ can be observed, as indicated by the broadening of the Co-O in the Co K-edge FT. The Co-O peak displays an evident shift toward high R in the $Zn_{0.790}Co_{0.210}O$ spectrum and this is more likely caused by the presence of Co metal which has a bigger R_{Co-Co} as compared R_{Co-O}. LC-XANES fit results in Table 5.1 agree with these results that the Co constituents of $Zn_{0.790}Co_{0.210}O$ and $Zn_{0.809}Co_{0.191}O$ are 48.1% Co metal and 51.9% of interstitial Co^{2+} substituted in Zn sites and 47.1% Co metal and 52.9% of interstitial Co^{2+} substituted in Zn sites, respectively.

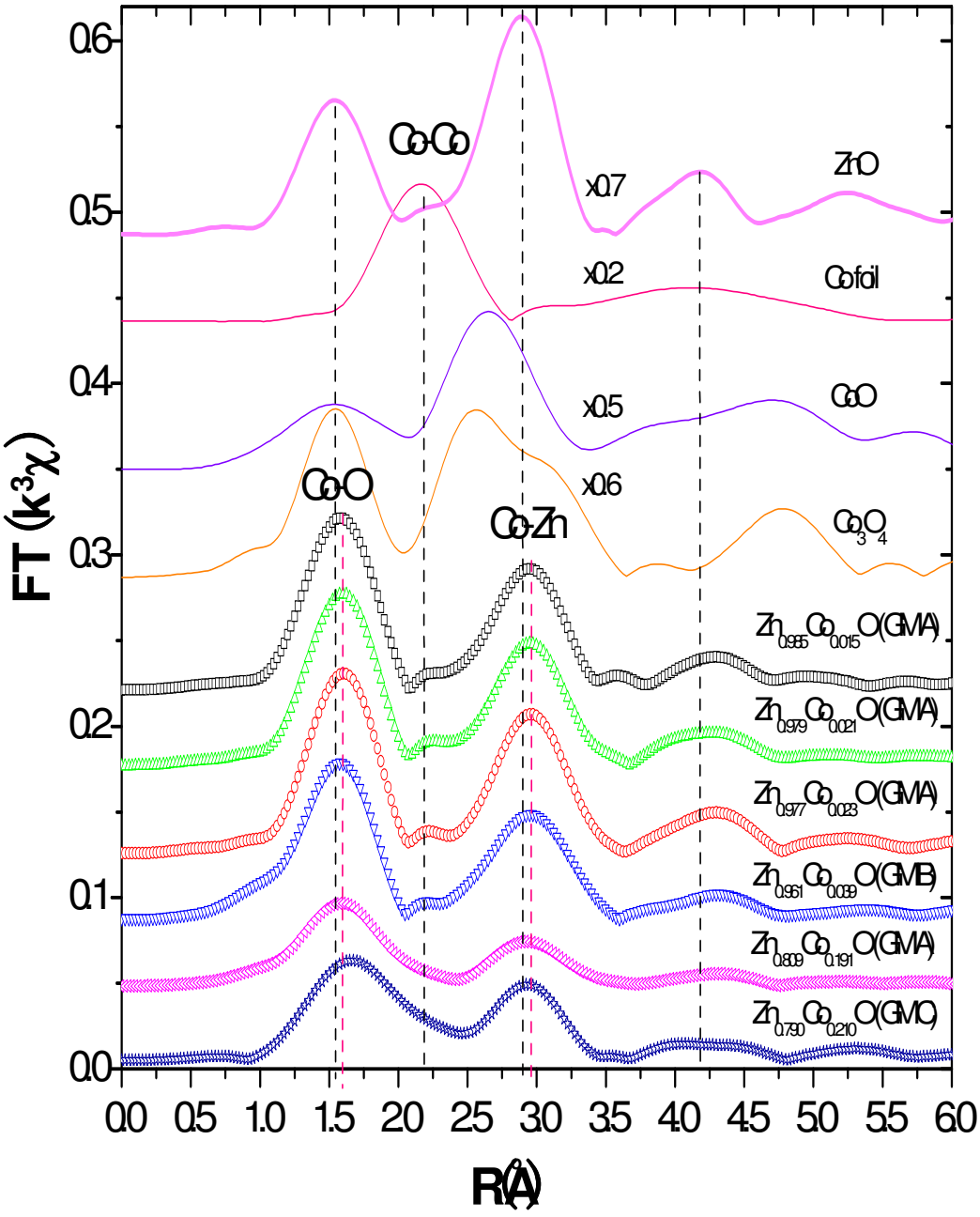

Fig. 5.6. Fourier transform magnitudes of the Co K-edge EXAFS function of Co-doped ZnO films deposited on glass and reference samples. The first peak situated at approximately 1.6Å is due to Co-O or Zn-O co-ordinations of the first shell. The second peak at about 2.9Å is due to Co-Zn or Zn-Zn coordinations of the second shell. GM A, GM B and GM C stand for 85%Ar + 15%N_2, 80%Ar + 20%O_2 and Ar gas mixture, respectively.

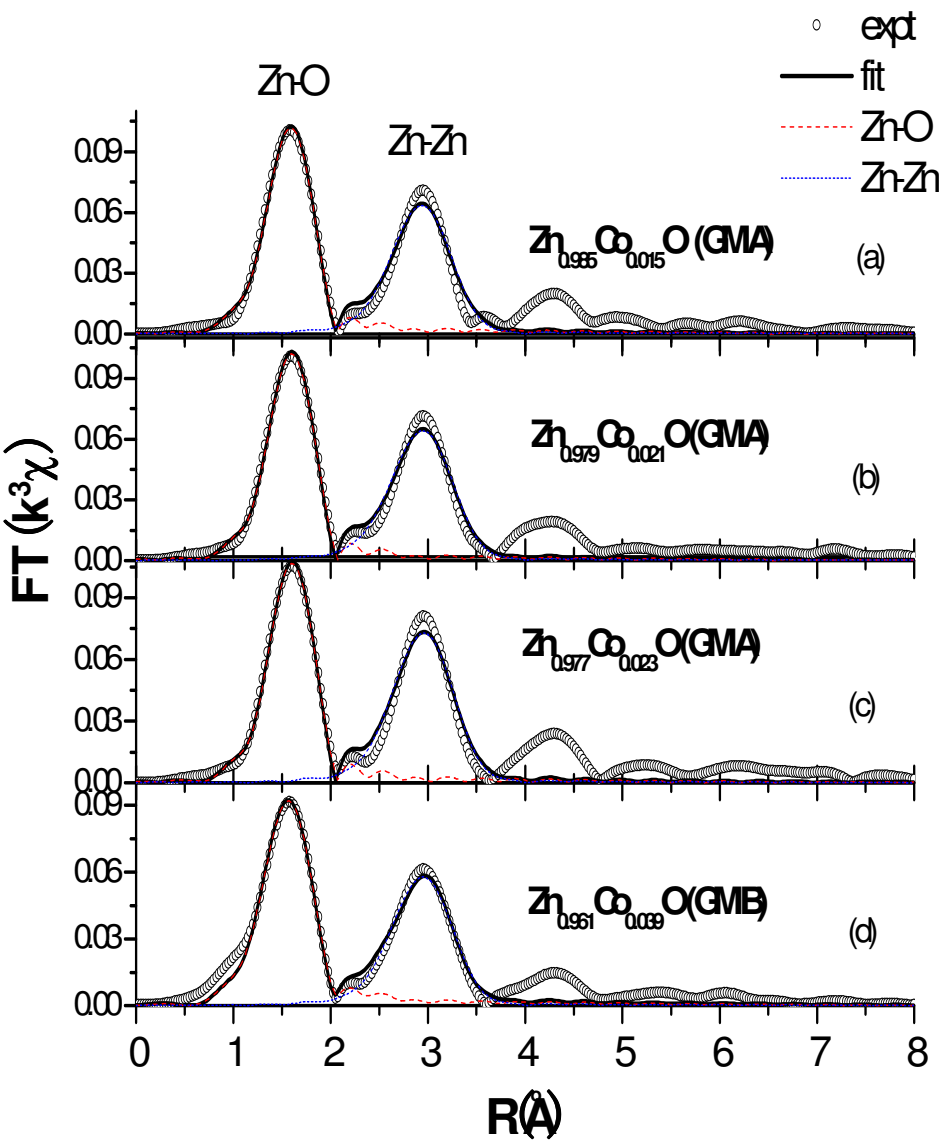

Fig. 5.7. Two shell-fit data fit (Zn-O and Co-Zn respectively) to the FT of (a) $Zn_{0.985}Co_{0.015}O$, (b) $Zn_{0.979}Co_{0.021}O$, (c) $Zn_{0.977}Co_{0.023}O$ and (d) $Zn_{0.961}Co_{0.039}O$, all deposited on glass, at the Co K-edges. GM A and GM B stand for 85%Ar + 15%N_2 and 80%Ar + 20%O_2 gas mixture, respectively.

Table. 5.2. Results of the Fit to Co K-edge EXAFS of the Co-O and Co-Zn shells in $Zn_{0.985}Co_{0.015}O$, $Zn_{0.979}Co_{0.021}O$, $Zn_{0.977}Co_{0.023}O$ and $Zn_{0.961}Co_{0.039}O$ films. [a]

Co K-edge	Co-O/ Zn-O/ Co-Co			Co-Zn/ Zn-Zn/ Co-Co		
	CN	R	σ^2	CN	R	σ^2
ZnO	4.0	1.97	--	12.0	3.21	--
Co	12.0	2.50	--	6.0	3.54	--
CoO	6.0	2.13	--	12.0	3.02	--
Co_3O_4	4.0/ 6.0	1.93	--	12.0	3.34	--
$Zn_{0.985}Co_{0.015}O$ /glass	3.9	1.97	0.0041	9.5	3.23	0.0137
$Zn_{0.979}Co_{0.021}O$ /glass	3.6	1.97	0.0031	13.0	3.24	0.0164
$Zn_{0.977}Co_{0.023}O$ /glass	3.5	1.98	0.0023	11.6	3.25	0.0142
$Zn_{0.961}Co_{0.039}O$ /glass	4.0	1.94	0.0059	9.3	3.24	0.0143
$Zn_{0.977}Co_{0.023}O$ /Si, annealed	3.3	1.95	0.0005			

[a] CN, *R* (Å), and σ^2 (Å^2) are the coordination number, inter-atomic distance, and Debye-Waller factor, respectively. The uncertainties for CN, R, and σ^2 are 10%, 0.01 Å, and 10%, respectively.

Fig. 5.8 illustrates the FT magnitudes of the Co K-edge EXAFS of annealed $Zn_{0.977}Co_{0.023}O$ film deposited on Si and the as-prepared $Zn_{0.977}Co_{0.023}O$ film grown on glass. Only the Co-O shell was fitted for the annealed sample at Co K-edge and the data fit is displayed in Fig. 5.9 while the fitting results are tabulated in Table 5.2. The annealed sample shows a smaller Co-O bond length (1.95Å) relative to the as-prepared sample (1.98Å), as observed from the shift toward low *R* of the corresponding FT peak. It is likely that precipitates similar to Co_3O_4 (1.93Å) have formed due to calcination after the sample was heated at 800^{o}C for an hour in air. However, this is not very evident based on the XANES results.

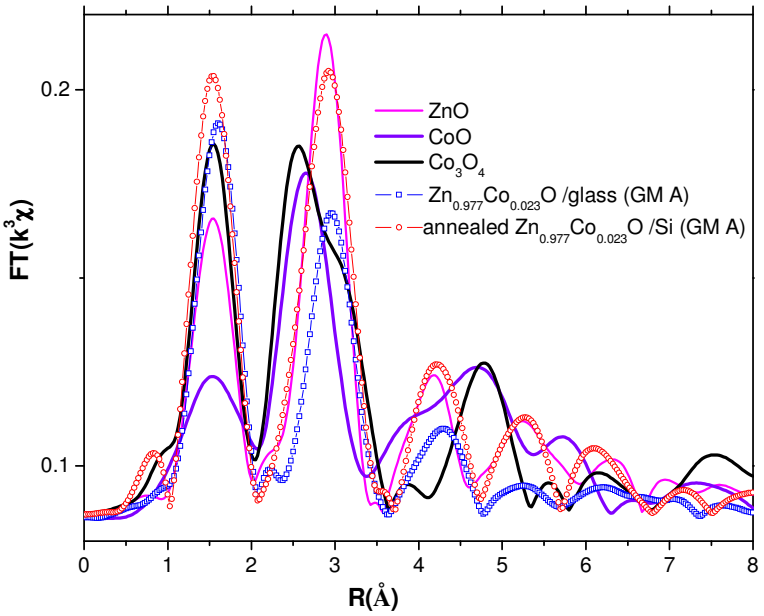

Fig. 5.8. Fourier Transform magnitudes of the Co K-edge EXAFS function of the as-prepared $Zn_{0.977}Co_{0.023}O$ film deposited on glass, annealed $Zn_{0.977}Co_{0.023}O$ film deposited on Si and reference samples. GM A stands for 85%Ar + 15%N_2 gas mixture.

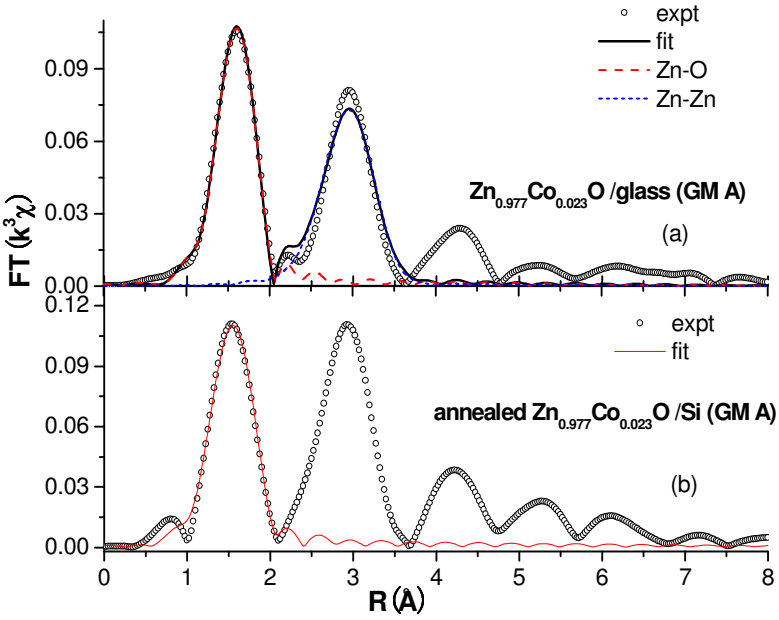

Fig. 5.9. Two shell-fit data fit (Zn-O and Zn-Zn respectively) to FT of the EXAFS function of (a) the as-prepared $Zn_{0.977}Co_{0.023}O$ deposited on glass; one shell-fit data (Zn-O) to FT of the EXAFS function of (b) annealed $Zn_{0.977}Co_{0.023}O$ deposited on Si(100) at the Co K-edges. GM A stands for 85%Ar + 15%N_2 gas mixture.

It can be concluded that the percolation threshold of Co into ZnO cannot exceed 19% even though reactive magnetron sputtering is a non-equilibrium film growth process. The majority of Co^{2+} ions have been incorporated into the substitutional sites of the Zn lattice for low Co doping content and they replace the Zn ions, adopting a tetrahedral coordination. Co_3O_4 clusters are formed when subjected to 800°C calcination and when the ambient in which the films are fabricated consists of 20% oxygen gas.Co metal are the major precipitates when the solubility limit is exceeded.

5.2.2 Cu-doped ZnO films

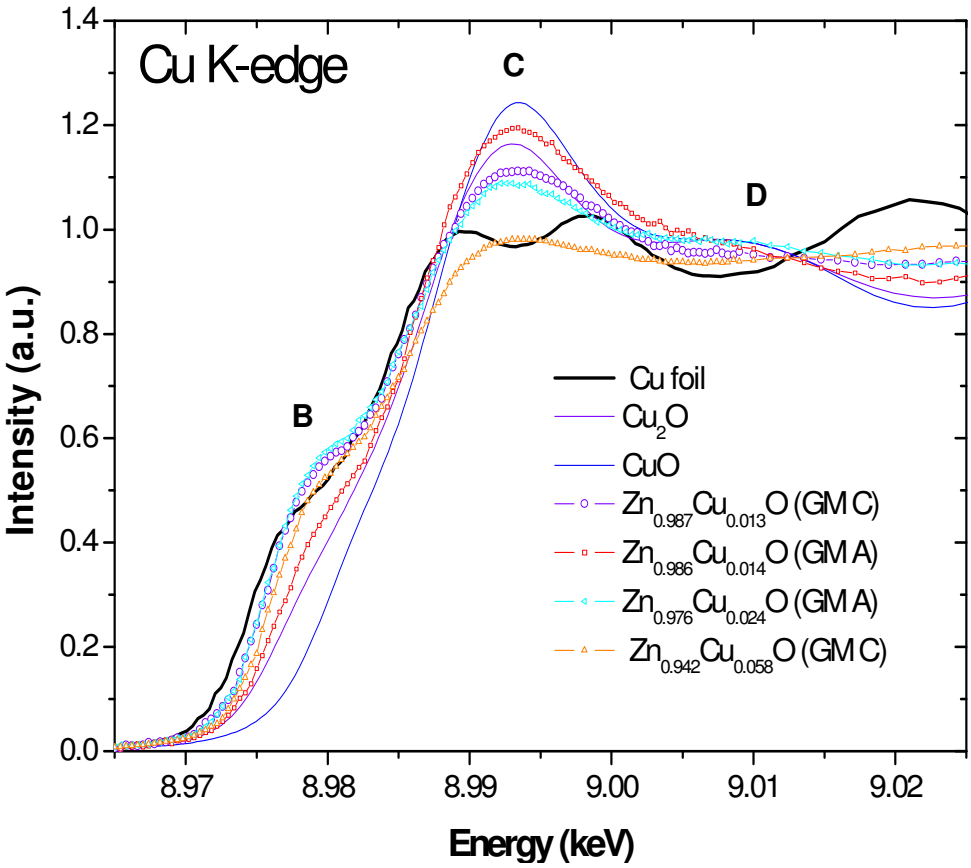

Fig. 5.10. Normalized Cu K-edge XANES of Cu-doped ZnO films deposited on glass, Cu foil, Cu_2O and Cu. GM A and GM C stand for 85%Ar + 15%N_2 and Ar gas mixture, respectively.

Fig. 5.10 compares the normalized Cu K-edge XANES spectra of Cu-doped ZnO films deposited on glass with those of pure Cu, Cu_2O and CuO. Three main features are identified in the XANES spectrum in Fig. 5.10: the shoulder peak B, the dominant main peak C and the shoulder D at the post-edge region. Pre-edge peak A represents electronic transition from 1s to the unoccupied 3d final states and its absence from the Cu K-edge XANES spectrum is due to the filled 3d orbital of Cu ions in Cu-doped ZnO samples. Shoulder peak B can be attributed to the unfilled anti-bonding states of hybridized molecular orbitals and arises from the 4p-character of the density of states of Cu. The shoulder D mainly arises from the interaction of central absorber with the distant coordination atoms, in particular, the third shell of 9 O atoms. In interpreting the XANES features of TM oxides, this peak was generally explained as an indication of middle-range-ordering from the MS point of view.[8,17] The lack of middle-range-ordering around the absorber can lead to a damping shoulder D, this may be the case for Cu-doped samples. A comparison with reference spectra in Fig. 5.10 in terms of chemical shift indicates a valence state of between 0 and 1+ of Cu in all the samples.

$Zn_{0.987}Cu_{0.013}O$ was fabricated under pure Ar atmosphere. The spectrum of $Zn_{0.987}Cu_{0.013}O$ has a very prominent shoulder B and this indicates the onset of precipitation of Cu or Cu oxides. The lattice of this sample is highly distorted as can be seen by the smeared out feature D, leading to the amorphous structure of the sample. Even though the Cu doping concentration is very low in this sample, Cu precipitation might have occurred since the deposition rate in Ar atmosphere is much higher as compared to the other gas mixtures of Ar, N_2 and O_2. In addition, the sputtering rate of Cu metal also exceeds that of other metallic foils. This might lead to the direct sputtering of Cu metal into ZnO without sufficient time for the diffusion of Cu ions into the ZnO

lattice. Another possible reason for the failure of substitution doping of Cu ions might be due to the low solubility limit(0~1.5%) of Cu in ZnO.[16]

$Zn_{0.986}Cu_{0.014}O$ and $Zn_{0.976}Cu_{0.024}O$ were fabricated under under 85%Ar + 15%N_2 atmosphere. A comparison with the Cu_2O spectrum reveals a valence state 1+ of Cu in $Zn_{0.986}Cu_{0.014}O$, implying a charge transfer from ZnO to Cu. The 1+ valence for Cu-doped ZnO has been reported by Fons et al.[18] on as-prepared Cu doped ZnO thin films grown by molecular beam epitaxy and theoretically predicted by Spaldin et al.[19] and Feng et al.[20]. In fact, Cu has been predicted generally as acceptors in impurity doping of ZnO to produce p-type semiconductors.[19] Peak B in the spectrum of $Zn_{0.986}Cu_{0.014}O$ is of very low intensity as compared to the rest of the samples whereas peak C is very prominent. Peak D is barely visible due to poor crystallinity and disordered lattice structure. However, the substitution of Cu^+ ions in ZnO lattice of this sample is not evident solely based on the XANES results and we have to rely on EXAFS results to give us more information. The shape of this spectrum also resembles that of Cu_2O, and since the Cu ions in Cu_2O also have valence state 1+, it is impossible to distinguish them from the Cu^+ ions incorporated in Zn sites. On the other hand, $Zn_{0.976}Cu_{0.024}O$ resembles that of $Zn_{0.987}Cu_{0.013}O$ with a prominent shoulder B. Hence, this also indicates the possibility of precipitation of small amounts of Cu or Cu oxides.

$Zn_{0.942}Cu_{0.058}O$ was fabricated under pure Ar atmosphere. The spectrum of $Zn_{0.942}Cu_{0.058}O$ is marked by a rather sharp feature B, a subdued and broadened main peak C and an almost non-existent shoulder D. The intensiy of peak C decreases significantly as compared to the rest of the samples, implying the existence of large amounts of Cu metal within the sample.

$Zn_{0.986}Cu_{0.014}O$ films are deposited on Si(100) and glass slides under the same conditions. The film deposited on Si(100) was annealed at

800°C; details are given in section 4.5. Normalized Cu K-edge XANES spectra of this sample and the as-prepared $Zn_{0.986}Cu_{0.014}O$ film grown on glass are displayed in Fig. 5.11. Both spectra are similar to each other and a valence state 1+ of Cu is identified in both samples via a comparison with the Cu_2O spectrum. No precipitation can be detected in the annealed sample through XANES. However, SIMS results (Figs. 4.23 and 4.24) in section 4.5 clearly shows that after annealing $Zn_{0.986}Cu_{0.014}O$ at 800°C for an hour in air, surface precipitation of Cu or Cu oxides is observed. Some Cu ions might have aggregated and generated Cu_2O clusters near the surface. Since the Cu ions in Cu_2O also have valence state 1+, it is impossible to distinguish them from the Cu^+ ions incorporated in Zn sites.

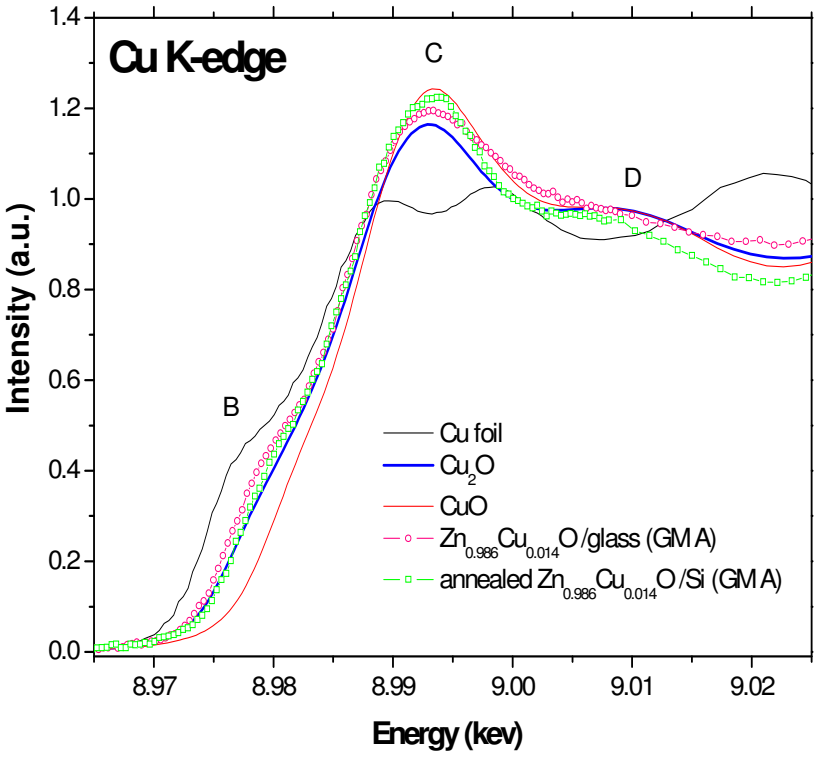

Fig. 5.11. Normalized Cu K-edge XANES spectra of annealed $Zn_{0.986}Cu_{0.014}O$ film deposited on Si(100) and the as-prepared $Zn_{0.986}Cu_{0.014}O$ film grown on glass. GM A stands for 85%Ar + 15%N_2 gas mixture.

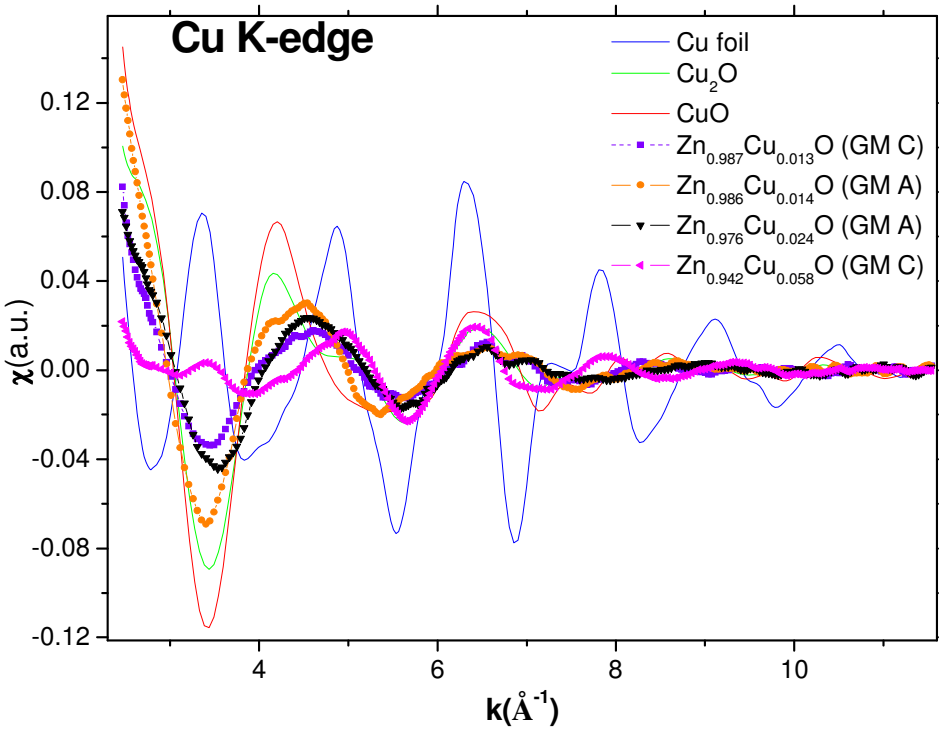

Fig. 5.12. Cu K-edge EXAFS function of the Cu-doped ZnO films deposited on glass and reference samples. GM A and GM C stand for 85%Ar + 15%N_2 and Ar gas mixture, respectively.

Fig. 5.12 shows the Cu K-edge EXAFS functions of Cu-doped ZnO films and reference samples by extracting the oscillation part from the free atomic absorption background. A change in shape and a significant decrease in intensity of the XAFS amplitude are observed for sample $Zn_{0.942}Cu_{0.058}O$, indicating a structural phase transition.

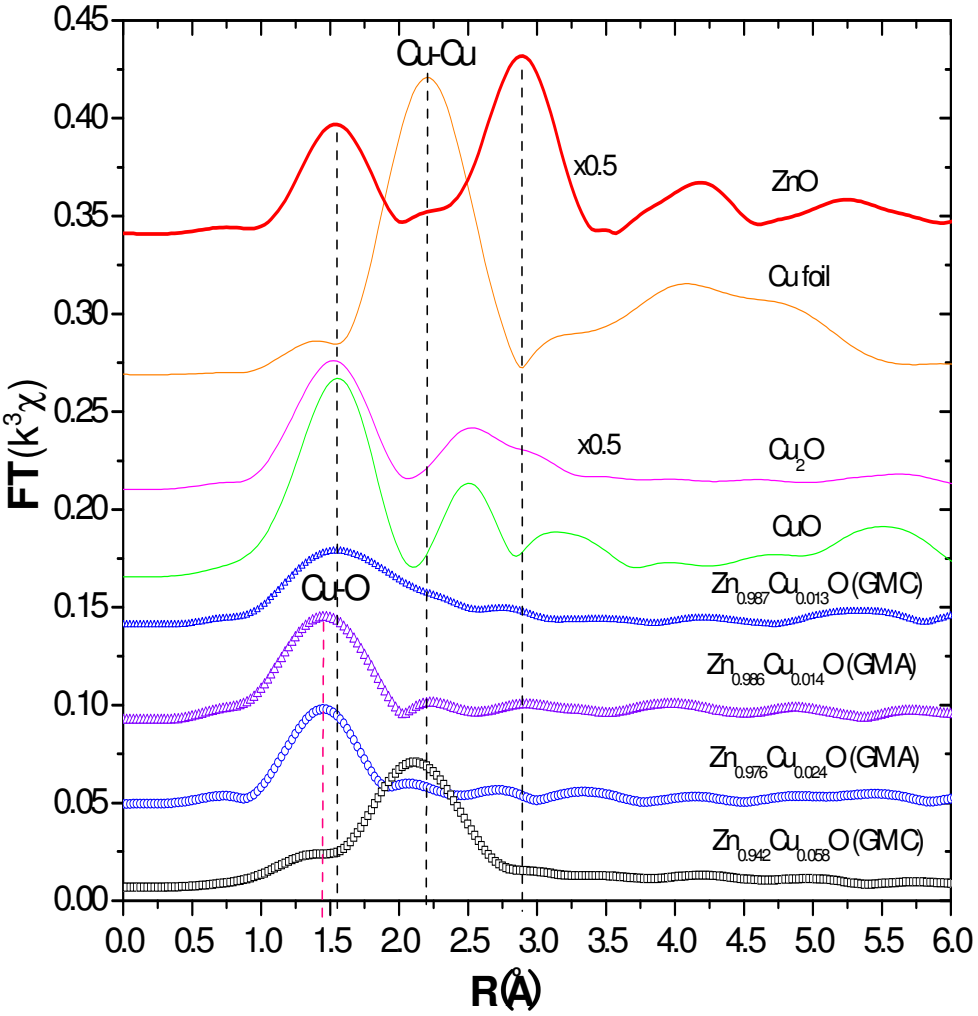

Fig. 5.13. Fourier transform magnitudes of the Cu K-edge EXAFS function of Cu-doped ZnO films deposited on glass and reference samples. GM A and GM C stand for 85%Ar + 15%N_2 and Ar gas mixture, respectively. Phase shift was not corrected.

The Fourier transform (FT) magnitudes of the Cu K-edge EXAFS function of the Cu-doped ZnO films and reference samples are shown in Fig. 5.13. Fig. 5.14 depicts the 1-shell data fit in $Zn_{0.986}Cu_{0.014}O$ and and $Zn_{0.976}Cu_{0.024}O$; the fitting results are tabulated in Table 5.3. Table 5.3 also lists the radial structure of the first coordination shell for the reference samples used in the study which were extracted from crystallographic data of these oxides. Samples with high Cu

concentration are excluded in Fig. 5.13 and Fig. 5.14 because all of them resemble the Cu K-edge EXAFS functions of Cu foil. In the FT, the XAFS function in the range 2.3-11.6Å^{-1} in *k* space was extracted for Cu K-edge. The CN, inter-atomic distance (R), DW factor and the energy shift (E_0) were set as free variables during the fit. The inelastic factor, s_0^2, was extracted from a fit to the reference sample and was fixed at 0.81 in the fit.

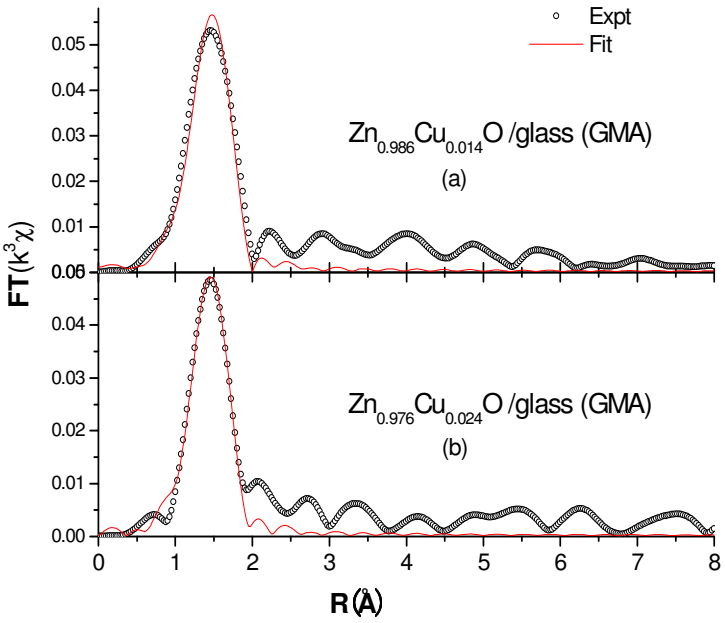

Fig. 5.14. One shell data fit (Zn-O) to FT of the EXAFS functions of (a) $Zn_{0.986}Cu_{0.014}O$ and (b) $Zn_{0.976}Cu_{0.024}O$ films), all deposited on glass, at the Cu K-edges. GM A stands for 85%Ar + 15%N_2 gas mixture.

Table. 5.3. Results of the Fit to Cu K-edge EXAFS of the Cu-O in $Zn_{0.986}Cu_{0.014}O$ and $Zn_{0.976}Cu_{0.024}O$ films.[a]

Cu K-edge	Cu-O/ Zn-O/ Cu-Cu		
	CN	R	σ^2
ZnO	4.0	1.97	--
Cu	12.0	2.56	--
Cu_2O	2.0	1.85	--
CuO	4.0	1.95	--
$Zn_{0.986}Cu_{0.014}O$ /glass	3.0	1.90	0.0066
$Zn_{0.976}Cu_{0.024}O$ /glass	1.8	1.86	0.0032

[a] CN, *R* (Å), and σ^2 (Å^2) are the coordination number, inter-atomic distance, and Debye-Waller factor, respectively. The uncertainties for CN, R, and σ^2 are 10%, 0.01 Å, and 10%, respectively.

In the Cu K-edge EXAFS functions of $Zn_{0.986}Cu_{0.014}O$ and $Zn_{0.976}Cu_{0.024}O$ shown in Fig. 5.13, the first peak at about 1.4Å (phase shift was not corrected) is due to nearest four Cu-O or Zn-O pairs (for ZnO) at the first shell. The fit to the Cu-O coordination yields R_{Cu-O} of 1.90Å and 1.86Å for $Zn_{0.986}Cu_{0.014}O$ and $Zn_{0.976}Cu_{0.024}O$ respectively as listed in Table 5.3. These samples show much smaller R_{Cu-O} relative to R_{Zn-O} (1.97Å), as observed from the shift toward low *R* of the corresponding FT peak. The second coordination peaks are basically non-existent due to poor crystallinity and significant distortion of the lattice caused by doping. In addition, the CN of the Cu-O shell for these samples is very much lower than 4, hence the FT fitted results clearly demonstrates the formation of Cu_2O local structure whose R_{Cu-O} value is 1.85Å and the number of nearest oxygen neighbors is 2, consistent with the XANES analysis, indicative of Cu precipitation from the wurtzite lattice and formation of Cu_2O. $Zn_{0.976}Cu_{0.024}O$ evidently contains more Cu_2O clusters than $Zn_{0.986}Cu_{0.014}O$ with its lower CN and smaller R_{Cu-O} due to its higher Cu doping concentration. Tao et al.[21] has

also reported similar findings on the precipitation of Cu_2O clusters in Cu-doped ZnO nanoparticles calcinated at 400^oC.

The broadening of the Cu-O peak in the Cu K-edge FT displayed in Fig. 5.13 is observed for $Zn_{0.987}Cu_{0.013}O$. In addition, this peak displays an evident shift toward high R and this is attributed to the presence of Cu metal which has a bigger R_{Cu-Cu} as compared to R_{Cu-O}. The position of the Cu-O shell peak for $Zn_{0.942}Cu_{0.058}O$ is very close to the Cu-Cu peak of Cu foil, which is a clear indication that majority of the Cu have aggregated and precipitated as pure Cu in this sample, in agreement with XANES results.

It can be concluded that Cu ions in ZnO matrix are not stable against 400°C calcination and tend to precipitate easily as Cu or Cu_2O. Also, the ZnO lattice is greatly distorted with Cu doping, distinct from Mn and Co doping in ZnO. The solubility of Cu into ZnO is extremely low (less than 1.3%) even though reactive magnetron sputtering is a non-equilibrium film growth process. The substituted Cu ions at the Zn sites have a valence state of 1+. Cu_2O and metallic Cu are the main precipiates when the percolation threshold is exceeded.

5.2.3 Ti-doped ZnO films

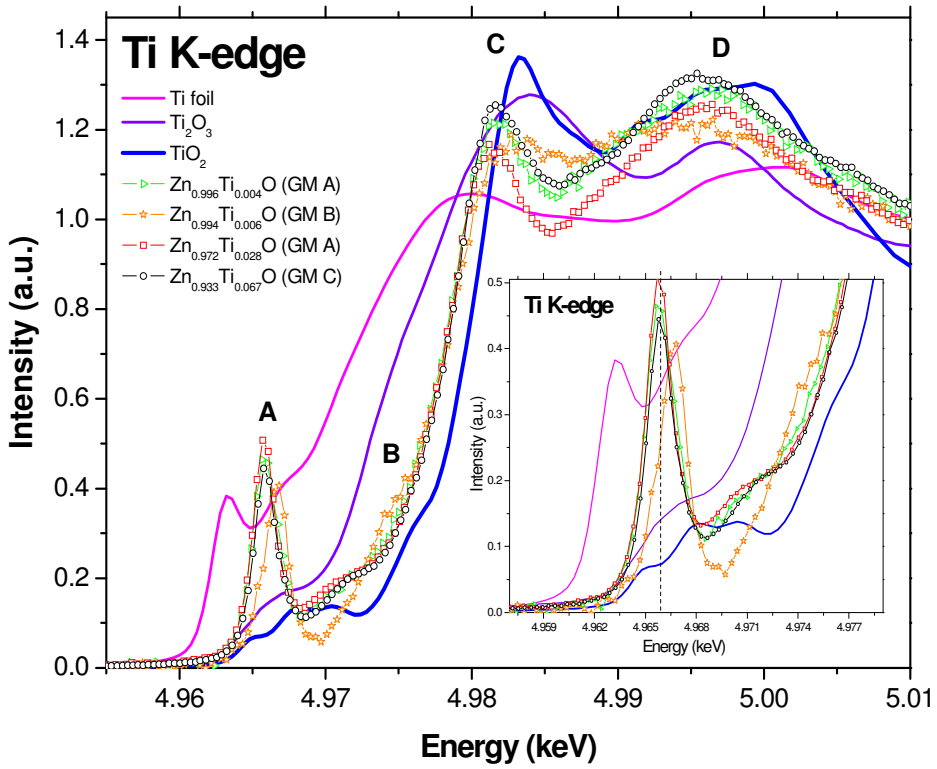

Fig. 5.15. Normalized Ti K-edge XANES of Ti-doped ZnO films deposited on glass, Ti foil, Ti_2O_3 and TiO_2. Inset: the pre-edge region of the spectra. GM A, GM B and GM C stand for 85%Ar + 15%N_2, 80%Ar + 20%O_2 and Ar gas mixture, respectively.

Fig. 5.15 compares the normalized Ti K-edge XANES spectra of Ti-doped ZnO films deposited on glass with those of pure Ti foil, Ti_2O_3 and TiO_2. Four main features are identified in the XANES spectra in Fig. 5.15: a very sharp pre-edge peak A, the shoulder peak B, the dominant main peak C and the shoulder D at the post-edge region. Feature A corresponds to the electronic transition from 1s to the unoccupied 3d final states and is very prominent due to the almost empty 3d orbital of Ti and the non-centrosymmetric tetrahedral geometry of an absorbing atom through the mixing of d–p orbitals.[10]

$Zn_{0.996}Ti_{0.004}O$ and $Zn_{0.972}Ti_{0.028}O$ were fabricated under 85%Ar + 15%N_2 ambient. $Zn_{0.933}Ti_{0.067}O$ was fabricated under pure Ar ambient. The XANES spectra of these samples display very prominent pre-edge peak A. This observation provides direct evidence for the substitutional incorporation of Ti ions into the tetrahedral zinc sites in the wurzite ZnO lattice. On the contrary, the spectra of Ti_2O_3 and TiO_2 show only weak pre-edge peak A due to the octahedral local structures around Ti ions. A comparison with the Ti_2O_3 spectrum in terms of chemical shift at the peak A reveals a valence state close to 3+ of Ti in these samples, indicating that the Ti atoms act as donors[22,23] by supplying an electron or they create zinc vacancies (V^0 centers)[22] when Ti^{3+} occupies Zn^{2+} sites. Venkatesan et al.[24] reported the 3+ valence state of Ti in Ti-doped ZnO fabricated using conventional pulsed laser deposition.

$Zn_{0.994}Ti_{0.006}O$ was fabricated under 80%Ar + 20%O_2 ambient. There is a positive chemical shift in peak A for this sample relative to those of the samples stated above. The drop in intensity and shift of peak A to higher energy implies the valence state of Ti changes to a higher oxidation state and is between 3 and 4 as it lies in between those of Ti_2O_3 and TiO_2. Peak C also broadens and its intensity is much lower than the rest. Although the Ti doping concentration is extremely low in this sample, a portion of titanium oxides or zinc titanate might have formed during the sputtering process. The Ti ions sputtered from the target might have reacted with the oxygen ions and formed oxide precipitates.

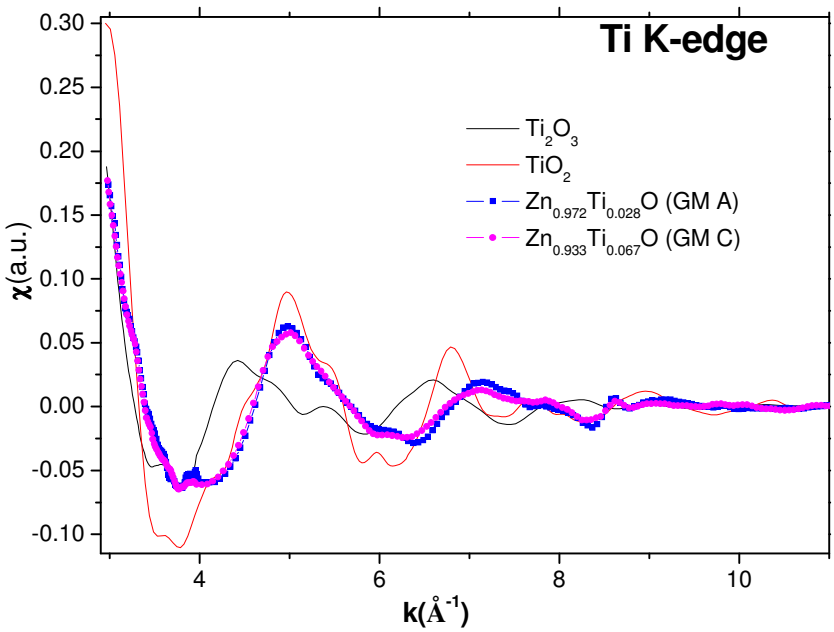

Fig. 5.16. Ti K-edge EXAFS functions of $Zn_{0.972}Ti_{0.028}O$ and $Zn_{0.933}Ti_{0.067}O$ films deposited on glass and reference samples. GM A and GM C stand for 85%Ar + 15%N_2 and Ar gas mixture, respectively.

Fig. 5.16 shows the Ti K-edge EXAFS functions of $Zn_{0.972}Ti_{0.028}O$ and $Zn_{0.933}Ti_{0.067}O$ films and reference samples. The data for $Zn_{0.996}Ti_{0.004}O$ and $Zn_{0.994}Ti_{0.006}O$ are not available because of the poor statistics due to low Ti concentrations and the heavy matrix background. It is noted that the EXAFS functions for $Zn_{0.972}Ti_{0.028}O$ and $Zn_{0.933}Ti_{0.067}O$ are very similar.

The Fourier transform (FT) magnitudes of the EXAFS function of $Zn_{0.972}Ti_{0.028}O$, $Zn_{0.933}Ti_{0.067}O$ films and reference samples are illustrated in Fig. 5.17. Fig. 5.18 gives the data fit for the first Ti-O shell in $Zn_{0.972}Ti_{0.028}O$ and $Zn_{0.933}Ti_{0.067}O$; the fitting results are tabulated in Table 5.4. Table 5.4 also lists the radial structural parameters of the first coordination shell for the reference samples used in the study which were extracted from crystallographic data. In the FT, the XAFS function in the range 2.9-11.0Å in k space was extracted for Ti K-edge. The CN, R, DW factor and E_0 were set as free variables

during the fit. The inelastic factor, s_0, was extracted from a fit to the reference sample and was fixed at 0.90 in the fit.

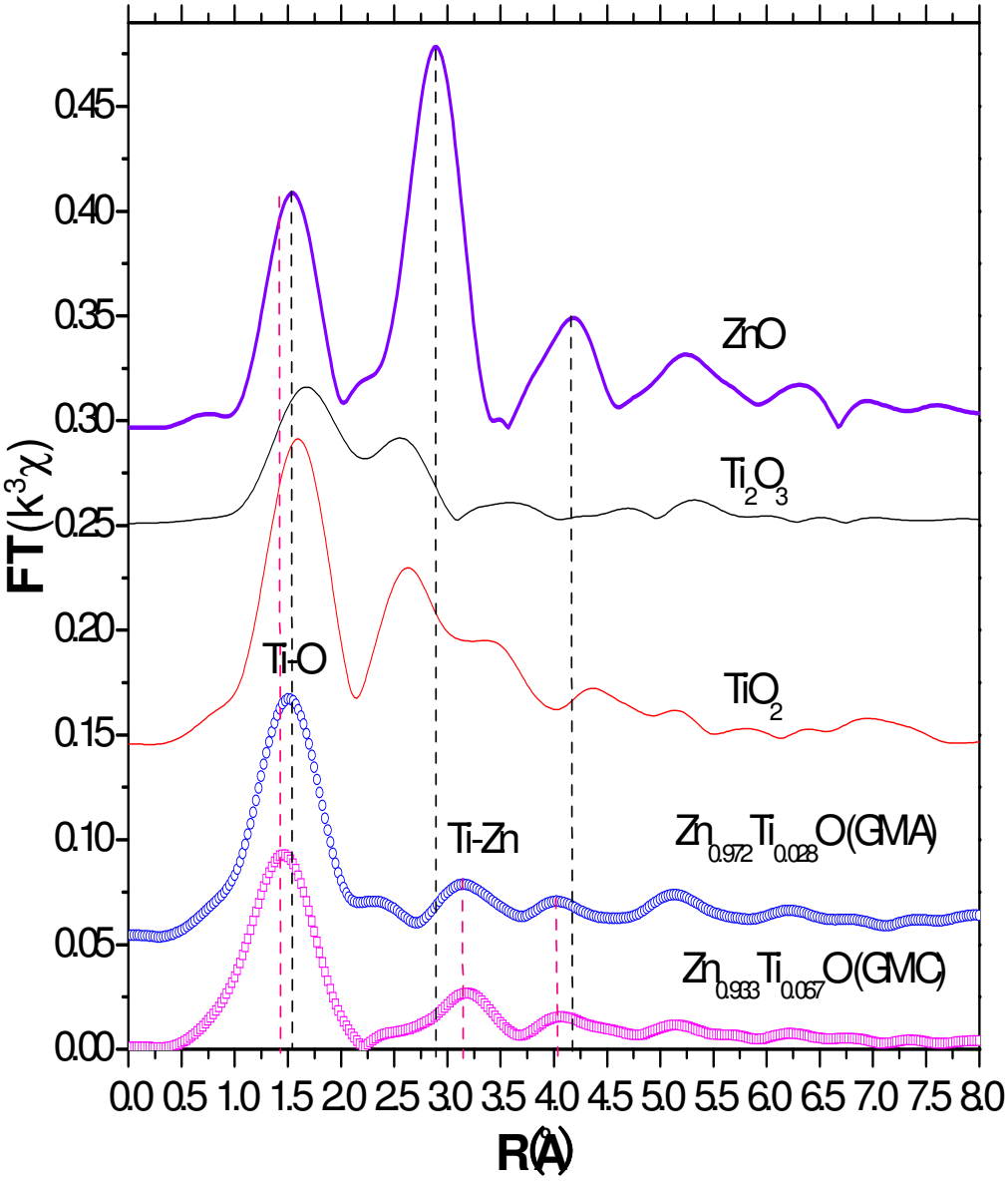

Fig. 5.17. Fourier Transform magnitudes of the Ti K-edge EXAFS function of Ti-doped ZnO films deposited on glass and reference samples. The first peak at 1.4~1.5Å is due to Ti-O or Zn-O coordinations of the first shell. The second peak at about 3.15~3.2Å is due to Co-Zn or Zn-Zn co-ordinations of the second shell. GM A and GM C stand for 85%Ar + 15%N_2 Ar gas mixture, respectively. Phase shift was not corrected.

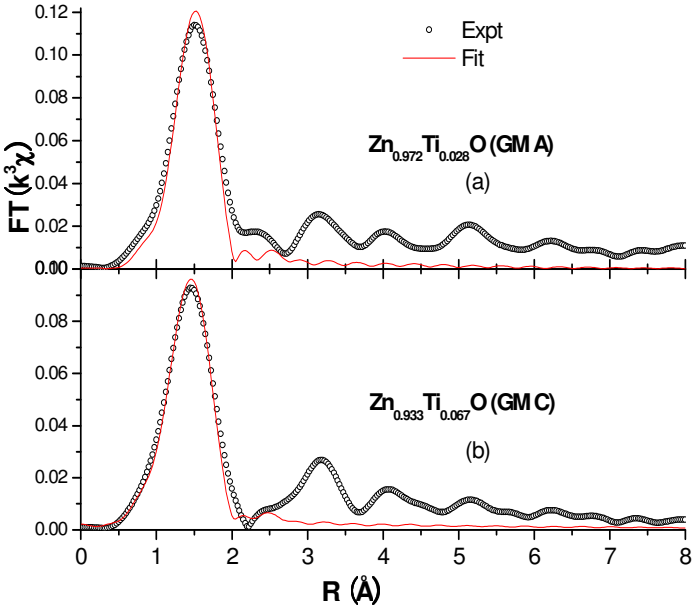

Fig. 5.18. One shell-fit data fit (Ti-O) to the first peak in FT of (a) $Zn_{0.972}Ti_{0.028}O$, (b) $Zn_{0.933}Ti_{0.067}O$ film deposited on glass. GM A and GM C stand for 85%Ar + 15%N_2 Ar gas mixture, respectively.

Table. 5.4. Results of the Fit to the Ti-O shell in $Zn_{0.972}Ti_{0.028}O$ and $Zn_{0.933}Ti_{0.067}O$ films.[a]

Ti K-edge	Ti-O/ Zn-O		
	CN	R	σ^2
ZnO	4.0	1.97	--
Ti_2O_3	6.0	2.05	--
TiO_2	6.0	1.95	--
$Zn_{0.972}Ti_{0.028}O$ /glass	4.3	1.89	0.0044
$Zn_{0.933}Ti_{0.067}O$ /glass	5.4	1.87	0.0087

[a] CN, *R* (Å), and σ^2 (Å^2) are the coordination number, inter-atomic distance, and Debye-Waller factor, respectively. The uncertainties for CN, R, and σ^2 are 10%, 0.01 Å, and 10%, respectively.

In the Ti K-edge EXAFS functions of $Zn_{0.972}Ti_{0.028}O$ and $Zn_{0.933}Ti_{0.067}O$ displayed in Fig. 5.17, the first peak at around 1.4~ 1.5Å

(phase shift was not corrected) is due to the Ti-O or Zn-O coordinations in the first shell. The second peak at about 3.15~3.2Å corresponds to the second shell, e.g. Ti-12Zn for doped ZnO or Zn-12Zn for ZnO. Due to the lattice distortion caused by the doping, a shift towards higher *R* of the second Ti-Zn shell is observed for doped samples relative to ZnO. This is attributed to the more closely packed Ti-O shells, causing Ti to be more loosely bonded to the second shell. The third peak at approximately 4.05Å arises mainly from the third coordination shell comprising 9 O atoms and multiple scattering paths, which are not obvious due to the lack of long range ordering in the film samples.

The fit to the Ti-O coordination yields a R_{Ti-O} of 1.89Å for $Zn_{0.972}Ti_{0.028}O$. It is much smaller than R_{Zn-O} (1.97Å) in ZnO, in agreement with the theoretical calculations in reference [22] and this might be due to the stronger interaction between tetra Ti^{3+} and O^{2-} as compared to Zn^{2+} and O^{2-}. The empty d-orbitals of Ti may be involved in the bonding. The CN of the Ti-O shell for $Zn_{0.972}Ti_{0.028}O$ is close to 4 if the 10% error was taken into account. This implies that the majority of the Ti^{3+} ions have substituted the Zn^{2+} ions in ZnO. However, a distortion was also induced. The solubility limit of Ti in ZnO at the equilibrium state is about 2.5~4.0%.[16]

A broadening and the shift toward low R of the Ti-O peak for $Zn_{0.933}Ti_{0.067}O$ are observed. The fit to the Ti-O coordination yields a R_{Ti-O} of 1.87Å which is also smaller than that of ZnO. The CN of the Ti-O shell for $Zn_{0.933}Ti_{0.067}O$ is 5.3 which implies that a portion of Ti ions are more likely to take octahedral coordination than tetrahedral one. Hence, the FT fitted results are consistent with the formation of zinc titanate compounds such as $Zn_2Ti_3O_8$ and $ZnTiO_3$. These compounds might have shorter Ti-O bond lengths. $Zn_2Ti_3O_8$ is a metastable compound and possesses a defect spinel structure.[26] The Ti^{4+} ions in $Zn_2Ti_3O_8$ occupy octahedral sites whereas part of Zn^{2+} ions occupy octahedral sites and the rest are in tetrahedral sites. $ZnTiO_3$ has

a perovskite structure and is stabilized by the 6-fold coordination of the Ti^{4+} ions and 12-fold coordination of the Zn^{2+} ions. The Ti^{4+} ion is located at the octahedral interstitial site at the center of the unit cell and is coordinated to six O^{2-} ions. This accounts for the increase in CN and a decrease in R of the Ti-O shell for $Zn_{0.933}Ti_{0.067}O$. However, this is not very evident based on the XANES results.

It can be concluded that the percolation threshold of Ti in ZnO cannot exceed 6.7% even though reactive magnetron sputtering is a non-equilibrium film growth process. XAFS results also indicated that the majority of Ti^{3+} ions have been incorporated into the substitutional sites of the Zn lattice at about and below 2.8% Ti doping content; the results also revealed predominant tetrahedral coordination geometry of Ti atoms in $Zn_{1-x}Ti_xO$. The ZnO lattice is distorted with Ti doping, demonostrated by the fact that Zn-O has a stronger interaction than ZnO. Titanium oxides are formed when the films are fabricated in the ambient containing 20% oxygen and zinc titanate compounds are generated at approximately 6.7% Ti doping content.

5.2.4 Mn-doped ZnO

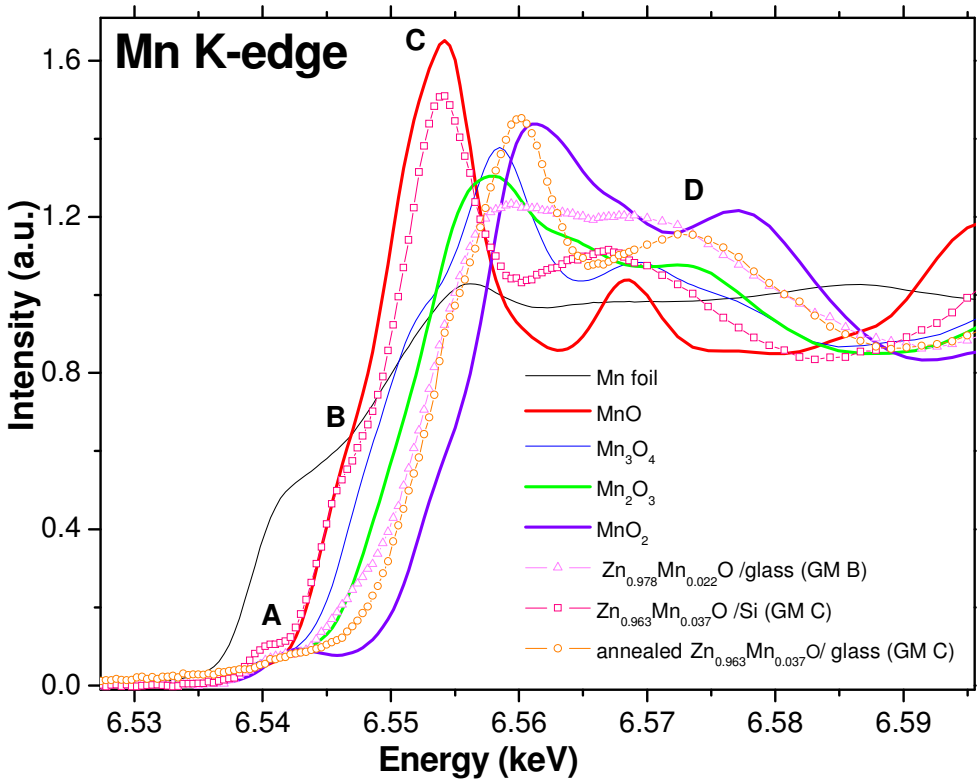

Fig. 5.19. Normalized Mn K-edge XANES of $Zn_{0.978}Mn_{0.022}O$ and $Zn_{0.963}Mn_{0.037}O$ films deposited on glass, annealed $Zn_{0.963}Mn_{0.037}O$ film deposited on Si(100), Mn foil, MnO, Mn_3O_4, Mn_2O_3 and MnO_2. GM B and GM C stand for 80%Ar + 20%O_2 and Ar gas mixture, respectively.

Fig. 5.19 compares the normalized Mn K-edge XANES spectra of $Zn_{0.978}Mn_{0.022}O$ and $Zn_{0.963}Mn_{0.037}O$ films deposited on glass and annealed $Zn_{0.963}Mn_{0.037}O$ film deposited on Si(100) with those of pure Mn foil, MnO, Mn_3O_4, Mn_2O_3 and MnO_2. The XANES spectrum for $Zn_{0.999}Mn_{0.001}O$ was not presented because of the poor data quality due to the low Mn concentration. Similar to previous data, the spectra in Fig. 5.19 shows a small pre-edge peak A, a shoulder peak B, a dominant main peak C and a shoulder D at the post-edge region. The interpretations of K-edge XANES features for 3d TM oxides have been explained in sections 5.2.1 and 5.2.2.

$Zn_{0.978}Mn_{0.022}O$ fabricated under 80%Ar + 20%O_2 atmosphere shows a positive chemical shift relative to $Zn_{0.963}Mn_{0.037}O$. The shift of the peak A to higher energy implies the change of valence state of Mn to a higher oxidation state between 3+ and 4+, as the final spectrum lies in between those of Mn_2O_3 and MnO_2. Reduced and broadened intensities for A, C, and D are observed. Although the Mn doping concentration is extremely low in this sample, a small portion of maganese oxides in $Zn_{0.978}Mn_{0.022}O$ might already have formed during the sputtering process. As indicated by the XRD results in section 4.4.4, $Zn_2Mn_3O_8$ is the probable precipitated phase. Mn might have reacted with the O_2 gas in the chamber during deposition.

$Zn_{0.963}Mn_{0.037}O$ was fabricated under pure Ar ambient. A comparison with MnO in terms of chemical shift indicates a 2+ valence for Mn, which is in agreement with previous reports.[12,27-29] Furthermore, the solubility limit of Mn in ZnO at equilibrium state is about 19.0~21.0%.[16] The spectrum of this sample shows a distinct pre-edge peak A which indicates a four-fold coordination of Mn, consistent with previous publications.[27,28,30-32] This suggests a substitutional incorporation of Mn^{2+} ions into the Zn sites.

$Zn_{0.963}Mn_{0.037}O$ films deposited on Si(100) and glass slide are grown under the same conditions. The film deposited on Si is annealed at 800^{o}C; details are given in section 4.5. There is a positive shift in energy of the annealed $Zn_{0.963}Mn_{0.037}O$ spectrum relative to the as-deposited one. The intensity of peak A decreases and it shifts to higher energy, this indicates that the valence state of Mn changes to a higher oxidation state and is between 3 and 4 as the final spectrum lies in between those of Mn_2O_3 and MnO_2. After the sample was heated at 800^{o}C for an hour in air, some Mn^{2+} ions might have aggregated and formed manganese oxides with higher valence states near the surface.

Fig. 5.20 illustrates the Mn K-edge EXAFS functions of Mn-doped ZnO films and reference samples by extracting the oscillation part from

the free atomic absorption background. The EXAFS of $Zn_{0.978}Mn_{0.022}O$ and annealed $Zn_{0.963}Mn_{0.037}O$ are drastically different from that of $Zn_{0.963}Mn_{0.037}O$, indicative of different structures in the films.

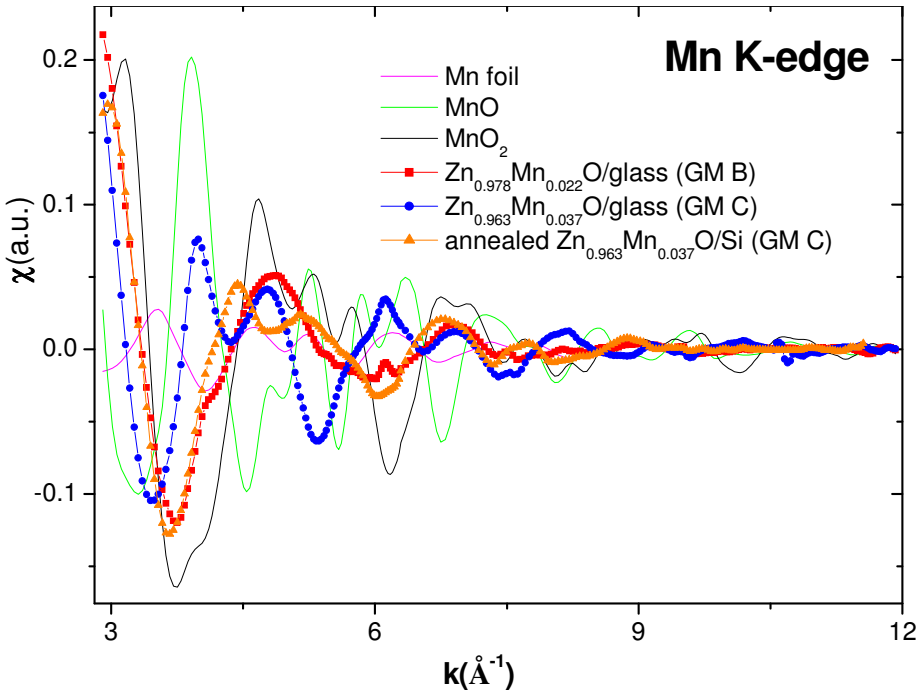

Fig. 5.20. Mn K-edge EXAFS function of Mn-doped ZnO films deposited on glass and reference samples. GM B and GM C stand for 80%Ar + 20%O_2 and Ar gas mixture, respectively.

The Fourier transform (FT) magnitudes of the Mn-doped ZnO films and reference samples are shown in Fig. 5.21. Fig. 5.22 illustrates the two-shell data fit in $Zn_{0.978}Mn_{0.022}O$ and $Zn_{0.963}Mn_{0.037}O$ films deposited on glass and the one-shell data fit for $Zn_{0.963}Mn_{0.037}O$ film deposited on Si; the fitting results are tabulated in Table 5.5. Table 5.5 also lists the radial structural parameters of the first and second coordination shells for the reference samples used in the study which are extracted from crystallographic data of these oxides. In the FT, the XAFS function in the range 2.7-12.0$Å^{-1}$ in *k* space wwas extracted for Mn K-edge. The CN, interatomic distance (R), DW factor and the energy shift (E_0) were

set as free variables during the fit. The inelastic factor, s_0, was extracted from a fit to the reference sample and was fixed at 0.90 in the fit.

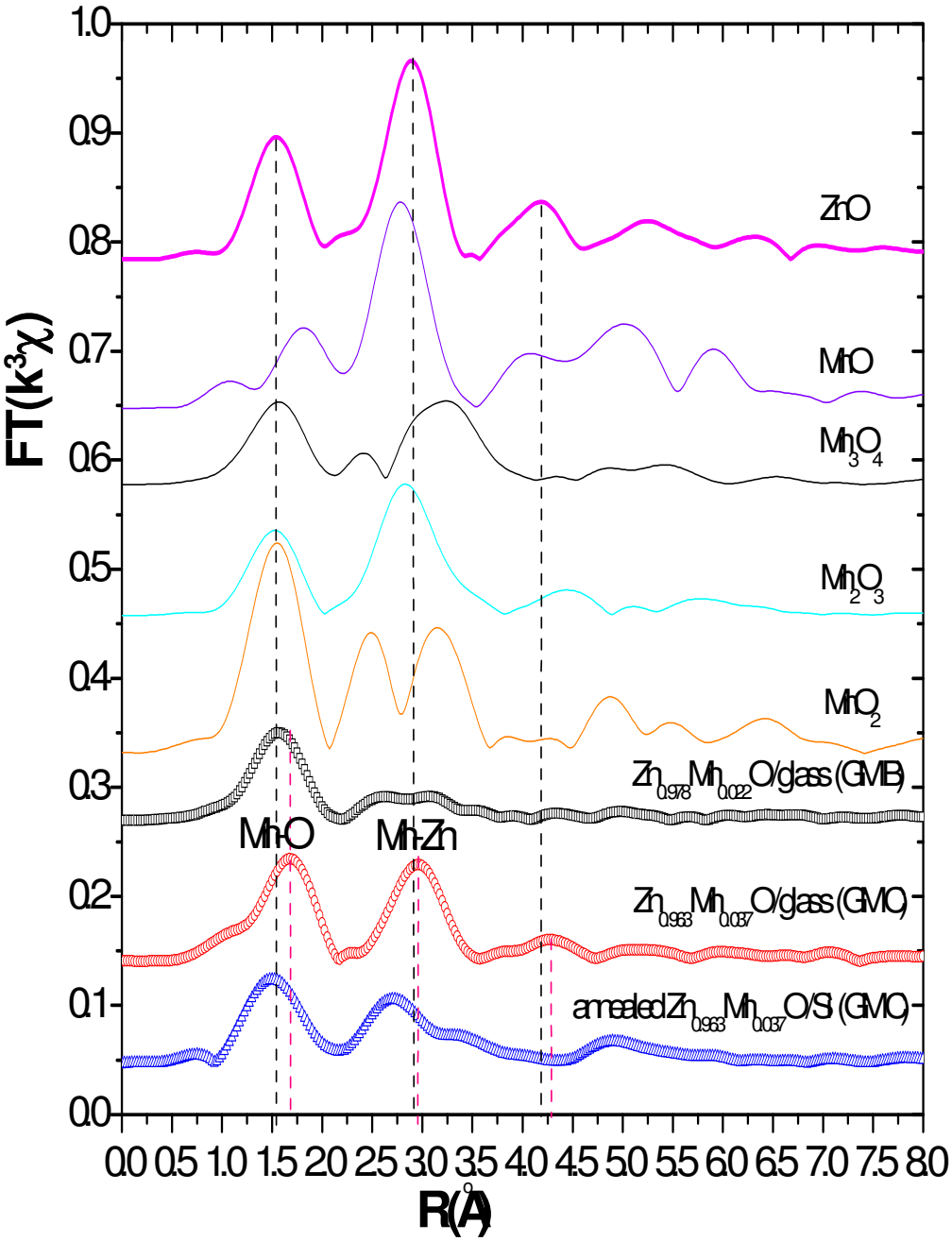

Fig. 5.21. Fourier Transform magnitudes of the Mn K-edge EXAFS function of Mn-doped ZnO films deposited on glass and reference samples. GM B and GM C stand for 80%Ar + 20%O_2 and Ar gas mixture, respectively.

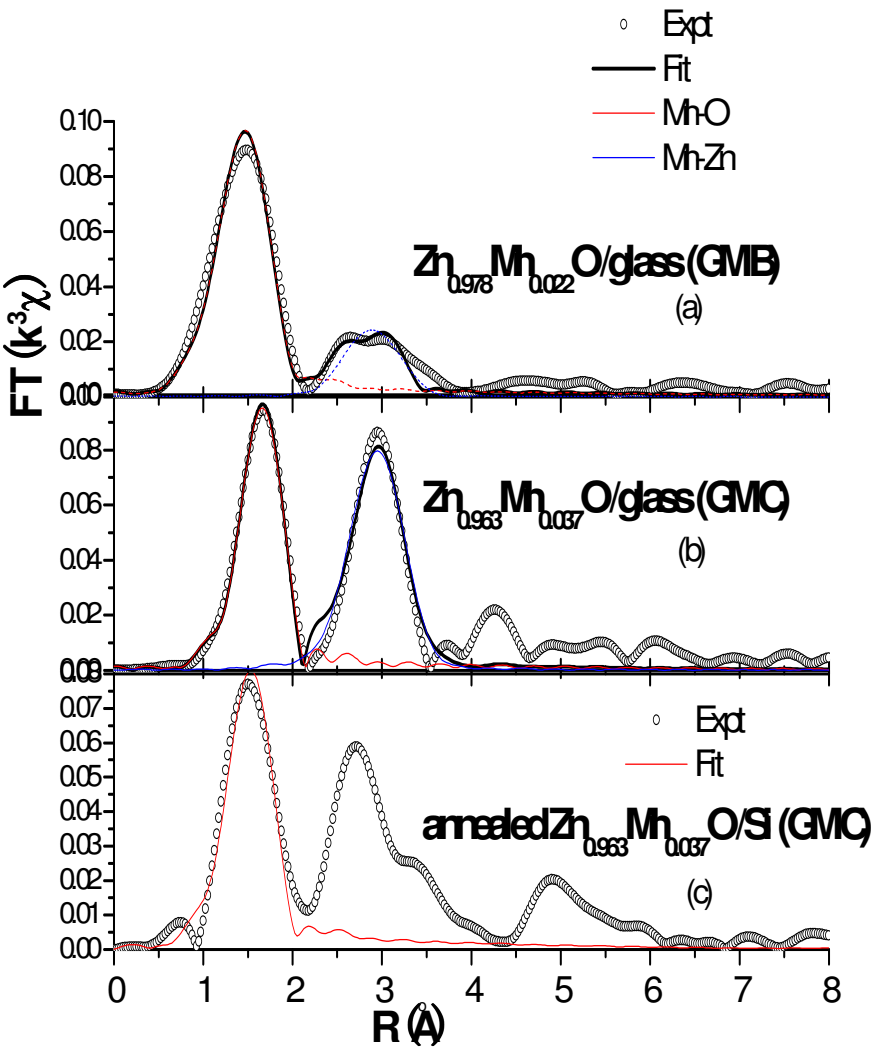

Fig. 5.22. Two shell data fit (Zn-O and Zn-Zn respectively) to the FT of the (a) $Zn_{0.978}Mn_{0.022}O$ film deposited on glass, (b) $Zn_{0.963}Mn_{0.037}O$ film deposited on glass and one shell-fit data (Zn-O) to the (c) annealed $Zn_{0.963}Mn_{0.037}O$ film deposited on Si (100) at the Mn K-edges. GM B and GM C stand for 80%Ar + 20%O_2 and Ar gas mixture, respectively.

Table. 5.5. Fitting results of the Mn-O and Mn-Zn shells in $Zn_{0.978}Mn_{0.022}O$ and $Zn_{0.963}Mn_{0.037}O$ films.[a]

Mn K-edge	Mn-O/ Zn-O			Mn-Zn /Zn-Zn /Mn-Mn		
	CN	R	σ^2	CN	R	σ^2
ZnO	4.0	1.97	--	12.0	3.21	--
MnO	6.0	2.22	--	12.0	3.14	--
Mn_3O_4	4.0/ 6.0	2.04	--	8.0	3.43	--
Mn_2O_3	6.0	1.99	--	6.0	3.10	--
Mn_5O_8	6.0	1.89	--	6.0	2.94	--
MnO_2	6.0	1.89	--	2.0	2.87	--
$Zn_{0.978}Mn_{0.022}O$ /glass	6.5	1.89	0.0116	2.3	3.24	0.0093
$Zn_{0.963}Mn_{0.037}O$ /glass	3.5	2.04	0.0033	10.5	3.25	0.0130
$Zn_{0.963}Mn_{0.037}O$ /Si, annealed	3.4	1.91	0.0060			

[a] CN, *R* (Å), and σ^2 ($Å^2$) are the coordination number, inter-atomic distance, and Debye-Waller factor, respectively. The uncertainties for CN, R, and σ^2 are 10%, 0.02 Å, and 10%, respectively.

As shown in Fig. 5.21, the first peak is due to the nearest neighbor four Co-O or Zn-O bonds in the first shell. The second peak corresponds to the second shell of mainly twelve Co-Zn or Zn-Zn bonds (for ZnO) and the third peak arises mainly from the third coordination shell comprising 9 O atoms. The third coordination peaks of the as-prepared thin films are almost smeared out due to long range disorder in the samples.

In Fig. 5.21, the position of the first Mn-O peak does not change significantly for $Zn_{0.978}Mn_{0.022}O$ relative to the Zn-O peak. However, the fitted R_{Mn-O} is 1.89Å, much smaller than R_{Zn-O} and close to the theoretical value of MnO_2. The short R_{Mn-O} indicates that the Mn^{2+} ions are not isolated in the ZnO wurtzite lattice. They aggregate in the lattice,

and some of them convert from the wurtzite to Mn oxides with oxidization states between 3+ and 4+, with local structures similar to MnO_2 and $Zn_2Mn_3O_8$. It should be added that the R_{Mn-O} in manganese oxides is related to the valence states of Mn, the shorter R_{Mn-O} for $Zn_{0.978}Mn_{0.022}O$ is correlated with a higher valence state which is consistent with the XANES analysis. The much dampened second Mn-Zn or Mn-Mn peak and the third coordination peak in the FT are an indication that the precipitated tetravalent manganese oxides found in $Zn_{0.978}Mn_{0.022}O$ lack long range order. In addition, the CN of the first Mn-O shell for these samples is about 6, within experimental error, hence the majority of the Mn ions has precipitated and formed MnO_2 and $Zn_2Mn_3O_8$ clusters, consistent with XANES and XRD results.

In Fig. 5.21, the first Mn-O or Zn-O peak of $Zn_{0.963}Mn_{0.037}O$ deposited on glass shifts to the right relative to the Zn-O peak and is centered at about 1.9Å. R_{Mn-O} is 2.04Å, close to the values reported by Tao et al.[21] and J. Pellicer-Porres et al.[30]. The larger value of R_{Mn-O} (2.04Å) than those of ZnO (1.97Å) and Co-doped ZnO may be due to the larger Mn^{2+} ionic radius (0.66 Å) as compared to those of Zn^{2+} (0.60Å) and Co^{2+} (0.58Å). This indicates an overall expansion of the ZnO lattice as a result of doping with larger Mn^{2+} ions. The R_{Mn-Zn} value is 3.25Å, close to the value of Mn-doped ZnO nanoparticles calcinated at 400^{o}C reported by Tao et al.[21]. In addition, the CN of the first Mn-O shell for this sample does not exceed 4, indicating that the majority of the Mn^{2+} ions have been incorporated into the substitutional sites of the Zn lattice and have predominantly tetrahedral coordination in the first shell even though a distortion is induced by the substitution.

The broadening of the Mn-O and Mn-Zn peaks in the Mn K-edge FT displayed in Fig. 5.21 is observed for annealed $Zn_{0.963}Mn_{0.037}O$ deposited on Si. The shape and position of the FT resembles that of Mn_2O_3. There is an overall left shift of the spectrum to smaller R relative to the as-prepared sample. R_{Mn-O} (1.91Å) decreases relative to

that of the as-prepared sample. The CN of the first Mn-O shell for this sample, on the other hand, is smaller than 4, suggesting that the sample also contains a portion of MnO_2 and Mn_5O_8 ($Mn_2^{2+}Mn_3^{4+}O_8$)[33] which have Mn-O bond lengths of 1.89Å. Mn_5O_8 is a metastable compound.[34] At 800°C, this metastable substituted doping state of Mn in ZnO was replaced by manganese oxides with higher valence states, consistent with the XANES analysis.

It can be concluded that the majority of Mn^{2+} ions have been incorporated into the substitutional sites of the Zn lattice for low Mn doping content and they substitute the Zn ions at tetrahedral sites. There is also an overall expansion of the ZnO lattice as a result of doping of larger Mn^{2+} ions. Mn oxides with higher oxidization state are formed when the ambient in which the films are fabricated consists of 20% oxygen gas. When the Mn-doped ZnO sample is annealed at 800°C, Mn_2O_3 clusters and ZnMnO complex containing Mn^{3+} and Mn^{4+} are generated.

5.2.5 Discussions

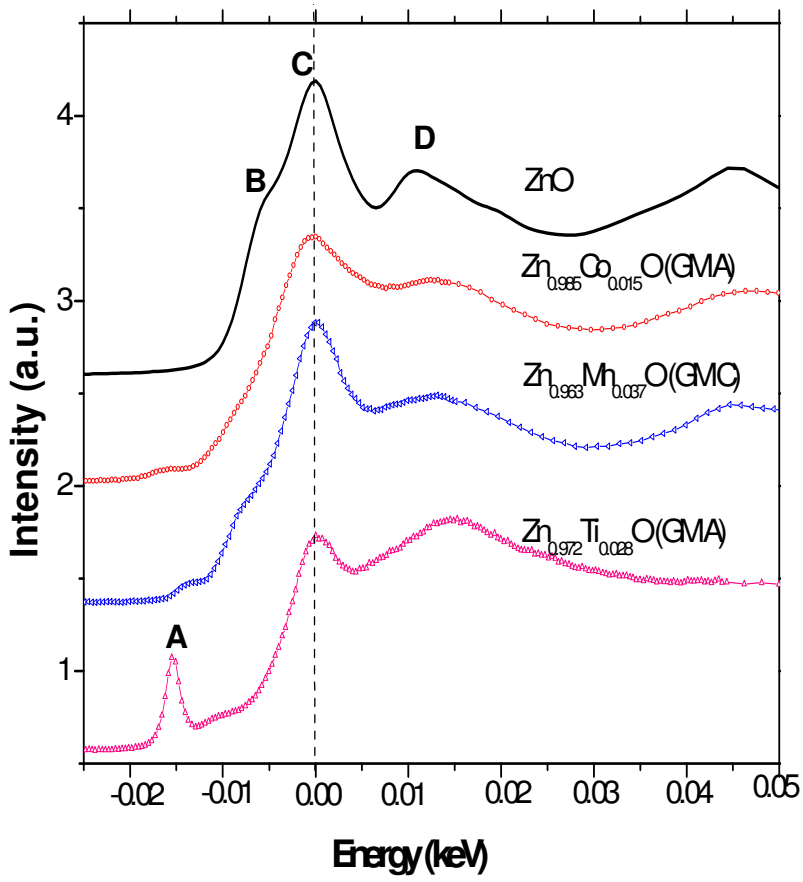

Fig. 5.23. Normalized K-edge fluorescent XANES for TM-doped ZnO (TM=Co, Mn and Ti) films deposited on glass and ZnO measured in fluorescence mode. Each spectrum was energy shifted relative to each other for co-plotting. GM A and GM C stand for 85%Ar + 15%N_2 Ar gas mixture, respectively.

Fig. 5.23 illustrates the normalized K-edge fluorescent XANES for TM-doped ZnO (TM=Co, Mn and Ti) films deposited on glass and ZnO measured in fluorescence mode. For comparison, the spectra were rescaled by taking the K edge energy of pure metals as the origin. The most pronounced pre-edge peak A is observed for the Ti-substituted ZnO and it reduces from Ti to Zn across the 3d transition metals series, indicating that the peak A is closely associated with the occupation of

3d-orbitals of TM as the electronic configuration from Ti to Cu varies from $3d^2$ to $3d^{10}$. The valence states of TM doped ZnO are related to the chemical shift of XANES and can be measured by comparison with reference samples. Ti incorporated in ZnO shows a 3+ valence state while those of Co and Mn are 2+.

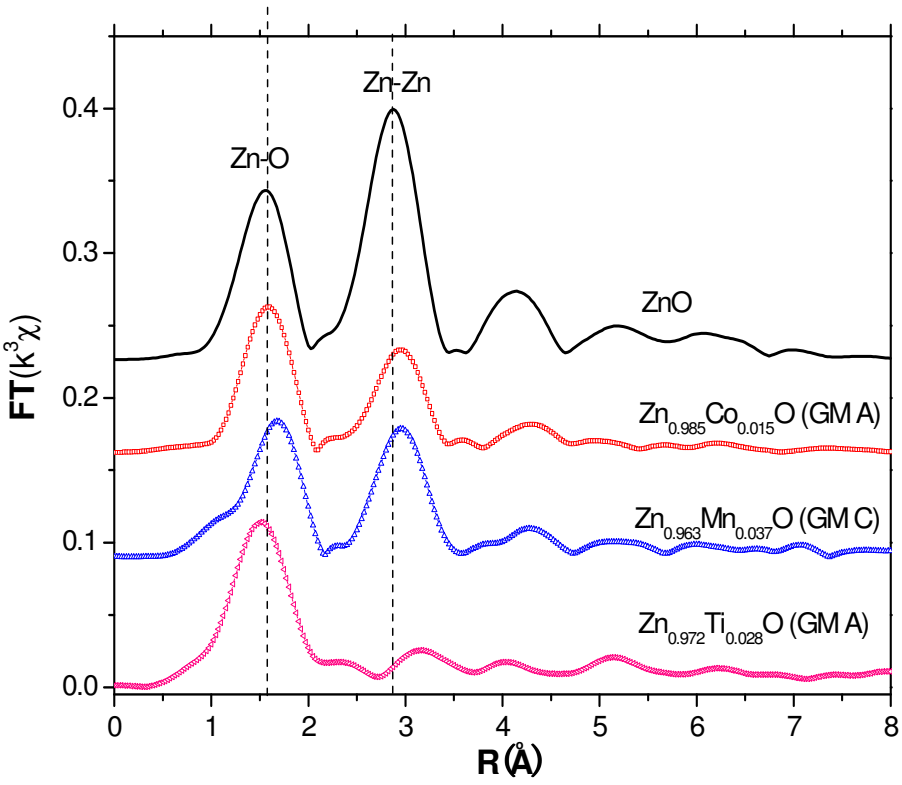

Fig. 5.24. Fourier Transform magnitudes of the TM-doped ZnO (TM=Co, Mn and Ti) films deposited on glass and ZnO. (GM A and GM C stand for 85%Ar + 15%N_2 Ar gas mixture, respectively.)

XAFS results show that the majority of the TM ions adopt a tetrahedral coordination in the ZnO matrix. The Fourier transformed spectra of Co, Ti and Mn-doped ZnO normally shows a well-ordered coordination up to the third shell[35,36] displayed in Fig 5.24. However, Co dopant in ZnO matrix results in less distortion of the ZnO lattice (in terms of $R_{Zn\text{-}O}$) as compared to Ti, Mn and Cu dopants. The ionic radius

matching with the ZnO lattice may be the main factor since this induces less strain energy.[21] In the case of Cu, though Cu^{+} has the same Shannon ionic radius as Zn^{2+} (0.6 Å), EXAFS results in section 5.2.2 have proven the precipitation of Cu_2O and Cu clusters in all Cu-doped samples; hence this might result in distortion of lattice since the clusters might be amorphous. Also, a slightly smaller radius might be more favorable for achieving high thermal stability of the dopant in ZnO, as in the case of Co^{2+} (0.58 Å).[21]

On the other hand, the charge transfer from ZnO to TM 3d orbitals also appears to be an important consideration.[21] The tendency of charge transfer arises from the excess electrons in impurity bands which are initially due to its strong n-type semiconductor character.[21] Such a charge transfer trend observed is compatible with the BMP model mentioned in Chapter 1.3.1. In this model, to achieve a high Curie temperature, hybridization and charge transfer from a donor-derived impurity band to unoccupied 3d states of the TM element is required.[21] The stable doping for Co but not for Mn, Cu and Ti, is indicative of the importance of ionic radius matching with matrix in ZnO doping, in order to reduce the free energy. The origin of the extra electrons for this charge transfer is probably impurity bands which are intrinsic for n-type ZnO[21] and needs further confirmation.

References

1. P. Yang, D. Lu, R. Kumar and H.O. Moser, Nucl. Instr. and Meth. in Phys. Res. B **238,** 310 (2005).
2. SPring-8 official website: http://www.spring8.or.jp/en/
3. SPring-8 official website, BL01B1 beamline details: http://www.spring8.or.jp/en/users/current_user/bl/beamline/BLsearch/instrument_list?q=BEQA
4. Isao Tanaka, Teruyasu Mizoguchi, Masafumi Matsui, Satoru Yoshioka, Hirohiko Adachi, Tomoyuki Yamamoto, nature materials, **2**, 541 (2003).
5. Tao Liu, Hairuo Xu, Wee Shong Chin, Zhihua Yong, and Andrew T. S. Wee, J. Phys. Chem C, **112**, 3489 (2008)

6. Fernandez-Garcia, M. Martinez-Arias, A, Hanson, J. C, Rodriguez, J. A. Chem. Rev, **104**, 4063 (2004).
7. Frank de Groot, Chem. Rev, **101**, 1779 (2001).
8. Z. Y. Wu, G. Ouvrard, P. Gressier, and C. R. Natoli, Phys. Rev. B, **55**, 10382 (1997).
9. Z. Y. Wu, S. Gota, F. Jollet, M. Pollak, M. Gautier-Soyer, and C. R. Natoli, Phys. Rev. B, **55**, 2570 (1997).
10. Ah Reum Han, Seong-Ju Hwang, Yongnan Zhao,Young-Uk Kwon, J. Magn. Magn. Mater., **320**,1591 (2008).
11. C.Song, K.W.Geng,F.Zeng,X.B.Wang, Y.X. Shen and F. Pan, Phys. Rev. B, **73**, 024405 (2006)
12. S.S Lee, G. Kim, S.C Wi. J.-S. Kang, S.W.Han,Y.K.Lee, K.-S.An, J. Appl. Phys., **99**, 08M103 (2006).
13. G. Peleckis, X. L. Wang, R. S. Liu, and S. X. Dou, IEEE Transactions on Magnetics, **41**, 2727 (2005).
14. E. Biegger, M. Fonin, U. Rüdiger, N. Janßen, M. Beyer, T. Thomay, and R. Bratschitsch, Yu. S. Dedkov, J. Appl. Phys., **101**, 073904 (2007).
15. S.C. Wi, J,-S. Kang, J. H. Kim, S,-B. Cho, B. J. Kim, S. Yoon, B. J. Suh, S.W. Han, K. H. Kim, Appl. Phys. Lett., **84**, 4233 (2004).
16. C. Liu, F. Yun and H. Morkoc, J. Mater. Sci. in electronics, **16**, 555 (2005).
17. Lin X. Chen, Tao Liu, Marion C. Thurnauer, Roseann Csencsits, Tijanaand Rahj, J. Chem. Phys. B **106**, 8539 (2002).
18. P. Fons, A. Yamada, K. Iwata, K. Matsubara, S. Niki, K. Nakahara, and H. Takasu, Nucl. Instru. Meth. B, **199**, 190 (2003).
19. Nicola A. Spaldin, Phys. Rev. B, **69**, 125201 (2004).
20. Xiaobing Feng, J. Phys.: Condens. Matter, **16,** 4251 (2004).
21. Tao Liu, Hairuo Xu, Wee Shong Chin, Ping Yang, Zhihua Yong, Andrew T. S. Wee, to be published.
22. Zhi-hua Xiong, Feng-yi Jiang, J. Phy. And Chem. of Solids, **68**, 1500 (2007).
23. K. Osuch, E.B. Lombardi and W. Gebicki, Physical Rev. B, 73, 075202 (2006).
24. M. Venkatesan, C. B. Fitzgerald, J.G. Lunney, and J.M. D. Coey, Phys. Rev. Lett., **93**, 177206 (2004).
25. U. Steinikeb, B. Wallis, Cyst. Res. Technol., **32**, 187 (1997).
26. D. H. Hill, D. A. Arena, R. A. Bartynski, P. Wu, G. Saraf, Y. Lu, L. Wielunski, R. Gateau, J. Dvorak, A. Moodenbaugh, and Yung Kee Yeo, Phys. Stat. Sol. (a), **203**, 3836 (2006).
27. Young Joo Kang, Dae Sung Kim, Sang Hyun Lee, and Jeunghee Park, Joonyeon Chang, Je Yong Moon and Gangho Lee, J. Phys. Chem. C, **111**, 14956 (2007).
28. Wen Chen, Jing Wang, Min-rui Wang, Vacuum, **81**, 894 (2007).
29. J. Pellicer-Porres, A. Segura, J.F. S´anchez-Royo, J.A. Sans, J.P. Iti´e, A.M. Flank, P. Lagarde, A. Polian, Superlattices and Microstructures, **42,** 251 (2007).

30. M.H. Kane, K. Shalini, C.J. Summers, R. Varatharajan, J. Nause, C.R. Vestal, Z.J. Zhang, I.T. Ferguson, J. Appl. Phys., **97**, 023906 (2005).
31. Teng Xiao-yun, Yu Wei, Yang Li-hua, Hao Qiu-yan, Zhang Li, Xu He-jun, Liu Cai-chi, Fu Guang-Sheng, Chin Phys. Lett., **24**, 1073 (2007).
32. Punnoose. A., Magnone. H., Seehra. M.S, IEEE Transactions on Magnetics, **37**, 2150 (2001).
33. S. Fritsch, J. Sarrias, A. Rousset and G.U. Kulkarni, Materials Research Bulletin, 33, 1185 (1998).
34. G. Martinez-Cariado, A. Segura, J. A. Sans, Appl. Phys. Lett., **89**, 061906 (2006).
35. H. Ofuchi, Z. W. Jin and T. Fukumura, Phys. Scripta, **T115**, 614 (2005).

Chapter 6

Magnetic Properties of 3d doped ZnO thin films

Vibrating sample magnetometer (VSM) was used to measure the hysteresis loops for all TM-doped ZnO films deposited on Si(100) substrates at room temperature. The saturation moments (M_s) of all samples were discussed and the possible origins of ferromagnetism (FM) were suggested.

6.1 Experimental procedure

A model 7407 VSM produced by Lake-Shore Company was used in the magnetic measurements of the thin films. The magnetic field was applied parallel to the plane of the sample. Before the measurements, the sample holder with a pure Si substrate bonded by white Teflon tape was first measured to calibrate the background madnetism contributed by the holder, Teflon tape and Si substrate. The thin film samples with dimensions (~10mm x 7mm) were used for magnetic measurements. A maximum of 5000G magnetic field was applied to the sample during measurements. There were a total of 72 points collected in the hysteresis loops and the y-sensitivity was set to be 400emu. The time lag at each point was approximately 20s. The magnetization curves were measured at room temperature.

6.2 Data Analysis

The saturation magnetic moments M_s per TM atom and per cm^3 were calculated. Before performing these calculations, the mass of the measured samples and pure Si substrate was measured using an electronic beam balance. Since the mass **X** of all the samples are different, it is crucial to normalize the magnetic measurements to 1g sample mass before making

comparisons. Assuming that the mass of thin films was negligible compared to the Si substrates, the magnetization curves were first divided by the mass of the respective samples. The same procedure is applied to the magnetic measurement performed on pure Si substrate for calibration. The calibration curve is then subtracted from the magnetization curves of all the samples; hence the hysteresis loops **R** obtained are due solely to the thin films since all the background and substrate effects were eliminated. **R** is then readjusted, so that its center lies in the center of the intersection of the x-y axes.

Next, the lengths and widths of the samples were measured using a vernier caliper several times and average values are taken. The surface areas **A** of the rectangular films were calculated. However, **A** is the surface area of the film for mass **X**; when the mass of the sample is increased to 1g, we are assuming a bigger piece of Si substrate and a larger surface area of the Si substrate. Hence, the area of the deposited film will also increase. The larger surface area **B** of the film for 1g of the sample is calculated by proportionality calculations. The thickness **T** of the films remained a constant regardless of the size of Si substrate. **T** had already been measured using the alpha-step profilometer and the results are tabulated in section 3.2. The volume ($\mathbf{V = B \times T}$) of the thin films were then calculated from these results, followed by the multiplication of the density of ZnO ($5.65 g/cm^3$) with **V** to obtain the mass (**m)** of the film for 1g of the sample. Next, the hysteresis loops **R** is divided by **m** of the respective films to obtain resultant curves **P/** emu per g. M_s per g for all thin films can then be found from **P**. The error in M_s can be calculated by means of standard deviation.

The concentrations of TM in $Zn_{1-x}TM_xO$ had been calculated in section 3.3. Next, the number of TM atoms in $Zn_{1-x}TM_xO$ was calculated using the following equation:

$$\begin{aligned}\#\text{ TM atoms} &= \#\text{moles of ZnO} \times \text{Avogadro constant} \times \%\text{TM concentration} \\ &= \text{mass } \mathbf{m} \text{ of film/ mass of 1 mole of } Zn_{1-x}TM_xO \\ &\quad \times \text{Avogadro constant} \times \%\text{TM concentration}\end{aligned}$$

where Avogadro constant=$6.02\times10^{23} mol^{-1}$

Finally, the magnetization curves **R** are divided by the respective number of TM atoms and a conversion from emu to μ_B is done to obtain the hysteresis loops **H/** μ_B per TM atom. M_s per TM atom for all thin films are measured from **H**. The error in M_s can be calculated by means of standard deviation.

6.3 Results and Discussions

6.3.1 Co-doped ZnO

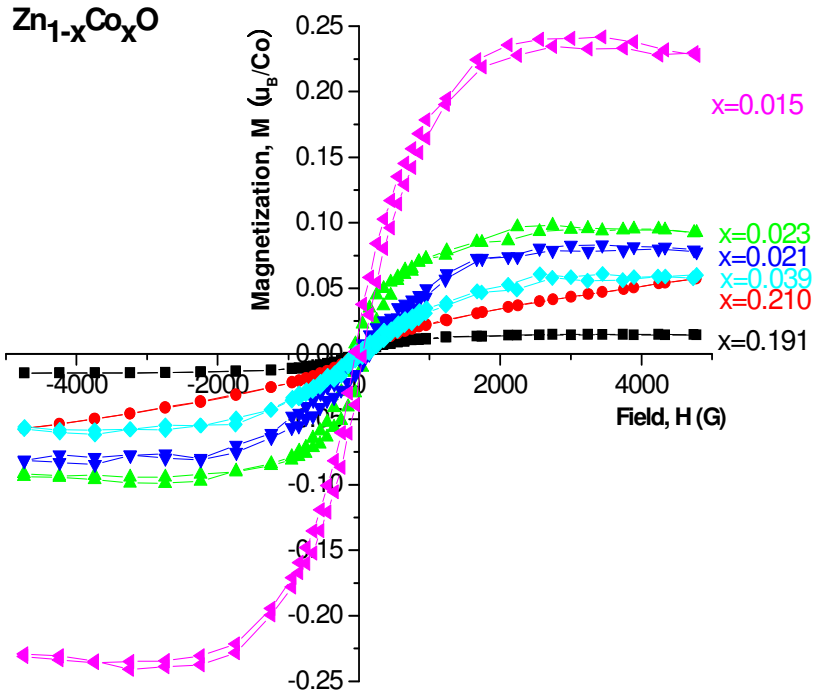

Fig. 6.1. M-H loops measured at room temperature for Co-doped ZnO films deposited on Si (100).

The M-H magnetization (μ_B/Co) curves measured at room temperature are shown in Fig. 6.1. All Co-doped ZnO films are ferromagnetic except for $Zn_{0.790}Co_{0.210}O$ which shows no distinct hysteresis in Fig. 6.1. The hysteresis loop for $Zn_{0.809}Co_{0.191}O$ is very low in magnitude. The insulating nature of our Co-doped ZnO samples is significant in that a magnetic coupling interaction other than carrier-mediated exchange is apparently operative. Moreover, conventional superexchange interactions cannot produce long-range magnetic order at concentrations of magnetic cations of

a few percent.[1] Therefore, there are two possible origins of the ferromagnetism in Co-doped ZnO that should be considered.

The first possible origin of FM of insulating Co-doped ZnO samples might be derived from common native defects such as oxygen vacancies, zinc intersitials and zinc vacancies.[2] The oxygen vacancies might have an important role in the origin of room-temperature ferromagnetism for insulating oxide DMS. [3-6] This is because the likely origin of the donor impurity band in ZnO films come from lattice defects such as oxygen vacancies which trap between one and two electrons (F^0centers).[7-10] The spin-split impurity-band model which is accountable for FM has been elaborated in section 1.3.2. M. Venkatesan et al.[7] reported that there is no obvious correlation between conductivity and cation valence or conductivity and magnetism in their TM-doped ZnO samples. The electrons in the impurity band will be localized by the influence of electronic correlations and potential fluctuations[11] associated with the dopant cations.[7] Localization does not preclude ferromagnetic coupling, providing the localization length is not much shorter than γa_0.[7]

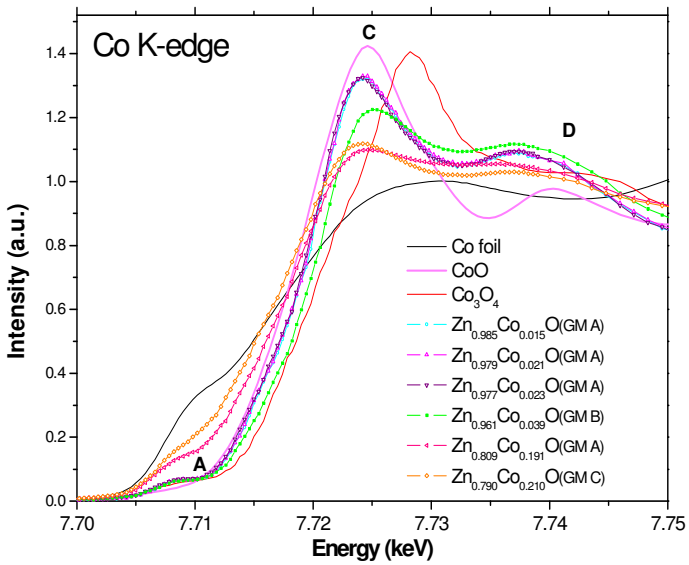

Fig. 6.2. Normalized Co K-edge XANES spectra of Co-doped ZnO films deposited on glass, Co foil, CoO and Co_3O_4. GM A, GM B and GM C stand for 85%Ar + 15%N_2, 80%Ar + 20%O_2 and Ar gas mixture, respectively.

Tongfei Shi et al.[4] has carried out XANES models simulations taking into account two structure models. One model is Co atom substituting for

Zn atom in ZnO cluster with the first shell, and the values obtained from their EXAFS fitting are attributed to second shell bond lengths. The other model is substitutional Co at Zn sites in ZnO with one oxygen vacancy in the nearest coordination shell.[4] In the experimental and calculated XANES spectra done using the FEFF8.2 code by Tongfei Shi et al.[4], it is observed that the two main features in the experimental spectra of $Zn_{0.98}Co_{0.02}O$ and $Zn_{0.95}Co_{0.05}O$ can be reproduced by the calculated spectrum for the structure model without oxygen vacancy.[4] However, the presence of an oxygen vacancy makes peaks A and B change to one smooth peak C. This indicates that oxygen vacancy, which can induce a donor state overlapping with the *d* states of the Co atoms, is not produced in these samples[4]. In contrast to their results, our EXAFS results (Fig. 6.2) in section 5.3.1 show that only a smooth peak "D" which corresponds to peak "C" in the calculated XANES spectra done by Tongfei Shi et al.[4], exists for $Zn_{0.985}Co_{0.015}O$, $Zn_{0.979}Co_{0.021}O$ and $Zn_{0.977}Co_{0.023}O$ whereby Co^{2+} ions are successfully incoporated at the Zn sites. Thus, our results indicate the presence of oxygen vacancies that might give rise to room temperature FM.

Marcel H.F. Sluiter et al.[6] , on the other hand, reported that the DFT calculations with oxygen vacancies in the case of Co and Mn revealed little effect on the magnetic couplings because the induced donor state is too deep to significantly affect the occupancy of the extended TM levels. This opposes the reasoning given by references [4], [5], [6] and [12]. Marcel H.F. Sluiter et al.[6] also reported that both electron doping with zinc interstitials and hole doping with zinc vacancies make $Zn_{1-x}Co_xO$ and $Zn_{1-x}Mn_xO$ strongly FM. The important role played by Zn vacancies and Zn interstitials explains why annealing at high temperatures decreases FM in $Zn_{1-x}Co_xO$ as the Zn vacancies and Zn interstitials are generally lost and replaced with inert oxygen vacancies. In our case, it is also possible that the FM found in the Co-doped ZnO films is due to the presence of the native defects such as zinc interstitials and zinc vacancies.

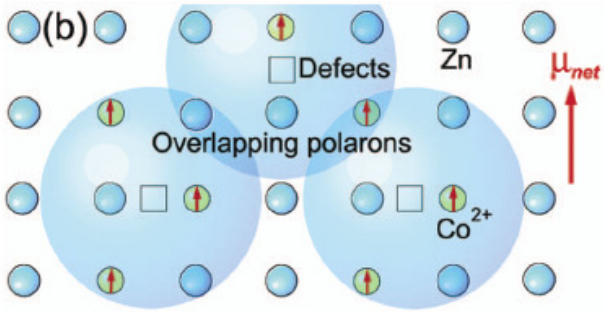

Fig. 6.3. Three-polaron subsystem is to represent supercoupling between polarons.[1]

The second possible origin of FM in our Co-doped ZnO samples can be attributed to intrinsic magnetism by invoking a supercoupling mechanism based on the bound magnetic polarons (BMP) model as mentioned in section 1.3.1.[1,3,13,14,15] The highly non-equilibrium process of magnetron sputtering makes it possible for impurities (defects) in the doped film to be located throughout the lattice at arbitrary distances with respect to Co sites.[4] For a sufficiently large orbital radius, overlap between a hydrogenic electron and the cations within its orbit leads to ferromagnetic supercoupling between them[1], as shown in Fig. 6.3. The interaction between the hydrogenic electron and the cations is represented by a Heisenberg exchange Hamiltonian:[1,16]

$$\hat{H}_{ij} = \Sigma_{ij} J_{ij} \hat{S}_i \hat{s}_j \qquad \text{--- (1)}$$

where S is the spin of the Co^{2+} and s is the donor electron spin. The donors tend to form a BMP, coupling Co^{2+} within their orbits. The Hamiltonian of a two-polaron subsystem is given by Eq. (1), where donor electron spin index j takes only two values j_1 and j_2 corresponding to the two polarons under consideration.[1]

Table. 6.1. The saturation magnetic moments M_s of Co-doped ZnO films deposited on Si (100) and the atmosphere under which they are fabricated.

Sample name	Atmosphere	M_s/μ_B per Co atom
$Zn_{0.985}Co_{0.015}O$	Ar + N_2	0.237 ± 0.004
$Zn_{0.979}Co_{0.021}O$	Ar + N_2	0.081 ± 0.002
$Zn_{0.977}Co_{0.023}O$	Ar + N_2	0.095 ± 0.0006
$Zn_{0.977}Co_{0.023}O$, annealed	Ar + N_2	0.037 ± 0.001
$Zn_{0.961}Co_{0.039}O$	Ar + O_2	0.058 ± 0.001
$Zn_{0.809}Co_{0.191}O$	Ar + N_2	0.015 ± 0.00003
$Zn_{0.790}Co_{0.210}O$	Ar	---

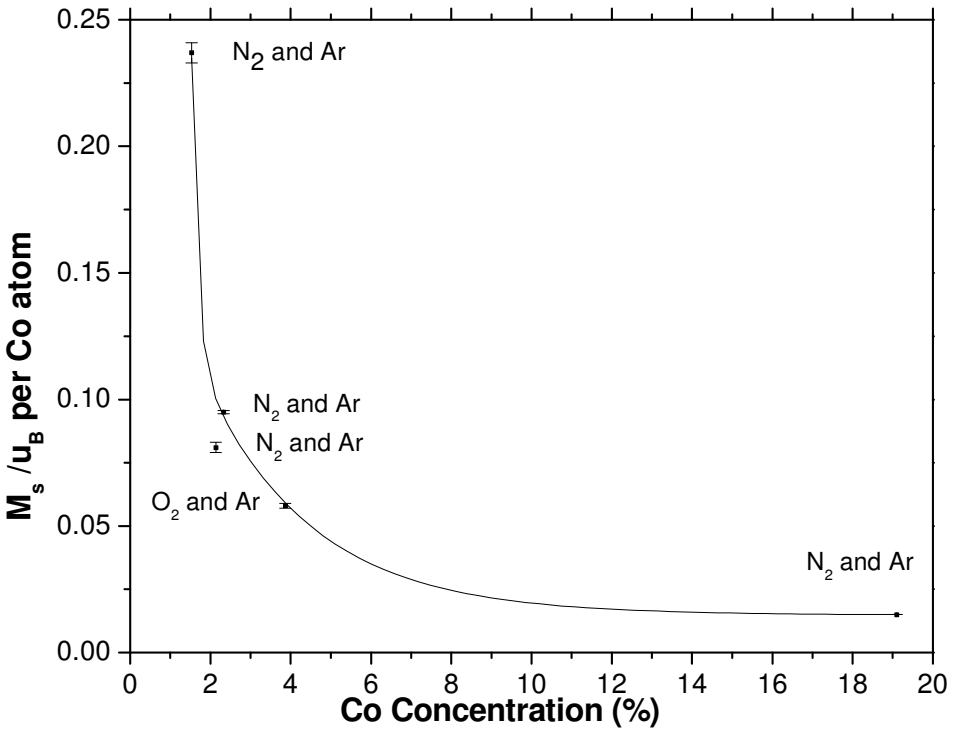

Fig. 6.4. The room temperature saturation magnetic moments M_s expressed as (μ_B/Co), as a function of the measured Co concentrations ***x*** of the Co-doped specimens. The Co concentration in the sample was estimated by XRF measurements.

Table 6.1 tabulates M_s (μ_B/Co) of Co-doped ZnO films deposited on Si (100). Fig. 6.4 displays the variation of M_s (μ_B/Co) with Co concentration ***x*** of the samples. The largest measured moment is 0.237±0.004 μ_B/Co in $Zn_{0.985}Co_{0.015}O$ is smaller than the spin-only moment $m_{spin}= 3\mu_B$ Co^{2+} in the high spin d^7 configuration $e^4t_2^3$.[7,12,17] Song et al.[1] reported a large saturation moment of 6.1 μ_B/Co atom at room temperature for 4 at.% Co-doped ZnO sample. Table 6.1 and Fig. 6.4 demonstrate a general trend of falloff in

$M_s(\mu_B/Co)$ with increasing $\boldsymbol{x}$, consistent with several publications.[1,3,18,19] This phenomenon can be explained by the four following reasons.

The first possible reason is in terms of a random distribution of cobalt ions over the cation sites in the wurtzite lattice. Isolated ions contribute the full moment, pairs and most groups of four are antiferromagnetically coupled and make no net contribution, triplets contribute $m_{spin}/3$. Large antiferromagnetically coupled clusters of N atoms will make a contribution of $m_{spin}/N^{1/2}$.[7,17] Antiferromagnetism or ferrimagnetism might appear where there are continuous paths throughout the crystal joining nearest neighbor magnetic Co cations.[1,3]

In our Co-doped ZnO samples, the majority of the Co^{2+} ions incorporated at Zn sites have no nearest Co^{2+} neighbor for low Co concentrations. Most of the magnetism arises through intervening Zn and therefore corresponds to the isolated case.[20] As $\boldsymbol{x}$ increases, the fraction of Co^{2+} that have nearest Co^{2+} neighbor grows rapidly, the Co spins might be antiferromagnetically coupled between nearest neighbor due to superexchange interaction which is short-ranged.[3,21] Hence, the magnetic property of the samples might be derived from the isolated Co^{2+} ions[20] that have no nearest neighbor Co^{2+} in the Co-doped ZnO films and these form larger fractions of the magnetic ions when $\boldsymbol{x}$ is smaller, particularly in $Zn_{0.985}Co_{0.015}O$, $Zn_{0.979}Co_{0.021}O$ and $Zn_{0.977}Co_{0.023}O$.

Secondly, the FM of the Co-doped samples might be due to the acquisition of moment through electronic effects by the atoms surrounding the cobalt atoms in the sample, or that the orbital moment of the cobalt remains unquenched.[1,19,22] The rapid decrease in M_s (μ_B/Co) on the increment of dopant concentration might be due to the enhanced dopant-dopant associations leading to progressive orbital moment quenching.

The third reason can be ascribed to the presence of Co_3O_4 clusters which are AFM[23,24] at room temperature. $Zn_{0.961}Co_{0.039}O$ contains approximately 14.0% Co_3O_4 clusters. Hence, the existence of AFM Co_3O_4 tends to decrease the ferromagnetism (FM) contributed by the isolated Co^{2+} ions, in agreement with reference [4]. The drop in M_s after a high temperature treatment of $Zn_{0.977}Co_{0.023}O$ might be due to the enhanced dopant-dopant associations[1] or the AFM interactions in the Co_3O_4 clusters which

precipitated after annealing. These explain the drop in the effective magnetic moment per Co atom with the increment of $\boldsymbol{x}$.

Finally, E Dudzik et al.[25] reported that Co clusters grown on Au (111) are superparamagnetic at room temperature. M. Klimenkov et al.[26], on the other hand, reported that magnetic measurements at temperatures between 2 K and 360 K reveal superparamagnetic behaviour of the small Co nanoclusters in SiO_2 films up to 3 nm and FM for clusters above 7 nm. The Co constituents of $Zn_{0.790}Co_{0.210}O$ and $Zn_{0.809}Co_{0.191}O$, as given by EXAFS results in section 5.3.1, imply that there are 48.1% Co^0 and 51.9% of interstitial Co^{2+} substituted in Zn sites and 47.1% Co^0 and 52.9% of interstitial Co^{2+} substituted in Zn sites, respectively. Hence, the fourth reason that accounts for the trend might be due to the formation of these superparamagnetic Co nanoclusters[21] at high Co concentrations.

$Zn_{0.790}Co_{0.210}O$ shows no distinct hysteresis in Fig. 6.1; the M-H loop suggests paramagnetism of the sample. The Co^0 precipitated in $Zn_{0.790}Co_{0.210}O$ might have formed very small Co nanoclusters, leading to superparamagnetism. Thus, it can be deduced that $Zn_{0.790}Co_{0.210}O$ consists of a mixture of ferromagnetic and paramagnetic clusters of Co atoms at room temperature, i.e. superparamagnetic stage. $Zn_{0.809}Co_{0.191}O$, on the other hand, might have contained less of such small Co nanoclusters since superparamagnetism is not evident from the hysteresis M-H loop in Fig. 6.1. Nevertheless, the overall $M_s(\mu_B/Co)$ decreases. Thus, the possibility of the existence of these superparamagnetic Co clusters in $Zn_{0.809}Co_{0.191}O$ cannot be eliminated.

Table. 6.2. The saturation magnetic moments M_s of Co-doped ZnO films deposited on Si (100) and the atmosphere under which they are fabricated.

Sample name	Atmosphere	M_s (emu/ g)
$Zn_{0.985}Co_{0.015}O$	Ar + N_2	0.249 ± 0.004
$Zn_{0.979}Co_{0.021}O$	Ar + N_2	0.118 ± 0.003
$Zn_{0.977}Co_{0.023}O$	Ar + N_2	0.152 ± 0.001
$Zn_{0.977}Co_{0.023}O$, annealed	Ar + N_2	0.060 ± 0.002
$Zn_{0.961}Co_{0.039}O$	Ar + O_2	0.155 ± 0.004
$Zn_{0.809}Co_{0.191}O$	Ar + N_2	0.191 ± 0.0004
$Zn_{0.790}Co_{0.210}O$	Ar	---

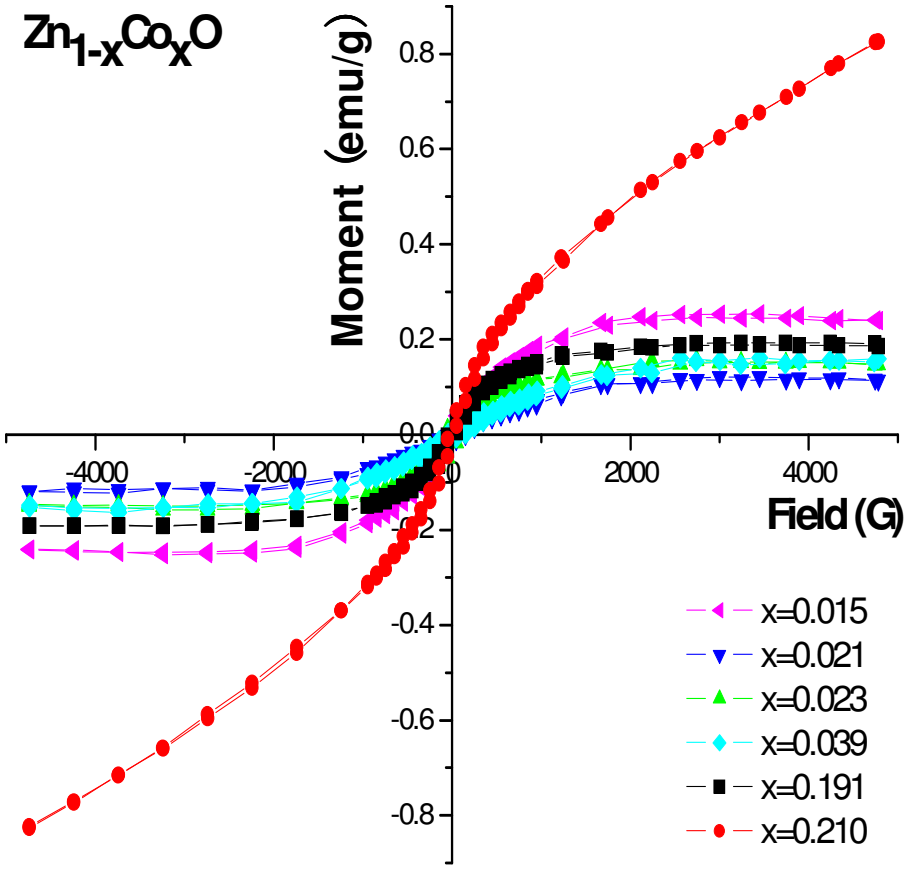

Fig. 6.5. M-H loops measured at room temperature for Co-doped ZnO films deposited on Si (100).

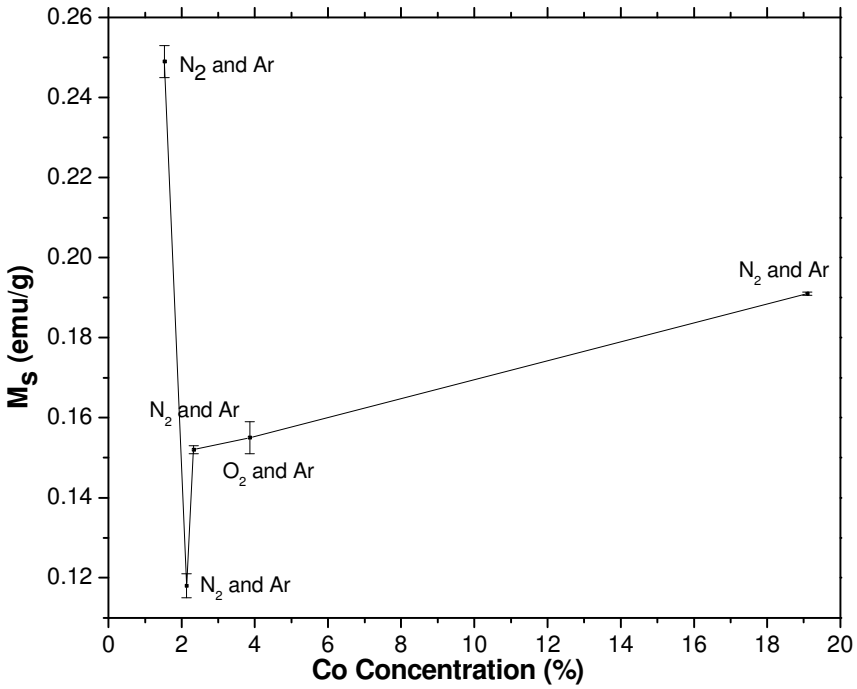

Fig. 6.6. The room temperature saturation magnetic moments M_s as a function of the measured Co concentrations ***x*** of the Co-doped specimens.

Table 6.2 tabulates the M_s (emu/g) of Co-doped ZnO films deposited on Si (100). Fig. 6.5 displays the M-H magnetization (emu/g) curves measured at room temperature while Fig. 6.6 displays the variation of M_s (emu/g) with Co concentration ***x*** of the samples. In contrast with the results plotted in terms of μ_B/Co in Fig. 6.4, the total absolute M_s increases with increasing ***x***. The exception is the case of $Zn_{0.985}Co_{0.015}O$ which has an extremely large number of isolated Co^{2+} ions, leading to a very large effective magnetic moment per Co. This can be ascribed to the fact that the total number of the isolated Co^{2+} ions is larger for higher ***x***; this portion of the Co^{2+} ions contributes to FM, hence leading to larger total absolute magnetic moment with increase in ***x*** even though Co_3O_4 and Co clusters exist.

6.3.2 Cu-doped ZnO

The M-H magnetization (μ_B/Cu) curves measured at room temperature are shown in Fig. 6.7. All Cu-doped ZnO films are ferromagnetic as observed through the M-H hysteresis loops. The resistivity of our Cu-doped ZnO samples is high such that a magnetic coupling interaction other than carrier-mediated exchange exists.

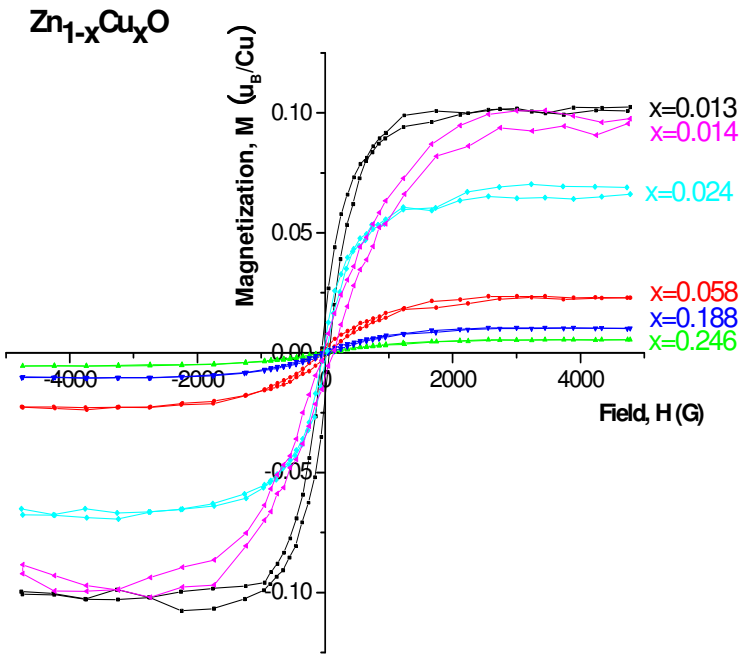

Fig. 6.7. M-H loops measured at room temperature for Cu-doped ZnO films deposited on Si (100).

Xiaobing Feng et al.[27] employed the Becke three parameter Lee-Yang-Parr (B3LYP) hybrid density functional method in the GGA approximation to study the electronic structure and possible ferromagnetic ordering in $Zn_{1-x}TM_xO$ (TM= Cu, Mn). For the case of Cu, the results indicate that in n-type ZnO, electrons would rather occupy the empty Cu 3d states, leading to Cu^+ state instead of Cu^{2+} ions because the unoccupied Cu 3d state is lower than the host conduction band states.[27] The total energies for different magnetic configurations and different distances were calculated between the Cu ions when two Zn ions are substituted with Cu ions. In one case ('far'), the two Cu ions are well separated along the *c*-axis with a Cu–Cu distance of 5.205 Å; in the other case ('near'), the two Cu ions are in the *ab* plane and have a distance of 3.249 Å which is the shortest distance between two cations in the *ab* plane.[27] The results reveal that the magnetic phases are more stable than the non-magnetic ones. In the 'near' case, the AFM state is favoured over the ferromagnetic one while in the 'far' case, the FM state has the lowest energy.[27,28] Of all the magnetic configurations, the FM state with the largest distance between the two Cu ions has the lowest total energy which implies that ferromagnetic semiconductors can be obtained by doping Cu into ZnO.[27,28] The calculation indicates that the magnetic couplings between Cu ions depend on the Cu–Cu distances.[26,27] In other words, FM state is stabilised for "isolated" Cu^+ ions. The calculation also shows that Cu-clustering is not stable in the ground state and it is detrimental to the FM of Cu-doped ZnO.[27]

Similar to Co-doped ZnO, the possible origins of the FM of Cu-doped ZnO might be ascribed to 1) the spin-split impurity-band model whereby the impurity band is found to primarily arise from the hybridization of the Cu 3d level with O 2p states[28] and/or 2) the intrinsic magnetism that can be explained by the BMP model.

Table. 6.3. The saturation magnetic moments M_s of Cu-doped ZnO films deposited on Si (100) and the atmosphere under which they are fabricated.

Sample name	Atmosphere	M_s/μ_B per Cu atom
$Zn_{0.987}Cu_{0.013}O$	Ar	0.101 ± 0.001
$Zn_{0.986}Cu_{0.014}O$	Ar + N_2	0.097 ± 0.004
$Zn_{0.986}Cu_{0.014}O$, annealed	Ar + N_2	0.056 ± 0.001
$Zn_{0.976}Cu_{0.024}O$	Ar + N_2	0.067 ± 0.001
$Zn_{0.942}Cu_{0.058}O$	Ar	0.023 ± 0.0003
$Zn_{0.812}Cu_{0.188}O$	Ar + N_2	0.010 ± 0.0001
$Zn_{0.754}Cu_{0.246}O$	Ar	0.005 ± 0.00006

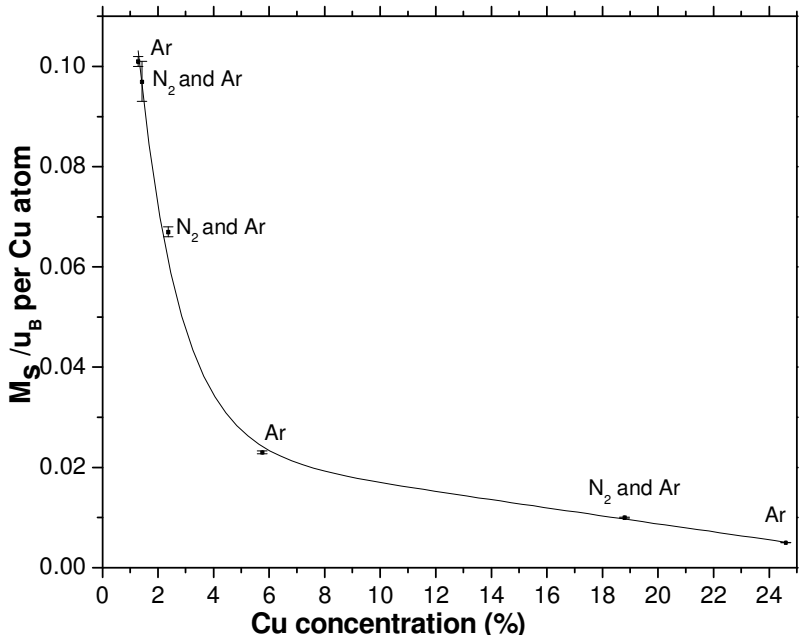

Fig. 6.8. The room temperature saturation magnetic moments M_s as a function of the measured Cu concentrations ***x*** of the Cu-doped specimens. The Cu concentration in the sample was estimated by XRF measurements.

Table 6.3 summarizes the M_s (μ_B/Cu) of Cu-doped ZnO films deposited on Si (100). Fig. 6.8 displays the variation of M_s (μ_B/Cu) with Cu concentration ***x*** of the samples. The largest measured moment is $0.101\pm0.001\mu_B$/Cu in $Zn_{0.987}Cu_{0.013}O$ whereas the theoretical value of the magnetic moment of Cu doped in ZnO is predicted to be 0.[12] However, many papers[29-31] have reported the presence of FM in their Cu-doped ZnO samples with magnetic moment as high as 0.75 μ_B/Cu atom.[29] Table 6.3 and Fig. 6.8, again, display a consistent decrease in M_s with increasing ***x***, in

agreement with reference [27]. This similar trend probably has the same explanations as Co-doped ZnO.

Firstly, at higher Cu concentrations, there is an increasing occurrence of AFM coupling between Cu pairs occurring at shorter separation distance. This has been predicted in theoretical studies.[27,32] Secondly, the rapid drop in M_s (μ_B/Cu) on the increment of Cu concentration can be attributed to the enhanced dopant-dopant associations leading to progressive orbital moment quenching.

Thirdly, the decrease in magnetic moment per Cu is related to the presence of Cu_2O which is AFM.[29,30,33] EXAFS results in section 5.3.2 confirm the existence of Cu_2O clusters in $Zn_{0.986}Cu_{0.014}O$ and $Zn_{0.976}Cu_{0.024}O$. The decrease in M_s after annealing $Zn_{0.986}Cu_{0.014}O$ at 800°C might be due to the enhanced dopant-dopant associations[1] or the AFM interactions in the Cu_2O clusters which formed after calcination.

Copper clusters, on the other hand, are non-magnetic.[27-29,34] Lastly, as mentioned previously, Cu-clustering is not stable in the ground state and it is detrimental to FM in Cu-doped ZnO.[27] Cu clusters are also found in $Zn_{0.987}Cu_{0.013}O$, $Zn_{0.942}Cu_{0.058}O$, $Zn_{0.812}Cu_{0.188}O$ and $Zn_{0.754}Cu_{0.246}O$, as indicated by EXAFS results in section 5.3.2. All the above reasons explain why M_s (μ_B/Cu) drops off with increasing $\boldsymbol{x}$ values.

Table. 6.4. The saturation magnetic moments M_s of Cu-doped ZnO films deposited on Si (100) and the atmosphere under which they are fabricated.

Sample name	Atmosphere	M_s (emu/g)
$Zn_{0.987}Cu_{0.013}O$	Ar	0.089 ± 0.001
$Zn_{0.986}Cu_{0.014}O$	Ar + N_2	0.095 ± 0.003
$Zn_{0.986}Cu_{0.014}O$, annealed	Ar + N_2	0.055 ± 0.001
$Zn_{0.976}Cu_{0.024}O$	Ar + N_2	0.109 ± 0.002
$Zn_{0.942}Cu_{0.058}O$	Ar	0.090 ± 0.001
$Zn_{0.812}Cu_{0.188}O$	Ar + N_2	0.132 ± 0.002
$Zn_{0.754}Cu_{0.246}O$	Ar	0.092 ± 0.001

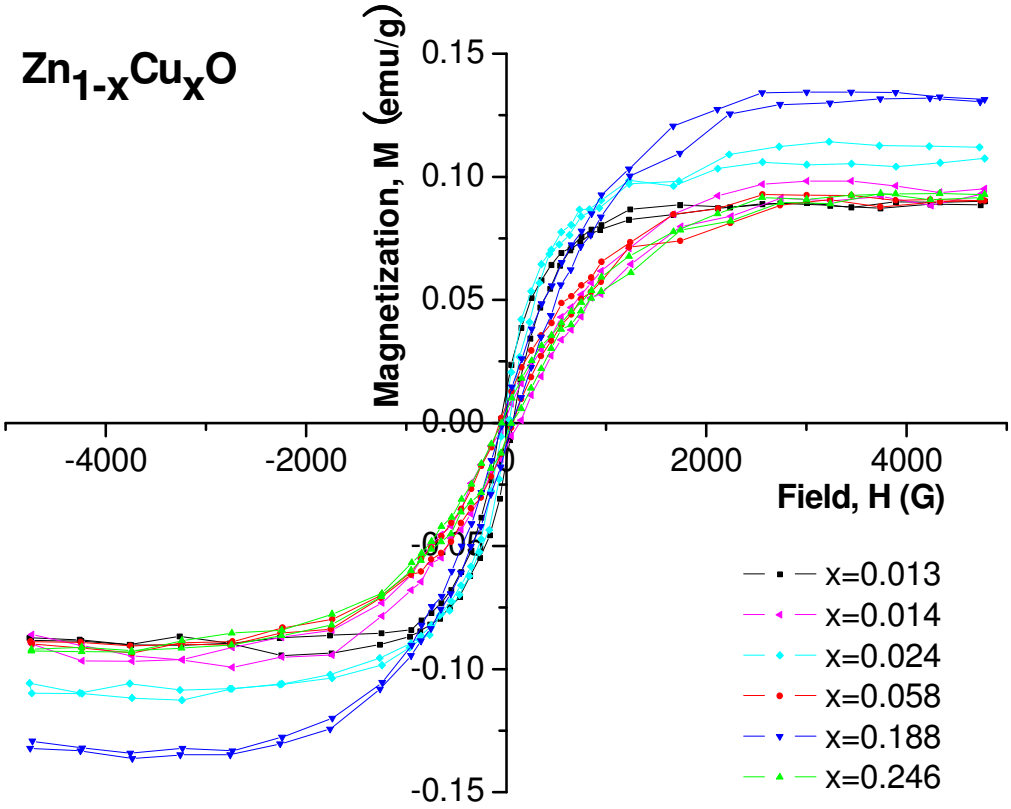

Fig. 6.9. M-H loops measured at room temperature for Cu-doped ZnO films deposited on Si (100).

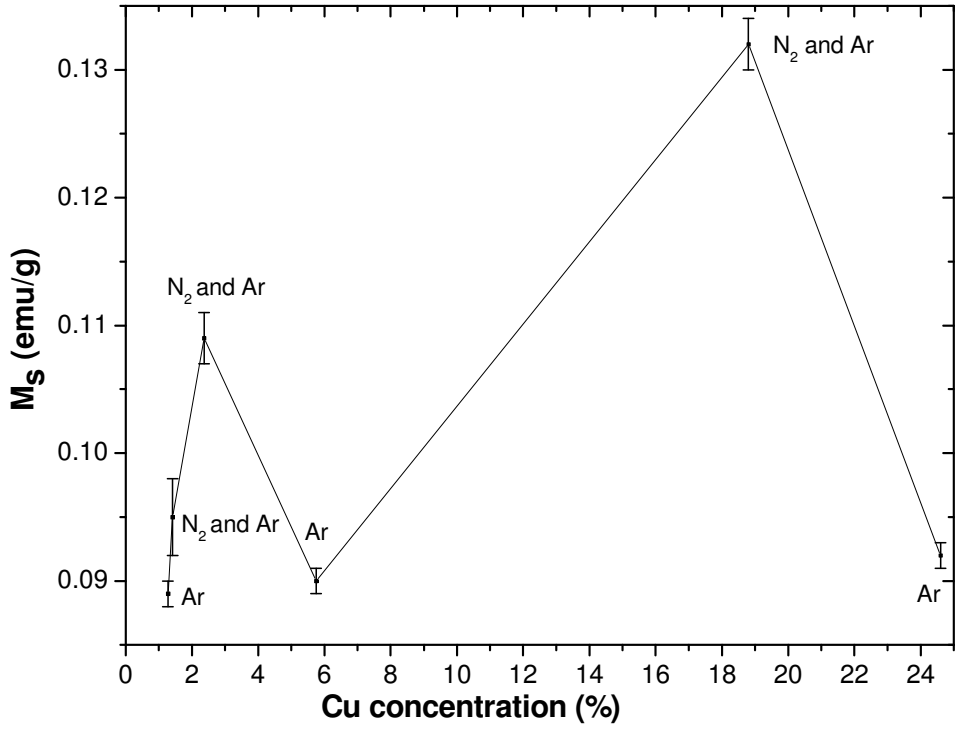

Fig. 6.10. The room temperature saturation magnetic moments M_s as a function of the measured Cu concentrations ***x*** of the Cu-doped specimens.

Table 6.4 tabulates the M_s (emu/g) of Cu-doped ZnO films deposited on Si (100). Fig. 6.9 displays the M-H magnetization (emu/g) curves measured at room temperature while Fig. 6.10 displays the variation of the magnetic moment M_s (emu/g) with Cu concentration $\boldsymbol{x}$ of the samples. Contrary to the results plotted in terms of μ_B/Cu in Fig. 6.8, the total absolute magnetic moment does not decrease with increasing $\boldsymbol{x}$. It is observed that for all Cu-doped ZnO films fabricated under Ar ambient, the M_s values are roughly the same (0.090emu/g) which implies that M_s is independent of $\boldsymbol{x}$. On the other hand, the M_s values increase readily with the increment of $\boldsymbol{x}$ for films fabricated under 85%Ar + 15%N_2 atmosphere.

EXAFS results have confirmed the existence of Cu clusters in $Zn_{0.987}Cu_{0.013}O$, $Zn_{0.942}Cu_{0.058}O$ and $Zn_{0.754}Cu_{0.246}O$ which are all fabricated under Ar ambient, whereas 85%Ar + 15%N_2 atmosphere has favored the formation of AFM Cu_2O clusters in $Zn_{0.986}Cu_{0.014}O$ and $Zn_{0.976}Cu_{0.024}O$. Under 85%Ar + 15%N_2 atmosphere, $Zn_{0.812}Cu_{0.188}O$ has a mixture of Cu and Cu_2O clusters due to its high Cu content. It is postulated that in the samples fabricated under 85%Ar + 15%N_2 ambient, a lot more isolated Cu^+ ions (which contribute to FM state) are present which increases with rise in $\boldsymbol{x}$, leading to a higher total absolute magnetic moment. Although AFM Cu_2O clusters exist in these samples, the larger magnitude of FM might be able to overcome it. It is also postulated that the samples fabricated under Ar atmosphere have a high percentage of non-magnetic Cu clusters and a fixed small number of isolated Cu^+ ions. Thus, the M_s values almost remained constant regardless of $\boldsymbol{x}$ values.

6.3.3 Ti-doped ZnO

The M-H magnetization (μ_B/Cu) curves measured at room temperature are shown in Fig. 6.11. All Ti-doped ZnO films are ferromagnetic as observed through the M-H hysteresis loops. $Zn_{0.995}Ti_{0.005}O$ fabricated under under 80%Ar + 20%O_2 atmosphere might have contained large amounts of FM Ti oxides precipitates, hence it has a higher M_s than the rest of the

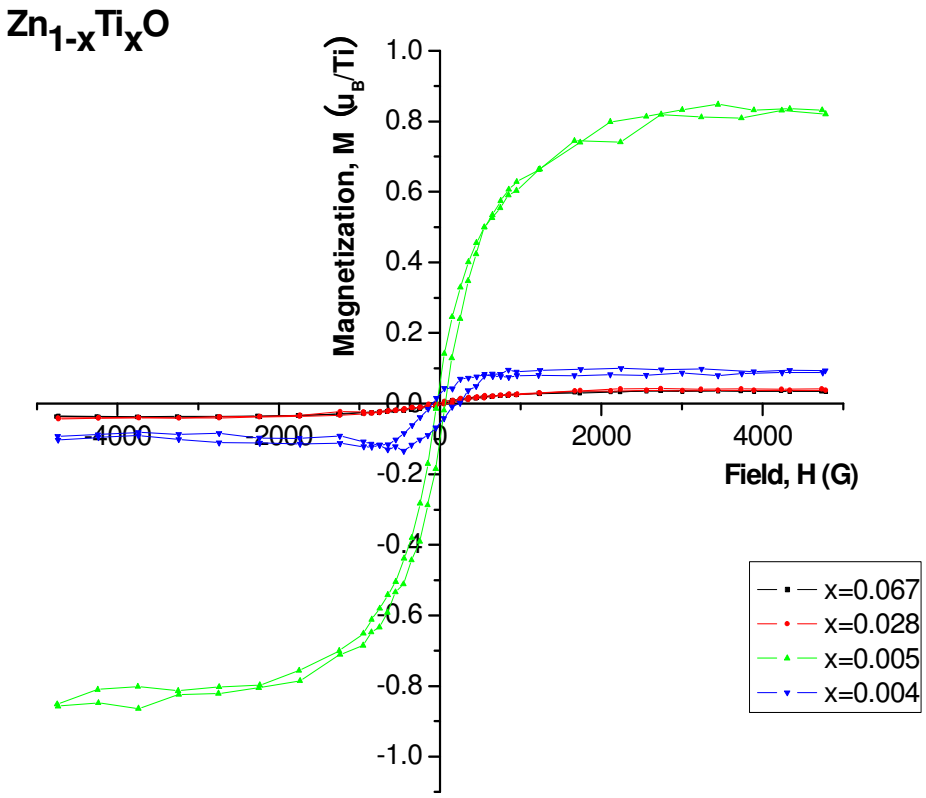

Fig. 6.11. M-H loops measured at room temperature for Ti-doped ZnO films deposited on Si (100).

samples. The Ti-doped ZnO samples are insulators; hence, carrier-mediated FM is not possible.

Osuch et al[35] performed electron density functional theory (DFT) calculations which show that the introduction of titanium induces an impurity band in the lower part of the conduction band with both the majority- and minority-spin components retaining a band gap. The introduction of Ti, therefore, maintains the semiconducting nature of ZnO. The impurity levels associated with the Ti dopant are spin polarized with the Fermi level passing through the Ti related impurity band for the majority spin component.[35] Impurity levels lying close to the Fermi level are spin polarized by 0.6–0.7 eV.[35] These results are consistent with experimental findings of Park et al.[36] and Lin et al.[37] where Ti dopants are found to be donors in ZnO. The impurity band is formed by the hybridization of the Ti 3d level with the 2p states of the O neighbors of Ti.[35] This is also consistent with the experimental findings of Venkatesan *et al.*[7] where it was suggested that ferromagnetic ordering arises in ZnO:Ti

due to an exchange interaction between localized Ti 3d magnetic moments mediated by an overlap of Ti 3d orbitals with a delocalized donor impurity band.[35] It is necessary for a partly occupied Ti 3d impurity band overlaps with a spin polarized donor impurity band to mediate the exchange interaction in that model.[35] *Ab initio* calculations performed by Osuch et al[35] suggest ferromagnetic ordering in the $Ti_{0.0625}Zn_{0.9375}O$ sample without additional doping and that Ti itself is likely to be a *n*-type dopant in ZnO.[35] These results are further supported by the results of Gebicki et al.,[38] where it was found that Raman peaks of ZnO:Ti are associated with electronic transitions in a Ti-related complex strongly coupled to lattice phonons.

Hence, the possible origins of the FM of Ti-doped ZnO might be ascribed to 1) the spin-split impurity-band model whereby the impurity band is formed by the hybridization of the Ti 3d level with the 2p states of the O neighbors of Ti and/or 2) the intrinsic magnetism that can be explained by the BMP model.

Table. 6.5. The saturation magnetic moments M_s of Ti-doped ZnO films deposited on Si (100) and the atmosphere under which they are fabricated.

Sample name	Atmosphere	M_s/μ_B per Ti atom
$Zn_{0.996}Ti_{0.004}O$	$Ar + N_2$	0.090 ± 0.004
$Zn_{0.995}Ti_{0.005}O$	$O_2 + N_2$	0.827 ± 0.013
$Zn_{0.972}Ti_{0.028}O$	$Ar + N_2$	0.039 ± 0.002
$Zn_{0.933}Ti_{0.067}O$	Ar	0.036 ± 0.001

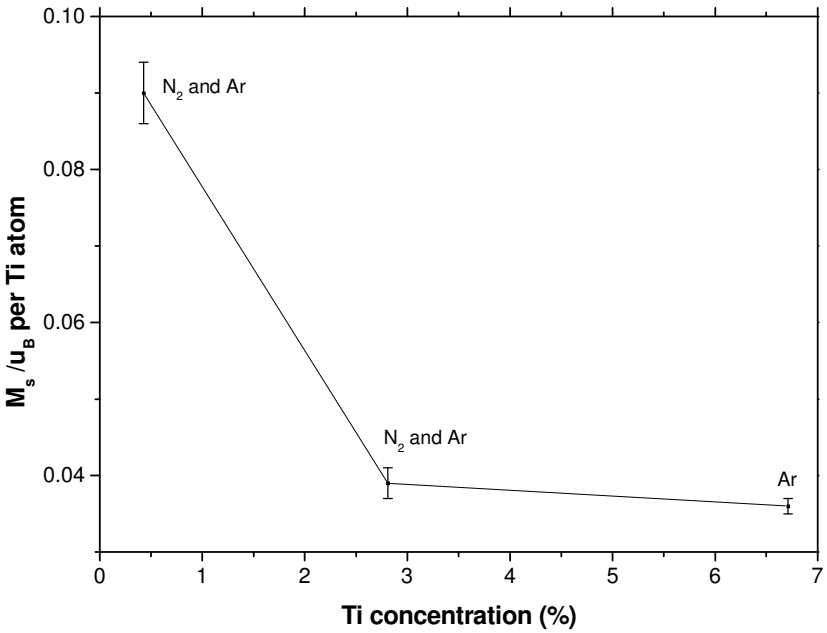

Fig. 6.12. The room temperature saturation magnetic moments M_s as a function of the measured Ti concentrations $\boldsymbol{x}$ of the Ti-doped specimens. The Ti concentration in the sample was estimated by XRF measurements.

Table 6.5 summarizes the M_s (μ_B/Ti) of Ti-doped ZnO films deposited on Si (100). Fig. 6.12 displays the variation of M_s (μ_B/Ti) with Ti concentration $\boldsymbol{x}$ of the samples which excludes $Zn_{0.995}Ti_{0.005}O$. The largest measured moment of Ti-doped ZnO, excluding $Zn_{0.995}Ti_{0.005}O$ which contains large amounts of FM Ti oxides precipitates, is $0.090\pm0.004\mu_B$/Ti in $Zn_{0.996}Ti_{0.004}O$. The theoretical value of the magnetic moment of Ti doped in ZnO is predicted to be 0 by Sato et al.[12] However, Antony et al.[39] reported a saturation moment of 0.15 μ_B/Ti atom at room temperature for 5% Ti-doped ZnO sample, and Osuch et al[35] performed DFT calculations predicting a magnetic moment of $0.63\mu_B$ per supercell in $Zn_{0.9375}Ti_{0.0625}O$. Table 6.5 (omitting $Zn_{0.995}Ti_{0.005}O$) and Fig. 6.12 display a consistent decrease in M_s with increasing $\boldsymbol{x}$. This similar trend probably has the same explanations as Co and Cu-doped ZnO.

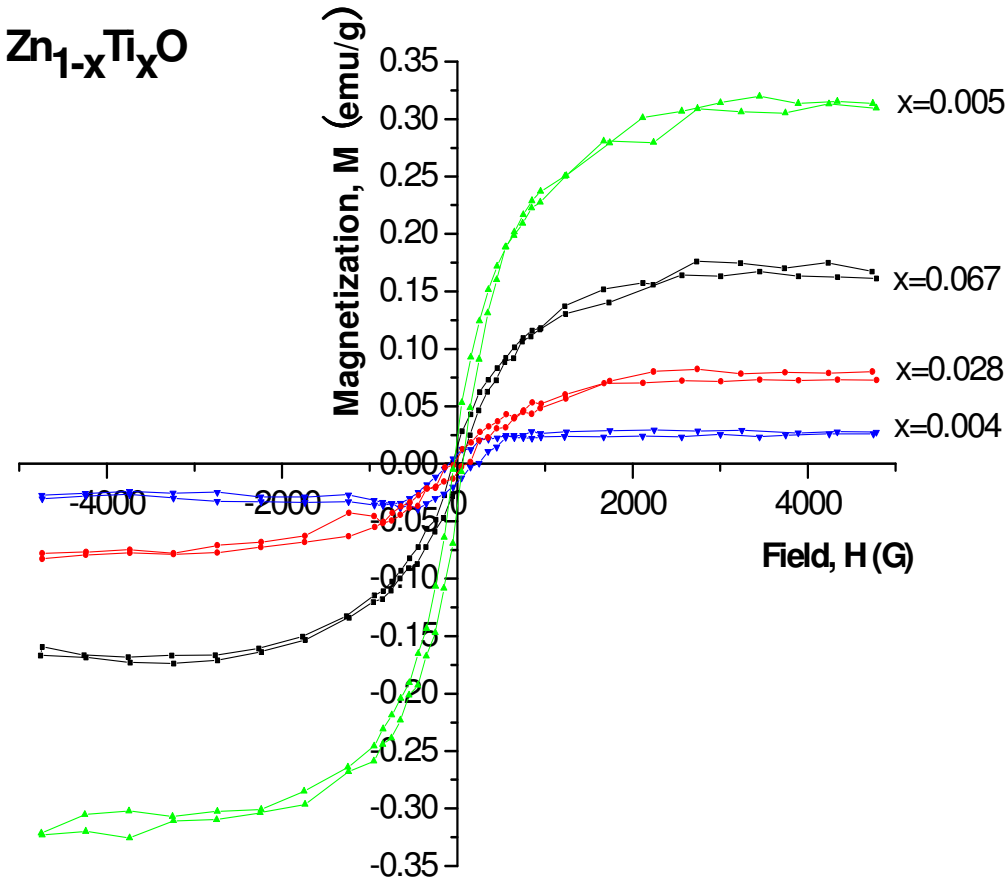

Fig. 6.13. M-H loops measured at room temperature for Ti-doped ZnO films deposited on Si (100).

Table. 6.6. The saturation magnetic moments M_s of Ti-doped ZnO films deposited on Si (100) and the atmosphere under which they are fabricated.

Sample name	Atmosphere	M_s (emu/g)
$Zn_{0.996}Ti_{0.004}O$	Ar + N_2	0.027 ± 0.001
$Zn_{0.995}Ti_{0.005}O$	O_2 + N_2	0.312 ± 0.005
$Zn_{0.972}Ti_{0.028}O$	Ar + N_2	0.076 ± 0.003
$Zn_{0.933}Ti_{0.067}O$	Ar	0.168 ± 0.005

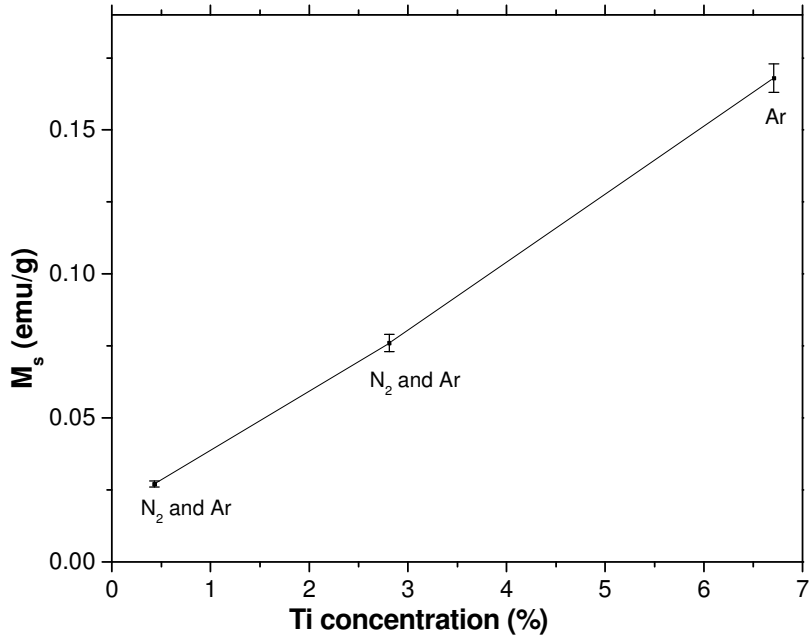

Fig. 6.14. The room temperature saturation magnetic moments M_s as a function of the measured Ti concentrations $\boldsymbol{x}$ of the Ti-doped specimens.

Table 6.6 tabulates the M_s (emu/g) of Ti-doped ZnO films deposited on Si (100). Fig. 6.13 displays the M-H magnetization (emu/g) curves measured at room temperature while Fig. 6.14 shows the variation of the magnetic moment M_s (emu/g) with Ti concentration $\boldsymbol{x}$ which excludes $Zn_{0.995}Ti_{0.005}O$. Unlike in Fig. 6.12, the total absolute magnetic moment increases almost linearly with increasing $\boldsymbol{x}$ with the exception of $Zn_{0.995}Ti_{0.005}O$ which contains large amounts of FM Ti oxides precipitates. This can be attributed to the fact that the total number of isolated Ti^{3+} ions is larger for higher $\boldsymbol{x}$. This portion of the Ti^{3+} ions contributes to FM, hence leading to larger total absolute magnetic moment with increase in $\boldsymbol{x}$.

6.3.4 Mn-doped ZnO

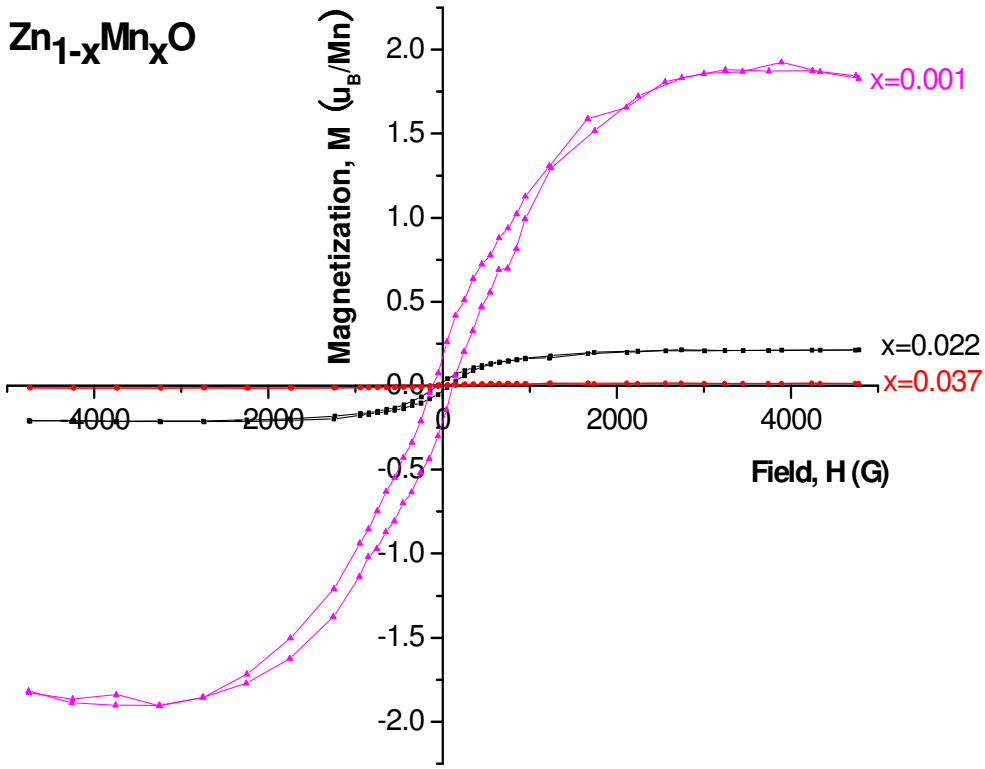

Fig. 6.15. M-H loops measured at room temperature for Mn-doped ZnO films deposited on Si (100).

The M-H magnetization (μ_B/Mn) curves measured at room temperature for Mn-doped ZnO films deposited on Si (100) are shown in Fig. 6.15. All Mn-doped ZnO films are ferromagnetic as observed through the M-H hysteresis loops. The Mn-doped ZnO samples are insulators; hence, carrier-mediated FM is not possible. Xiao-yun et al.[40] reported that the insertion of Mn^{2+} ions leads to formation of defects in the ZnO host matrix. Thus, the FM of $Zn_{1-x}Mn_xO$ films is strongly related to the defects in ZnO.[40,41]

Yan et al.[41] reported that the room-temperature ferromagnetism of $Zn_{0.97}Mn_{0.03}O$ grown by metal organic chemical vapour deposition (MOCVD) method may be connected with the presence of Zn vacancy (V_{Zn}). They used the Vienna *ab initio* simulation package (VASP) to calculate the electronic structure and magnetic interactions between Mn ions in the model structure of Mn_{Zn}+V_{Zn}.[41] The calculations showed that the FM configuration is energetically favoured over the AFM configuration by 22meV in total energy, indicating the stability of the FM state against the

AFM state for Mn_{Zn}+V_{Zn}.[41] This is in agreement with previous theoretical calculations.[42,43] The hybridization between the Mn $3d^{\uparrow}$ and defect a_1 states facilitates the electron transfer from Mn $3d^{\uparrow}$ states to the acceptor.[41] According to the BMP model, the charge transfer between the Mn 3d and a_1 states favours an enhancement of the Curie temperature T_C.[41] From first-principles calculations, it was concluded that the Zn vacancy favours the room-temperature ferromagnetism in the $Zn_{0.97}Mn_{0.03}O$ thin film. [41]

For the spin-split impurity-band model, there is no overlap of the donor impurity band with the 3d levels of Mn as shown in Fig. 6.16 and the exchange is weak.[7] Hence, the possible origins of the FM of Mn-doped ZnO might be ascribed to the intrinsic magnetism that can be explained by the BMP model. However, there are also several theoretical and experimental reports[12,44] on AFM found in Mn-doped ZnO.

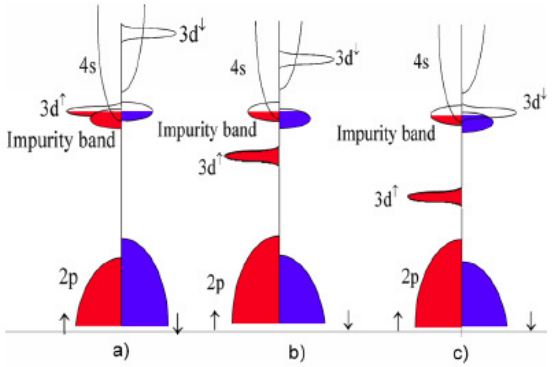

Fig. 6.16. Schematic density of states for (a) TM= Ti, (b) TM = Mn, and (c) TM = Co. The Fermi level lies in a spin-split donor impurity band.[7]

Table. 6.7. The saturation magnetic moments M_s of Mn-doped ZnO films deposited on Si (100) and the atmosphere under which they are fabricated.

Sample name	Atmosphere	M_s/μ_B per Mn atom
$Zn_{0.999}Mn_{0.001}O$	Ar + N_2	1.882 ± 0.022
$Zn_{0.978}Mn_{0.022}O$	Ar + O_2	0.211 ± 0.001
$Zn_{0.963}Mn_{0.037}O$	Ar	0.013 ± 0.0007
$Zn_{0.963}Mn_{0.037}O$, annealed	Ar	0.034 ± 0.0009

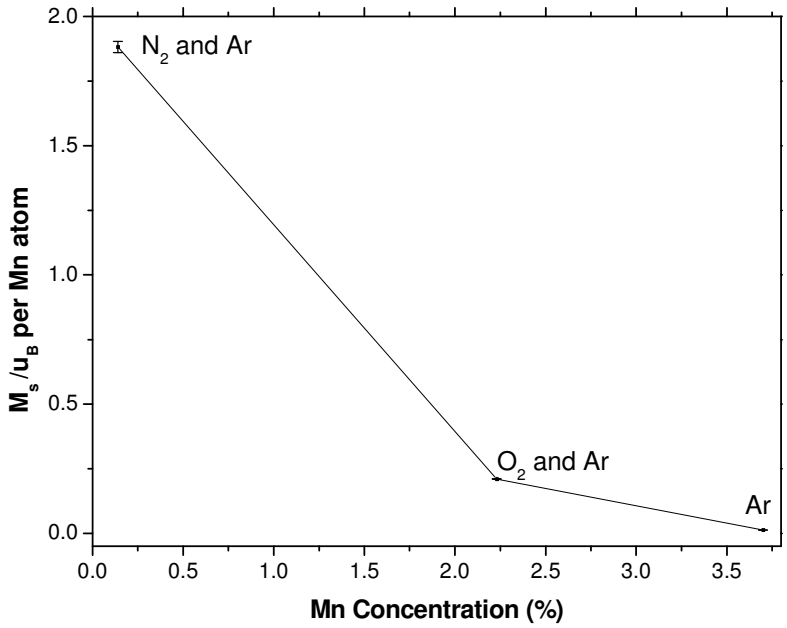

Fig. 6.17. The room temperature saturation magnetic moments M_s as a function of the measured Mn concentrations ***x*** of Mn-doped specimens. The Mn concentration in the sample was estimated by XRF measurements.

Table 6.7 summarizes the M_s (μ_B/Mn) of Mn-doped ZnO films deposited on Si (100). Fig. 6.17 displays the variation of M_s (μ_B/Mn) with Mn concentration ***x*** of the samples. The largest measured moment of $Zn_{0.999}Mn_{0.001}O$ is 1.882±0.022μ_B/Mn, smaller than the spin-only moment m_{spin}= 5μ_B Mn^{2+} in the high spin state.[3,12,41,45] This is a common phenomenon for DMS materials, usually ascribed to the competition between the FM interaction and AFM superexchange coupling of neighboring Mn^{2+} ions.[42] Several papers[3,7,41,45] reported low M_s <0.5μ_B/Mn in Mn-doped ZnO, in contrast to our results for $Zn_{0.999}Mn_{0.001}O$. This indicates that there might be other factors leading to FM in our samples which will be further discussed in section 6.3.5.

Table 6.7 and Fig. 6.17 display a consistent decrease in M_s with increasing ***x***, in agreement with references [41], [44], [46] and [47]. This similar trend probably has the same explanations as the rest of the TM-doped ZnO. With increasing x, the fraction of Mn ions pairs and groups of four Mn ions or more formed AFM clusters which do not contribute to the magnetic signal increases which reduces the net magnetization.[41,47,48] The slight increase in M_s after annealing $Zn_{0.963}Mn_{0.037}O$ at 800^{o}C might be due

to the precipitation of small amounts of Mn_3O_4 which is FM with T_c of 46K.[41,49] Nearly all possible Mn-based binary and ternary oxide candidates are AFM[41] and these include MnO and MnO_2 with Neel temperatures of 116 and 84K respectively.[45]

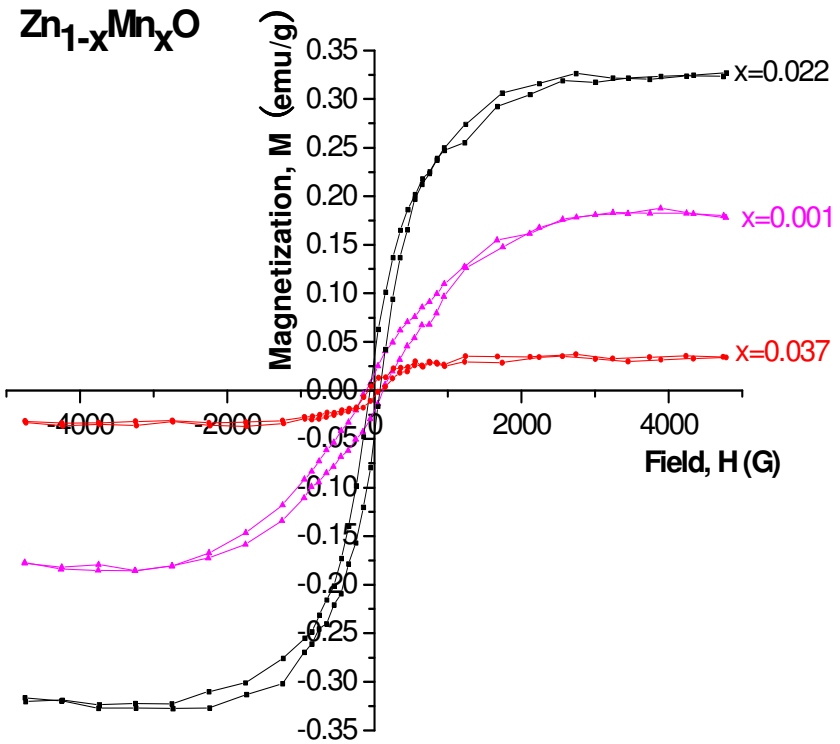

Fig. 6.18. M-H loops measured at room temperature for Mn-doped ZnO films deposited on Si (100).

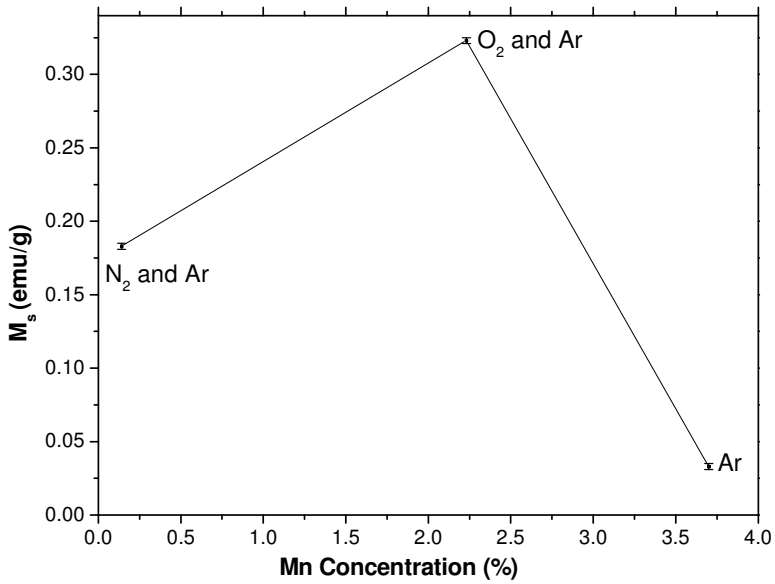

Fig. 6.19. The room temperature saturation magnetic moments M_s as a function of the measured Mn concentrations ***x*** of the Mn-doped specimens.

Table. 6.8. The saturation magnetic moments M_s of Mn-doped ZnO films deposited on Si (100) and the atmosphere under which they are fabricated.

Sample name	Atmosphere	M_s (emu/g)
$Zn_{0.999}Mn_{0.001}O$	Ar + N_2	0.183 ± 0.002
$Zn_{0.978}Mn_{0.022}O$	Ar + O_2	0.323 ± 0.002
$Zn_{0.963}Mn_{0.037}O$	Ar	0.033 ± 0.002
$Zn_{0.963}Mn_{0.037}O$, annealed	Ar	0.087 ± 0.002

Table 6.8 tabulates the M_s (emu/g) values of Mn-doped ZnO films deposited on Si (100). Fig. 6.18 displays the M-H magnetization (emu/g) curves measured at room temperature while Fig. 6.19 shows the variation of the magnetic moment M_s (emu/g) with Mn concentration $\boldsymbol{x}$.

The total absolute magnetic moment decreases with the increment of $\boldsymbol{x}$ with the exception of $Zn_{0.978}Mn_{0.022}O$ which is suspected to contain small amounts of FM Mn_3O_4; this is plotted in terms of μ_B/Mn in Fig. 6.12. This suggests that the AFM superexchange coupling between Mn atoms is energetically more favorable than FM as $\boldsymbol{x}$ increases[48]; Mn atoms will gather close to each other, cluster around O atom and exhibit AFM behavior which leads to a net reduction in magnetization.[48,50,51]

6.4 Summary

VSM measurements at room temperature reveal that the TM (Co, Cu, Ti and Mn)–doped ZnO films are ferromagnetic. The origins of the FM of our insulating TM-doped ZnO samples can generally be attributed to 1) the spin-split impurity-band model and/or 2) the intrinsic magnetism that can be explained by the BMP model.

The largest measured moments for TM-doped ZnO without any precipitation are 0.237±0.004 μ_B/Co in $Zn_{0.985}Co_{0.015}O$, 0.090±0.004μ_B/Ti in $Zn_{0.996}Ti_{0.004}O$ and 1.882±0.022μ_B/Mn in $Zn_{0.999}Mn_{0.001}O$.

In all TM–doped ZnO films, M_s(μ_B/TM atom) is generally found to decrease with increasing $\boldsymbol{x}$. This trend can be explained by a few reasons. Firstly, at higher TM concentrations, there is an increasing occurrence of AFM coupling between TM pairs, groups of four and coupled clusters of N

number of TM atoms. Secondly, the rapid drop in M_s with increasing TM content can be attributed to enhanced dopant-dopant associations leading to progressive orbital moment quenching. Thirdly, the formation of AFM TM oxide clusters at high TM concentrations might also lead to the fall in $M_s(\mu_B$/TM atom).

References

1. C. Song, K.W. Geng, F. Zeng, X.B. Wang, Y.X. Shen, F. Pan, Y.N. Xie, T. Liu, H.T. Zhou and Z. Fan, Phys. Rev. B, **73**, 024405 (2006).
2. J Marcel H.F. Sluiter, Y. Kawazoe, Paramanand Sharma, A. Inoue, A.R. Raju, C. Rout and U.V. Waghmare, Phys. Rev. Lett., **94**, 187204 (2005).
3. J.M.D. Coey, M. Venkatesan and C. B. Fitzgerald, Nat. Mater. **4**, 173 (2005).
4. Tongfei Shi, Sanyuan Zhu, Zhihu Sun, Shiqiang Wei and Wenhan Liu, Appl. Phys. Lett., **90**, 102108 (2007).
5. J.E. Jaffe, T.C. Droubay and S.A. Chambers, J. Appl. Phys., **97**, 073908 (2005).
6. H.M. Weng, X.P. Yang, J.M. Dong, H. Mizuseki, M. Kawasaki and Y. Kawazoe, Phys. Rev. B, **69**, 125219 (2004).
7. M. Venkatesan, C. B. Fitzgerald, J.G. Lunney, and J.M. D. Coey, Phys. Rev. Lett., **93**, 177206 (2004).
8. A.P. Roth, J.B. Webb and D. F. Williams, Phys. Rev. B, 25, 7836 (1982).
9. A. F. Kohan, G. Ceder, D. Morgan and C.G.Van deWalle, Phys. Rev. B, **61**, 15019 (2000).
10. S. B. Zhang, S. H. Wei and A. Zunger, Phys. Rev. B, **63**, 075205 (2001).
11. N. F. Mott, Conduction in Noncrystalline Materials (Oxford University Press, New York, 1987).
12. K. Sato and H. Katayama-Yoshida, Physica E, **10**, 251. (2001).
13. A. Kaminski and S. Das Sarma, Phys. Rev. Lett., **88**, 247202 (2002).
14. P. A. Wolff, R. N. Bhatt, and A. C. Durst, J. Appl. Phys., **79**, 5196 (1996).
15. C. Liu, F. Yun and H. Morkoc, J. Mat. Science in Electronics, **16**, 555 (2005)
16. P. A. Cox, Transition Metal Oxides (Clarendon, Oxford, 1992).
17. C.B. Fitzgerald, M. Venkatesan, J.G. Lunny, L.S. Dorneles and J.M.D. Coey, Applied Surface Science **247**, 493 (2005).
18. S-J Han, B.Y. Lee, J.-S. Ku, Y.B. Kim and Y.H. Jeong, J. Magn. Magn. Mater., **272**, 2008 (2004).
19. S.B Ogale, R.J. Choudhary, J.P. Buhan. S.E. Lofland, S.R Shinde, S.N. Kale, V.N. Kulkarni, J. Higgins, C. Lanci, J.R Simpson, N.D. Browning, S. Das Sarma, H.D. Drew, R.L. Greene and T. Venkatesan, Phys. Rev. Lett., **91**, 077205-1 (2003).
20. A.S. Risbud, N.A. Spaldin, Z.Q. Chen, S. Stemmer and Ram Seshadri, Phys. Rev. B, **68**, 205202 (2003).
21. A. Dinia, G. Schmerber, C. Mény, V. Pierron-Bohnes, and E. Beaurepaire, J. Appl. Phys., **97**, 123908 (2005).

22. K.W. Edmonds, C. Binns, S.H. Baker, S.C. Thornton, C. Norris, J.B. Goedkoop, M. Finazzi and N.B. Brookes, Phys. Rev. B, **60**, 472 (1999).
23. Salah A. Makhlouf, J. Magn. Magn. Mater., **246**, 184 (2002).
24. Yuko Ichiyanagi and Saori Yamada, Polyhedron, **24**, 2813 (2005).
25. E Dudzik, H A D¨urr, S S Dhesi, G van der Laan, D Knabben and J B Goedkoop, J. Phys.: Condens. Matter, **11**, 8445 (1999).
26. M. Klimenkov, J. von Borany, W.Matz, D. Eckert, M. Wolf and K.-H. Müller, Appl. Phys. A, **74**, 571 (2002).
27. Xiaobing Feng, J. Phys.: Condens. Matter, **16,** 4251 (2004).
28. ZH Xiong, SQ Shi, QX Wan and FY Jiang, Physica Scripta, **T129**, 358 (2007).
29. D. Chakraborti, J. Narayan and J.T. Prater, Appl. Phys. Lett., **90**, 062504 (2007).
30. T.S. Herng, S.P. Lau, S.F. Yu, H.Y. Yang, X.H. Ji, J. Appl. Phys, **99**, 086101 (2006)
31. Hyeon-Jun Lee, Bo-Seong Kim, Chae Ryong Cho and Se-Young Jeong, Phys. Stat. Sol, **241**, 1533 (2004).
32. L.H. Ye, A.J. Freeman and B. Delley, Phys. Rev. B, **73**, 033203 (2006).
33. M. Wei, N. Braddon, D. Zhi, P.A. Midgley, S.K. Chen M.G. Blamire and J.L. MacManus-Driscoll, Appl. Phys. Lett., **86**, 72514 (2005).
34. http://meetings.aps.org/link/BAPS.2006.MAR.R46.10
35. K. Osuch, E.B. Lombardi and W. Gebicki, Phys. Rev. B, **73**, 075202 (2006).
36. Y. R. Park and K. J. Kim, Solid State Commun., **123**, 147 (2002).
37. S.-S. Lin, J.-L. Huang, and D.-F. Lii, Mater. Chem. Phys., **90**, 22 (2005).
38. W. Gebicki, K. Osuch, C. Jastrzebski, Z. Golacki, and M. Godlewski, Superlattices Microstruct., **38**, 428 (2005).
39. Jiji Antony, Sweta Pendyala, David E. McCready, Mark H. Engelhard, IEEE Transactions On Magnetics, **42**, 2697 (2006).
40. Teng Xiao-yun, Yu Wei, Yang Li-hua, Hao Qiu-yan, Zhang Li, Xu He-ju, Liu Cai-Chi and Fu Guang-Sheng, Chinese Phys. Lett., **24**, 1073 (2007).
41. Wensheng Yan, Zhihu Sun, Qinghua Liu, Zhongrui Li, Zhiyun Pan, Jie Wang, Shiqiang Wei, Dan Wang, Yingxue Zhou and Xinyi Zhang, Appl. Phys. Lett., **91**, 062113 (2007).
42. A. Ben Mahmoud, H. J. Von Bardeleden, J. L. Cantin, A. Mauger, E. Chikoidze, and Y. Dumont, Phys. Rev. B, **74**, 115203 (2006).
43. N. A. Spaldin, Phys. Rev. B, **69**, 125201 (2004).
44. G. Lawes, A.S. Risbud, A.P. Ramirez, Ram Seshadri, Phys. Rev. B, **71**, 045201 (2005).
45. V.A.L Roy, A.B. Djurisic, H. Liu, X.X. Zhang, Y.H Leung, M.H. Xie, J. Gao, H.F. Lui and C. Surya, Appl. Phys. Lett., **84**, 756 (2004).
46. S. J. Pearton, D. P. Norton, K. Ip, and Y. W. Heo, T. Steiner, J. Vac. Sci. Technol. B, **22(3)**, 932 (2004).
47. Sharmai P, Guptai A, Rao K V, Nat. Mater., **2**, 673 (2003).
48. Q. Wang, Q. Sun, B.K. Rao and P. Jena, Phys. Rev. B, **69**, 233310 (2004).
49. M.H Kane, K. Shalini, C.J. Summers, R. Varatharajan, J. Nause, C.R Vestal, Z.J. Zhang and I.T. Ferguson, Appl. Phys, **97**, 023906 (2005).
50. T. Fukumura, Z. Jin. M. Kawasaki, T. Shono, T. Hasegawa, S. Koshihara and H. Koinuma, Appl. Phys, **78**, 958 (2001).

51. S.W. Yoon, S,-B. Cho, S.C. We, S. Yoon, B.J. Suh, H.K Song and Y.J. Shin, **93**, 7879 (2003).

Chapter 7

Conclusions

$Zn_{1-x}TM_xO$ (TM: Co, Cu, Ti and Mn) films were fabricated on Si (100) substrates by radio-frequency magnetosputtering from a ZnO target with a small TM plate attached.

X-ray fluorescence analysis performed at the Phase Contrast Imaging (PCI) beamline at Singapore Synchrotron Light Source (SSLS) was employed to determine the stoichiometry of the films. The TM composition x in $Zn_{1-x}TM_xO$ was derived by comparing the areas under the Zn K_α and TM K_α peaks and those of a calibrated sample of known concentration. The alloy fraction x of $Zn_{1-x}Co_xO$ was determined to be 1.5%, 2.1%, 2.3%, 3.9%, 19.1% and 21%. The alloy fraction x of $Zn_{1-x}Cu_xO$ was determined to be 1.3%, 1.4%, 2.4%, 5.8%, 18.8% and 24.6%. The alloy fraction x of $Zn_{1-x}Ti_xO$ was determined to be 0.4%, 0.6%, 2.8% and 6.7%. The alloy fraction x of $Zn_{1-x}Mn_xO$ was determined to be 0.1%, 2.2% and 3.7%.

Scanning electron microscopy (SEM) images showed the polycrystalline nature of the film surfaces. The Co, Cu and Ti-doped ZnO films have relatively small and slightly elongated spherical grain structure. The Mn-doped ZnO films, on the other hand, have a mixture of small, spherical and blade-like grain structures. The images at high magnification also display ring hexagonal structures of the ZnO compound.

X-ray diffraction (XRD) studies using Cu K α radiation indicated the polycrystalline nature of the films. All TM-doped ZnO films deposited on glass slides exhibit ZnO (002) peak. The dominant ZnO (002) peak indicates that these films have a strongly c-axis orientated wurtzite structure. Thus, ZnO films grown on glass slides might have slightly different crystal phases as compared to those grown on Si (100) substrates.

All TM (Co, Cu, Ti and Mn)-doped ZnO films deposited on Si (100) exhibit structural anisotropic behavior. No particular trend is observed for the films grown under the same gas ambient for all TM-doped samples.

ZnO (002) and ZnO (201) peaks are observed in all the XRD spectra of the undoped ZnO and Co, Ti and Mn-doped ZnO films deposited on Si (100) substrates. This indicates non-preferential-orientation wurtzite structures. All the peak positions of ZnO: TM are shifted slightly towards the higher angles as compared to undoped ZnO. The peak shifts suggest a decrease in lattice height c for the all TM-doped ZnO films. The decrease in c is consistent with the substitution of Zn^{2+} ion by the smaller Co^{2+} ion. However, it is not consistent in the cases of Cu, Ti and Mn doping. Hence, ionic radii difference between Zn^{2+} and TM ions cannot fully account for the decrease in lattice parameter c. Other possible reasons might be the strain caused by non-uniform substitution of Cu, Ti and Mn ions into the Zn site, and complex defect formation.

Secondary ion mass spectrometry (SIMS) has shown that out of the three annealed TM (Co, Cu and Mn)-doped ZnO samples, only $Zn_{0.977}Co_{0.023}O$ showed uniform dopant distribution relative to the Zn^{2+} distribution. The as prepared $Zn_{0.986}Cu_{0.014}O$ sample possessed a slightly higher concentration of Cu ions in the bulk of ZnO with respect to the surface whereby after annealing, surface precipitation of Cu or Cu oxides was observed. $Zn_{0.978}Mn_{0.022}O$ film consisted of two-layers, the bottom layer being Mn richer than the top layer. After annealing this sample, the concentration of Mn at shallower depth increased.

X-ray absorption fine structure (XAFS) was measured at room temperature at the X-ray Development and Demonstration (XDD) beamline at SSLS in fluorescence mode. The XAFS spectra were compared to standard samples of oxides and metal foils measured in transmission mode.

XAFS results indicate that the percolation threshold of Co into ZnO cannot exceed 19%. The majority of Co^{2+} ions were incorporated into the substitutional sites of the Zn lattice for low Co doping content and they adopt a tetrahedral coordination. Co_3O_4 clusters are formed when subjected to 800^{o}C calcination and when the ambient in which the films are fabricated consists of 20% oxygen gas. Co metal are the major precipitates when the solubility limit is exceeded.

XAFS results show that the Cu ions in ZnO matrix are unstable against 400°C calcination and tend to precipitate easily as Cu or Cu_2O.

Furthermore, the ZnO lattice is greatly distorted with Cu doping, as distinct from Mn and Co doping in ZnO. The solubility of Cu into ZnO is extremely low (less than 1.3%). The substituted Cu ions at the Zn sites have a valence state of 1+. Cu_2O are the main precipiates when the percolation threshold is exceeded.

XAFS results indicate that the percolation threshold of Ti in ZnO cannot exceed 6.7%. The majority of Ti^{3+} ions have been incorporated into the substitutional sites of the Zn lattice at about and below 2.8% Ti doping content; the results also revealed predominant tetrahedral coordination geometry of Ti atoms in $Zn_{1-x}Ti_xO$. The ZnO lattice is distorted with Ti doping, demonostrated by the fact that Zn-O has a stronger interaction than ZnO. Titanium oxides are formed when the films are fabricated in the ambient containing 20% oxygen, and zinc titanate compounds are generated at approximately 6.7% Ti doping content.

XAFS results confirmed the incoporation of the majority of Mn^{2+} ions at the substitutional sites of the Zn lattice for low Mn doping content and they substitute the Zn ions at tetrahedral sites. There is also an overall expansion of the ZnO lattice as a result of doping larger Mn^{2+} ions. Mn oxides with higher oxidization state are formed when the ambient in which the films are fabricated consists of 20% oxygen gas. When the Mn-doped ZnO sample is annealed at 800°C, Mn_2O_3 clusters and the ZnMnO complex containing Mn^{3+} and Mn^{4+} are generated.

The Fourier transformed spectra of Co, Ti and Mn-doped ZnO normally shows a well-ordered coordination up to the third shell. However, Co dopant in ZnO matrix results in less distortion of the ZnO lattice (in terms of R_{Zn-O}) as compared to Ti, Mn and Cu dopants. The ionic radius matching with the ZnO lattice may be the main factor since this induces less strain energy. The charge transfer from ZnO to TM 3d orbitals also appears to be an important consideration. Such a charge transfer trend observed is compatible with the BMP model. The stable doping for Co but not for Mn, Cu and Ti, is indicative of the importance of ionic radius matching with ZnO matrix, in order to reduce the free energy.

VSM measurements at room temperature revealed that the TM (Co, Cu, Ti and Mn)–doped ZnO films are ferromagnetic. The origins of the FM

of the insulating TM-doped ZnO samples can generally be attributed to 1) the spin-split impurity-band model and/or 2) the intrinsic magnetism that can be explained by the BMP model.

The largest measured moments for TM-doped ZnO without any precipitation are 0.237±0.004 μ_B/Co in $Zn_{0.985}Co_{0.015}O$, 0.090±0.004μ_B/Ti in $Zn_{0.996}Ti_{0.004}O$ and 1.882±0.022μ_B/Mn in $Zn_{0.999}Mn_{0.001}O$.

In all TM–doped ZnO films, M_s(μ_B/TM atom) is generally found to decrease with increasing $\boldsymbol{x}$. This trend can be explained by a few reasons. Firstly, at higher TM concentrations, there is an increasing occurrence of AFM coupling between TM pairs, groups of four and coupled clusters of N TM atoms. Secondly, the rapid drop in M_s on the increment of TM content can be attributed to the enhanced dopant-dopant associations leading to progressive orbital moment quenching. Thirdly, the formation of AFM TM oxide clusters at high TM concentrations might also lead to the fall in M_s(μ_B/TM atom).

In conclusion, TM-doped ZnO DMS films were successfully fabricated on silicon with ferromagnetism at room temperature which hopefully will be useful in fabricating future Si-based spintronics devices. Further examinations of the magnetization properties of the TM-doped ZnO films could be carried out by performing Superconducting Quantum Interfering Devices (SQUID) measurements on the samples at low temperatures.